

Parenchymal border macrophages regulate the flow dynamics of the cerebrospinal fluid



<https://doi.org/10.1038/s41586-022-05397-3>

Received: 18 November 2021

Accepted: 29 September 2022

Published online: 9 November 2022

 Check for updates

Antoine Drieu^{1,2}, Siling Du^{1,2,3,33}, Steffen E. Storck^{1,2,33}, Justin Rustenhoven^{1,2,33}, Zachary Papadopoulos^{1,2,3}, Taitea Dykstra^{1,2}, Fenghe Zhong⁴, Kyungdeok Kim^{1,2}, Susan Blackburn^{1,2}, Tornike Mamuladze^{1,2,3}, Oscar Harari⁵, Celeste M. Karch^{5,6}, Randall J. Bateman⁶, Richard Perrin^{2,6}, Martin Farlow⁷, Jasmeer Chhatwal⁸, Dominantly Inherited Alzheimer Network*, Song Hu⁴, Gwendalyn J. Randolph², Igor Smirnov^{1,2} & Jonathan Kipnis^{1,2,3}

Macrophages are important players in the maintenance of tissue homeostasis¹. Perivascular and leptomeningeal macrophages reside near the central nervous system (CNS) parenchyma², and their role in CNS physiology has not been sufficiently well studied. Given their continuous interaction with the cerebrospinal fluid (CSF) and strategic positioning, we refer to these cells collectively as parenchymal border macrophages (PBMs). Here we demonstrate that PBMs regulate CSF flow dynamics. We identify a subpopulation of PBMs that express high levels of CD163 and LYVE1 (scavenger receptor proteins), closely associated with the brain arterial tree, and show that LYVE1⁺ PBMs regulate arterial motion that drives CSF flow. Pharmacological or genetic depletion of PBMs led to accumulation of extracellular matrix proteins, obstructing CSF access to perivascular spaces and impairing CNS perfusion and clearance. Ageing-associated alterations in PBMs and impairment of CSF dynamics were restored after intracisternal injection of macrophage colony-stimulating factor. Single-nucleus RNA sequencing data obtained from patients with Alzheimer's disease (AD) and from non-AD individuals point to changes in phagocytosis, endocytosis and interferon- γ signalling on PBMs, pathways that are corroborated in a mouse model of AD. Collectively, our results identify PBMs as new cellular regulators of CSF flow dynamics, which could be targeted pharmacologically to alleviate brain clearance deficits associated with ageing and AD.

The meninges, a tripartite membranous covering of the brain parenchyma, are densely populated by immune cells and their derived cytokines can affect mouse behaviour^{3–5}. Cytokines from the periphery and the meninges can be carried along in CSF, which is driven by arterial pulsation and vasomotion to circulate throughout the brain parenchyma^{6–8}. This parenchymal perfusion by CSF not only provides meningeal immune molecules direct access to brain cell signalling but also performs 'lymphatic clearance'⁹ by facilitating, through meningeal lymphatics, the removal and subsequent clearance of brain metabolites^{10,11}. Antigens are transported along the same routes into the dura, where they are sampled by dural antigen-presenting cells and presented to patrolling T cells to ensure immune surveillance of the CNS¹². Some of these brain-derived antigens subsequently also drain into the deep cervical lymph nodes (dCLNs) through meningeal lymphatic vessels¹⁰.

The CNS myeloid niche in the homeostatic brain comprises microglia and leptomeningeal and perivascular macrophages¹³ (we collectively

term these two populations of border macrophages as PBMs). Unlike microglia, which are located within the brain parenchyma, PBMs reside in the leptomeninges and perivascular spaces along the vasculature, and are therefore constantly in direct contact with the CSF^{14–16}. Previous studies have suggested a detrimental role for such macrophages in chronic hypertension¹⁷, AD^{18,19}, stroke and experimental autoimmune encephalomyelitis²⁰. The functions of PBMs in brain homeostasis, however, are still largely unexplored.

Here we show that PBMs regulate CSF flow dynamics, an integral aspect of brain physiology, under homeostatic conditions. We identify arterial-associated PBMs that display a transcriptomic profile of scavenger cells and control extracellular matrix (ECM) remodelling, which affects arterial motion, a driving force of CSF flow dynamics. Depletion of PBMs results in the accumulation of ECM proteins and impairment of brain perfusion by the CSF. We demonstrate that normal ageing is associated with PBM dysfunction. Moreover, treatment of aged mice with macrophage colony-stimulating factor (M-CSF) improves CSF dynamics.

¹Center for Brain Immunology and Glia (BIG), Washington University in St Louis, St Louis, MO, USA. ²Department of Pathology and Immunology, School of Medicine, Washington University in St Louis, St Louis, MO, USA. ³Immunology Graduate Program, School of Medicine, Washington University in St Louis, St Louis, MO, USA. ⁴Department of Biomedical Engineering, Danforth Campus, Washington University in St Louis, St Louis, MO, USA. ⁵Department of Psychiatry, Washington University in St Louis, St Louis, MO, USA. ⁶Department of Neurology, Hope Center for Neurological Disorders, Knight Alzheimer's Disease Research Center, School of Medicine, Washington University in St Louis, St Louis, MO, USA. ⁷Indiana School of Medicine, Indianapolis, IN, USA. ⁸Department of Neurology, Massachusetts General Hospital, Harvard Medical School, Boston, MA, USA. ³³These authors contributed equally: Siling Du, Steffen E. Storck, Justin Rustenhoven. *A list of authors and their affiliations appears at the end of the paper.  e-mail: drieu@wustl.edu; kipnis@wustl.edu

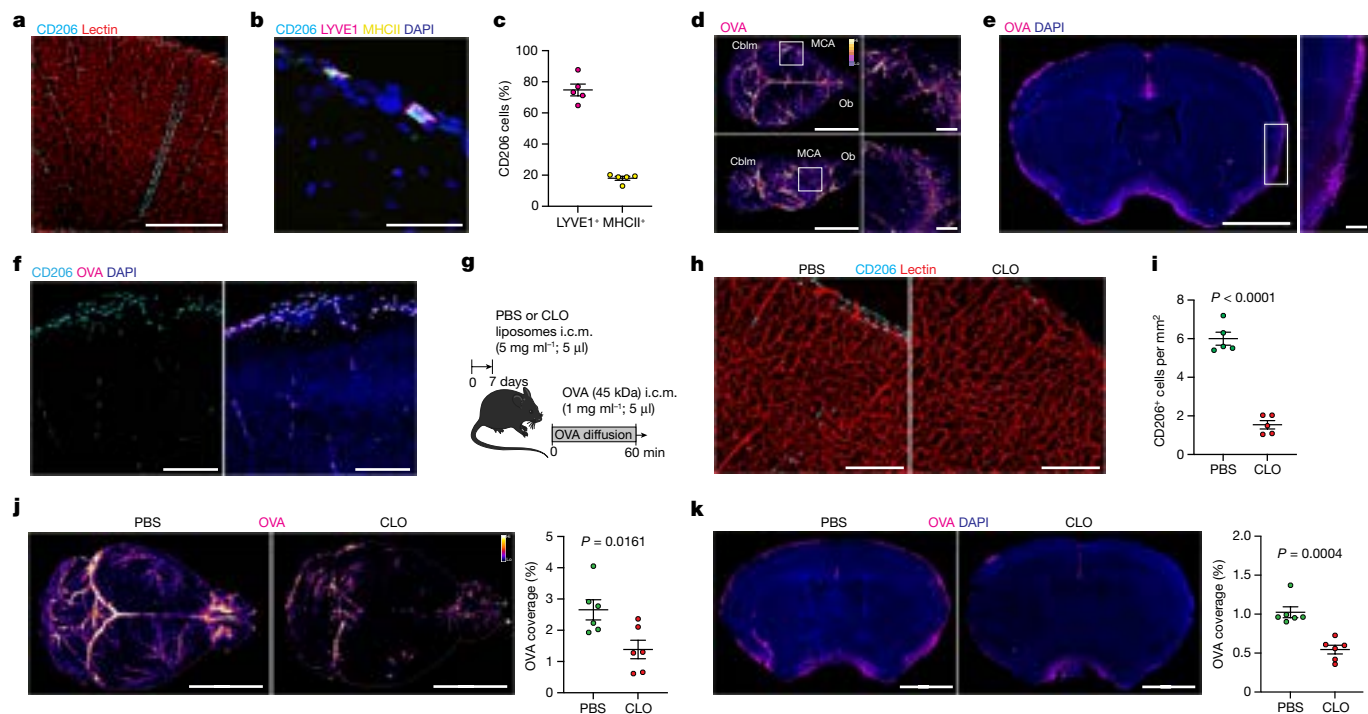


Fig. 1 | PBMs sample CSF and regulate its flow dynamics. **a**, CD206⁺ PBMs are located in close association with blood vessels stained positive by intravenous injection of lectin. **b**, CD206⁺ PBMs can be separated into two major subtypes by their expression of LYVE1 or MHCII co-stained for DAPI. **c**, Quantification of LYVE1⁺ versus MHCII⁺ PBM subtypes (average of both perivascular space and leptomeninges). *n* = 5 mice. **d**, WT mice received an i.c.m. injection of Alexa 647-conjugated OVA. Mice were perfused 1 h after OVA injection. Representative stereomicroscopy images showing whole brain OVA distribution from top (top row) and side (bottom row) views. OVA is mostly distributed around the olfactory bulbs (Ob), MCA and cerebellum (Cblm). **e**, OVA distribution in brain coronal sections (co-stained for DAPI) is largely found in leptomeninges and penetrating blood vessels. At higher magnification, OVA distribution also appears to be cellular (inset). **f**, OVA⁺ cells express the PBM

marker CD206. **g**, Schematic of experiment. One week after PBM depletion using i.c.m.-injected CLO liposomes, mice received an i.c.m. injection of OVA and perfused 1 h later. **h**, Representative images of brain sections showing CD206 and intravenously-injected lectin staining. **i**, Quantification of CD206⁺ cells. *n* = 5 mice per group; two-tailed unpaired Welch's *t*-test. **j**, Representative images showing OVA distribution in whole brains in PBM-depleted and control mice (left) and corresponding quantification (right). **k**, OVA coverage in brain coronal sections (left) and corresponding quantification (right). For **j** and **k**, *n* = 6 mice per group; two-tailed unpaired Welch's *t*-test. All data are presented as the mean ± s.e.m. Scale bars, 50 μm (**b**), 100 μm (**f**), 200 μm (**e**, inset, **h**), 500 μm (**a**), 1 mm (**d**, inset), 2 mm (**e**, **k**) or 5 mm (**d**, **j**). The illustration of the mouse in **g** is from Servier Medical Art, CC BY 3.0.

PBMs sample CSF and regulate its flow

PBMs are found in leptomeningeal and perivascular spaces in the brain, at the vicinity of larger blood vessels, and can be distinguished from microglia by their location and expression of the mannose receptor CD206 (ref. 16) (Fig. 1a, Extended Data Fig. 1a–c and Supplementary Video 1). We were able to distinguish two subtypes of PBMs on the basis of their expression of either LYVE1 or major histocompatibility complex II (MHCII) (Fig. 1b,c). Using flow cytometry, PBMs were distinguished using MHCII and CD38 as a substitute to LYVE1, as previously described²¹ (Extended Data Fig. 1d).

Perivascular spaces are filled with CSF and constitute an interface between blood and the CNS parenchyma²². CSF flows along the perivascular space, can cross astrocytic endfeet and flow into the brain (a process termed glymphatic)^{9,23}. We studied CSF flow dynamics by injecting fluorescent tracers into the mouse cisterna magna and then assessing tracer diffusion into the brain. Fluorescent ovalbumin (OVA) was delivered through intra-cisterna magna (i.c.m.) injection, and the mice were perfused after 1 h. The entire brain was extracted, fixed and imaged by light sheet microscopy (Extended Data Fig. 1e and Supplementary Video 2) or by stereomicroscopy (Fig. 1d and Extended Data Fig. 1f). Using these methods, we observed that OVA was mostly located in the regions of the olfactory bulbs, the cerebellum and the middle cerebral artery (MCA) (Fig. 1d). Although most of the tracer accumulated at the perivascular space, 28.9% of tracer was sampled by cells (Fig. 1d and Extended Data Fig. 1f).

Tracer penetration into the brain parenchyma is reportedly greater for small fluorescent tracers²⁴. However, we found that tracers, independent of their size, accumulated in both perivascular and leptomeningeal spaces in CD206⁺ macrophages (or PBMs; Fig. 1e,f and Extended Data Fig. 1g). We also observed tracer uptake by PBMs when tracers were infused into the striatum (Extended Data Fig. 1h), which suggested that PBMs sample CSF content on its way into and out of the brain. Indeed, we observed double-positive PBMs 2 h after the tracers were co-injected into both the striatum and CSF, although CSF influx was reduced owing to concomitant intra-striatal injection, as previously described²³ (Extended Data Fig. 1i).

Given the close association of PBMs with CSF, we hypothesized that CSF flow dynamics may be partially controlled by PBMs. To test this hypothesis, liposomes containing clodronate (CLO) were administered through i.c.m. injections to deplete PBMs (about 75% depletion was achieved when brain tissue was examined 1 week later; Fig. 1g–i). We confirmed that both the number and the morphology of microglial cells were not affected by i.c.m. CLO liposome administration (Extended Data Fig. 2a). Immunohistochemistry (IHC) and single-cell RNA-sequencing (scRNA-seq) analyses also demonstrated that PBMs are the major population of brain border-associated cells that phagocytosed i.c.m.-injected DiI-labelled liposomes. By contrast, microglia and other stromal cells did not sample the tracer (Extended Data Fig. 2b–e) and hence could not be directly affected by the liposomes. Notably, we observed two major PBM subtypes on the basis of their gene expression

of *Lyve1* and *MHCII*, as well as by staining and flow cytometry (Extended Data Fig. 2f–i). Specifically, CD206⁺LYVE1⁺MHCII^{lo/neg} PBMs were highly phagocytic and endocytic cells, expressing high levels of scavenger receptors such as *Cd163*, *Mrc1*, *Lyve1*, *Msr1* and *Siglec1*. Notably, these cells also upregulated genes involved in the interferon- γ (IFN γ) pathway such as *Irf8*, *Ifitm2* and *Ifitm6* (Extended Data Fig. 2h,i). Gene ontology pathway analyses highlighted important roles of LYVE1⁺ PBMs in metabolic processes and chemotaxis (Extended Data Fig. 2i). Conversely, CD206⁺LYVE1⁺MHCII⁺ PBMs upregulated pathways that are involved in immune response, response to viruses, cytokine production, cell–cell adhesion and antigen presentation (Extended Data Fig. 2h,i). These results indicated that the two PBM subtypes have different functions.

To assess the role of PBMs in CSF dynamics, fluorescent OVA was given through i.c.m. injection 1 week after PBM depletion. After allowing the tracer to diffuse freely for 1 h, mice were perfused and the whole brain was extracted, fixed and imaged by stereomicroscopy (Fig. 1j). In PBM-depleted mice, the OVA coverage was significantly reduced (Fig. 1j). Brains were then sectioned to evaluate OVA coverage in coronal sections, a method commonly used to evaluate CSF influx^{9,25} (Fig. 1k). OVA coverage of brain slices was also significantly reduced in PBM-depleted mice (Fig. 1k). Three days after CLO treatment, CSF flow was impaired to a lesser extent than 1 week after, which correlates with a lower level of (nevertheless, significant) PBM depletion at this time point (Extended Data Fig. 2j–m).

Our group recently showed that CSF flow is impaired after dural lymphatic ablation²⁵. After 3 days of CLO treatment, the number of CD206⁺ dural macrophages located at the vicinity of the superior sagittal sinus was reduced (Extended Data Fig. 2n–o). Conversely, there was no effect of CLO treatment after 1 week on either dural lymphatic vessels or dural CD206⁺ macrophages, which indicates that the observed impairment of CSF flow in this study cannot be attributed to dural lymphatic ablation (Extended Data Fig. 2p–s). There was also no effect of CLO treatment on choroid plexus CD206⁺ macrophages (Extended Data Fig. 2t). However, a population of IBA1⁺ cells were absent in dCLNs after CLO treatment (Extended Data Fig. 2u), which are presumably sinus subcapsular macrophages that were depleted once CLO liposomes drained to dCLNs.

We repeated the CSF flow experiment using 4 kDa dextran conjugated with fluorescein isothiocyanate (FITC–dextran) or 3 kDa Texas Red, which are more diffusive owing to their small molecular weight. Similar to OVA, the influx of small tracers was impaired after PBM depletion (Extended Data Fig. 3a,b). Furthermore, we observed significant accumulation of tracers (both OVA and FITC–dextran) in the brain parenchyma 1 h after intra-striatal injection in PBM-depleted mice. This result suggests that both influx and efflux of CSF are impaired after PBM depletion (Extended Data Fig. 3c,d) or that CSF influx and efflux are interdependent, as previously described (for example, intra-striatal injection impairs influx of CSF tracers²³). To assess whether the impairment in CSF flow dynamics affects CSF protein content itself, we performed a proteomics analysis of CSF sampled from PBM-depleted mice and control mice (Extended Data Fig. 3e). Accumulation of synapse-related proteins in PBM-depleted mice, such as NRXN1, PTPRS, NRCAM and CDH2, was observed (Extended Data Fig. 3f–h). Moreover, there was accumulation of clusterin (CLU), apolipoprotein E (APOE) and amyloid precursor protein (APP), proteins that have been associated with AD, in the CSF of PBM-depleted mice (Extended Data Fig. 3i–k).

Next we used magnetic resonance imaging (MRI) to better evaluate the dynamics of CSF flow in vivo^{26,27} (Fig. 2a). Diffusion of the contrast agent (Dotarem; 0.754 kDa) over time was reduced in PBM-depleted compared with control-treated mice (Fig. 2b,c and Supplementary Videos 3 and 4), without any notable effect of PBM depletion on ventricular size (Extended Data Fig. 3l–n). Intracranial pressure was also increased 1 week after PBM depletion, which normalized 3 weeks after depletion (Extended Data Fig. 3o), probably due to cells starting to repopulate the niche^{17,28}. MRI analyses also revealed a reduction of tracer diffusion at the vicinity of the MCA (Extended Data Fig. 3p–r). IHC

analyses showed that OVA coverage of dCLNs was reduced after PBM depletion (Extended Data Fig. 3s–v). However, there was no difference in OVA drainage to dCLNs, as assessed by in vivo imaging (Extended Data Fig. 3w–y). This is probably because of the rapid efflux of OVA from the dCLNs in PBM-depleted mice, as evidenced from live imaging of drainage (Extended Data Fig. 3y,z). This in turn is probably as a result of sinus subcapsular macrophage depletion by drained CLO liposomes (Extended Data Fig. 2u).

To better understand how PBM depletion affects CSF flow dynamics, we developed a new in vivo approach that enabled us to monitor fluorescent tracer movement over time. CSF tracers rapidly diffuse at the proximal part of the MCA perivascular space^{6,27}. In addition, given the observed reduced tracer coverage around the MCA by MRI (Extended Data Fig. 3p–r), we decided to visualize fluorescent macromolecule movement through the intact lateral parietal bone after retraction of the right temporalis muscle (Fig. 2d,e). Immediately after i.c.m. injection of fluorescent OVA, mice were turned onto their side for in vivo stereomicroscopy imaging of the proximal part of the MCA through the intact skull (Fig. 2d and Extended Data Fig. 4a–c). Using this method, we observed in vivo that OVA rapidly localized at the MCA perivascular space (Extended Data Fig. 4d) and was sampled by perivascular cells (Extended Data Fig. 4e). We validated this method by exposing mice to different anaesthetics that either enhance (ketamine and xylazine (KX) cocktail) or inhibit (isoflurane) the movement of CSF tracers^{29,30} (Extended Data Fig. 4f–j). Using this approach, we observed that OVA coverage over time was strongly reduced in PBM-depleted mice at the MCA level. This was in accordance with ex vivo results showing that global tracer coverage was reduced (Fig. 2f,g and Supplementary Videos 5 and 6).

Collectively, these data provide evidence that PBMs are strategically located at the interface between blood and the brain parenchyma, they sample CSF and regulate its flow dynamics.

PBMs, extracellular matrix and arterial motion

After PBM depletion, OVA was barely able to reach the perivascular space of penetrating vessels (Extended Data Fig. 4k). This raised questions about the morphology of the perivascular space after PBM depletion. Aquaporin-4 (AQP4), a water channel present in the astrocytic endfeet that form the glia limitans (that is, the outer layer of the perivascular space), has been proposed as a mediator of CSF influx²³. Using IHC, we were unable to detect any effect of PBM depletion on AQP4 coverage or AQP4 polarization (Extended Data Fig. 4l–n). By measuring the diameter of the perivascular space using the vascular marker CD31 in combination with AQP4 (Extended Data Fig. 4o), the space between the two markers (arguably representing the perivascular space) was substantially smaller in PBM-depleted mice than in control mice (Extended Data Fig. 4o–q). Using i.c.m.-injected fluorescent microbeads⁶, we were able to assess perivascular space in vivo (Extended Data Fig. 4r–t). However, this method did not allow assessment of the perivascular space in PBM-depleted mice because few beads could be detected (Extended Data Fig. 4s,t). To circumvent in vivo imaging, we perfused the mice with PBS without paraformaldehyde (PFA) to preserve the perivascular space, and bead accumulation was assessed at the vicinity of the MCA⁶ (Extended Data Fig. 4u,v). First, we compared perivascular space measurements in PBS-treated mice using both methods. A slight decrease in ex vivo compared to in vivo measurements was observed (Extended Data Fig. 4u–w). Using this method, the bead coverage was strongly reduced in PBM-depleted mice (Extended Data Fig. 4x). Although the perivascular space and MCA diameter did not change (Extended Data Fig. 4y), the space filled by the beads was reduced in PBM-depleted mice (Extended Data Fig. 4z).

The changes in CSF flow dynamics were accompanied by mild behavioural alterations (Extended Data Fig. 5). PBM-depleted mice froze more on the first day of the cued-fear conditioning test (Extended

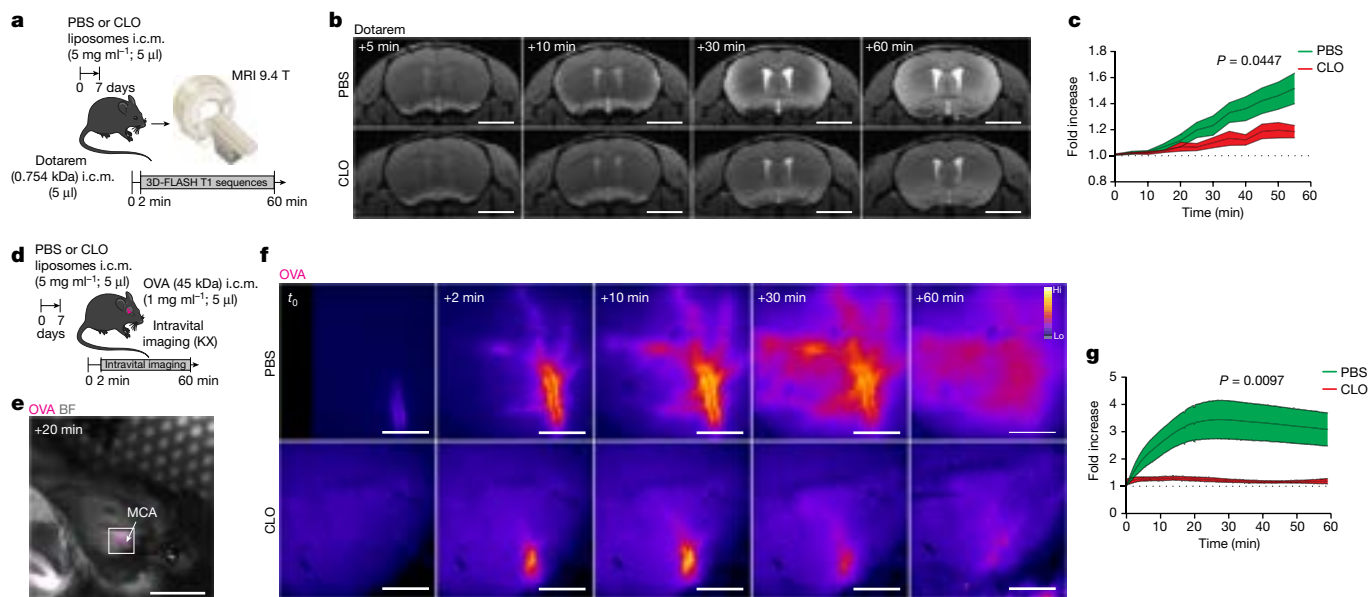


Fig. 2 | In vivo evidence of PBMs regulating CSF flow dynamics. **a**, Schematic of experiment. One week after PBM depletion, mice received an i.c.m. injection of Dotarem and were placed in a prone position into the MRI device for dynamic imaging. **b**, Representative brain coronal images showing Dotarem distribution over 1 h. **c**, Quantification of Dotarem signal fold-increase over time. $n = 5$ mice (treated with PBS) or 7 mice (treated with CLO). **d**, Schematic of experiment. One week after injection with CLO-containing or PBS-containing liposomes, the right temporal bone was exposed and mice received an i.c.m. injection of OVA. Mice were immediately imaged on their side by

stereomicroscopy. **e**, Representative in vivo OVA imaging at low magnification 20 min after i.c.m. injection. BF, brightfield. **f**, Representative images showing OVA distribution over 1 h at the proximal part of the MCA. **g**, Quantification of OVA signal fold-increase over time. $n = 6$ mice per group. All data are presented as the mean \pm s.e.m. P values calculated using repeated measures two-way analysis of variance (ANOVA) with Geisser–Greenhouse correction (**c,g**). Scale bars, 1 mm (**f**), 3 mm (**b**) or 5 mm (**e**). The illustrations of mice (**a,d**) and the MRI scanner (**a**) are from Servier Medical Art, CC BY 3.0.

Data Fig. 5a). However, PBM-depleted mice did not show any deficits in the following parameters: anxiety (assessed using the elevated plus maze test; Extended Data Fig. 5b); general motor activity (assessed using the open-field test; Extended Data Fig. 5c); response to stress (assessed using the forced-swim test; Extended Data Fig. 5d); or social recognition (assessed using the three-chamber test; Extended Data Fig. 5e). We also measured vital signs such as respiratory rate, heart rate and arterial pulsations and diameter, and did not find any difference between groups (Extended Data Fig. 5f).

To understand whether stromal cells (that is, endothelial cells and mural cells such as pericytes, vascular smooth muscle cells (VSMCs) and fibroblasts) are affected by PBM depletion, we sorted CD45⁺CD13⁺CD31⁻ (mural) cells and CD45⁺CD13⁻CD31⁺ (endothelial) cells and performed scRNA-seq 1 week after PBM depletion (Extended Data Fig. 6a). Fibroblasts (and pericytes, to a lesser extent) were the main producers of ECM, and ECM-related genes (*Lgals3*, *Col1a2*, *Tgfb2*, *Lum*, *Col11a1* and *Col8a2*) were upregulated in PBM-depleted mice (Extended Data Fig. 6b). We also observed transcriptional changes in pericytes, mainly related to angiogenesis and DNA methylation (Extended Data Fig. 6c), as well as in capillaries (Extended Data Fig. 6d). However, there were no differences in terms of mural cell (Extended Data Fig. 6e), endothelial cell (Extended Data Fig. 6f) or VSMC coverage (Extended Data Fig. 6g).

Macrophages have been proposed to regulate ECM degradation in other organs through the production of matrix metalloproteinases (MMPs) such as MMP2 and MMP9, which degrade the ECM secreted by other cell types such as fibroblasts and VSMCs²⁶. We proposed that PBM depletion could lead to changes in MMP activity, which in turn results in ECM accumulation that might interfere with CSF flow dynamics. Collagen type IV and laminin, both ECM proteins that are highly expressed in the brain, were accumulated around CD31⁺ vessels in PBM-depleted mice compared with vehicle-treated controls (Fig. 3a–c and Extended Data Fig. 6h–l). When analysed separately, we also observed an accumulation of ECM proteins at the vicinity of large

surface and penetrating blood vessels stained positive for α -smooth muscle actin (α SMA⁺) (Extended Data Fig. 6m,n). Furthermore, fluorescence spectrometry showed that MMP activity in the soluble brain fraction of PBM-depleted mice was significantly reduced (Fig. 3d,e). These results indicated that the functional perivascular space is regulated by PBMs through ECM remodelling.

Arterial pulsation^{6,7} and vasomotion⁸ are major drivers of CSF flow dynamics. It has been proposed that ECM deposition at the aorta level might affect its stiffness³¹. To test whether arterial motion might also be affected by PBM depletion, we created a small cranial window to observe vessel reactivity in vivo by photoacoustic microscopy (Fig. 3f). Head-restrained awake mice were placed on a moving platform and were able to move freely during image acquisition. At 1 min after the start of the imaging session, mice received 10% carbon dioxide (CO₂) in medical air through a nose cone to induce vessel dilation. Using this approach, we were able to record vessel diameter before and during the CO₂ challenge (Fig. 3f). Vasodilatory responses of arteries in PBM-depleted mice were impaired compared with control mice (Fig. 3g,h and Supplementary Videos 7 and 8). To confirm these findings, we assessed neurovascular coupling by recording vascular dilation through a thinned-skull cranial window at the barrel cortex level during contralateral stimulation of mouse whiskers³² (Fig. 3i). Vessel dilation after whisker stimulation was impaired in PBM-depleted mice compared with control counterparts (Fig. 3j and Supplementary Videos 9 and 10). Systemic application of dobutamine, a β_1 -adrenergic agonist previously shown to enhance arterial pulsations⁷, rescued the impaired CSF dynamics in PBM-depleted mice, as determined by i.c.m. injection of OVA and assessment of its distribution through the perivascular spaces and its influx into the parenchyma (Extended Data Fig. 6o–q).

To better understand the biology of PBMs, we performed scRNA-seq from mouse brain samples (Fig. 3k,i and Extended Data Fig. 7a). From the 14 different cell types obtained on the basis of their gene signatures, we isolated PBMs (based on their expression of canonical markers,

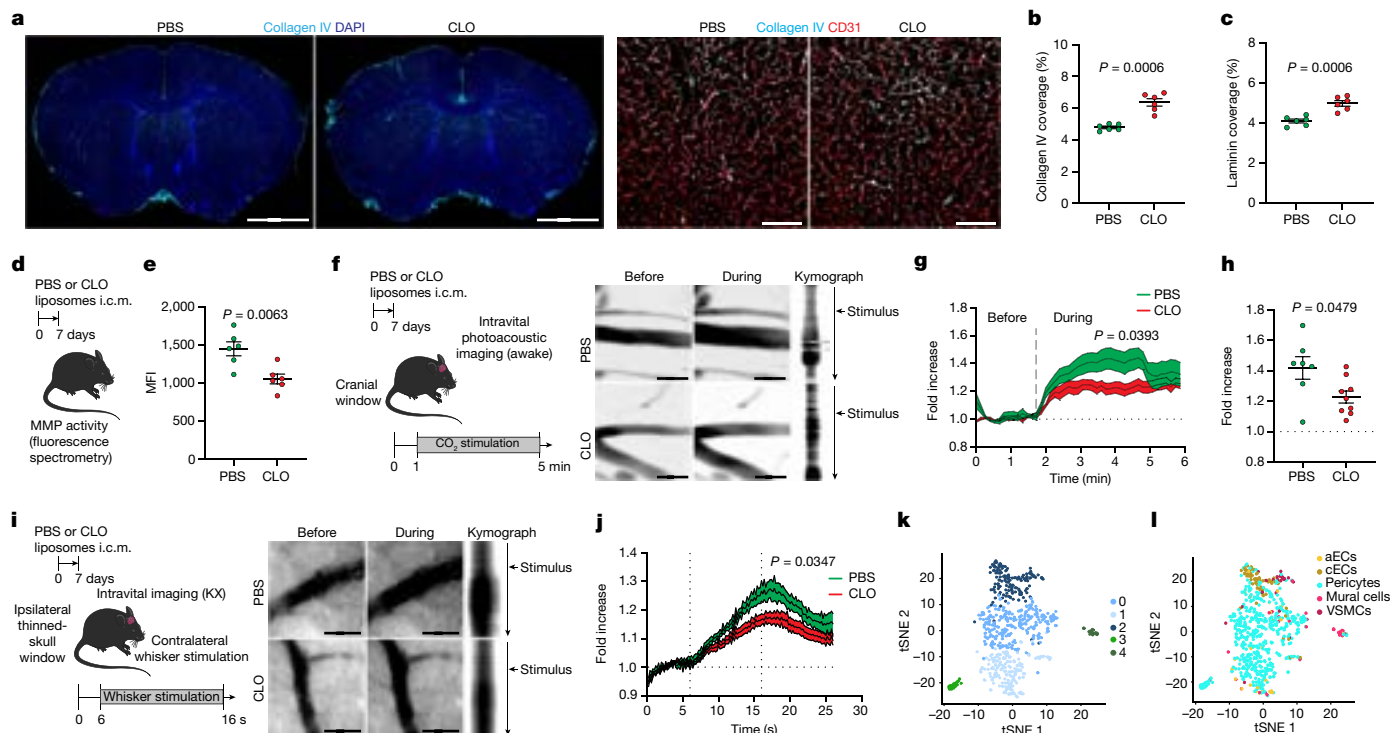


Fig. 3 | PBMs regulate CSF flow dynamics through ECM remodelling and arterial motion. **a**, Left, representative images of brain coronal sections showing collagen IV and DAPI staining. Right, high-magnification images showing collagen IV association with CD31⁺ blood vessels. **b**, Quantification of collagen IV coverage. **c**, Quantification of laminin coverage. For **b** and **c**, $n = 6$ mice per group. **d**, Schematic of experiment. One week after CLO or PBS treatment, brains were extracted and incubated with MMP substrate. **e**, Quantification of MMP activity. $n = 6$ mice per group. MFI, mean fluorescence intensity. **f**, Left, schematic of experiment. One week after CLO or PBS treatment, mice were imaged using photoacoustic microscopy. Right, representative images showing vessels before (left) and during (middle) 10% CO₂ challenge and corresponding kymographs (right). **g**, Quantification of vessel diameter fold-increase over time. $n = 7$ mice (treated with PBS) or 9 mice (treated with CLO). **h**, Quantification of arterial vessel diameter fold-increase during CO₂ challenge. $n = 7$ mice (treated with PBS) or 9 mice (treated with CLO). **i**, Left, schematic of experiment. One week after CLO or PBS liposome injection, mice were imaged by stereomicroscopy. Right, representative images showing vessels before (left) and during (middle) whisker stimulation and corresponding kymographs (right). **j**, Quantification of vessel diameter fold-increase over time. $n = 6$ mice (treated with PBS) or 8 mice (treated with CLO). **k**, Re-clustering of PBM scRNA-seq data revealed five PBM clusters. tSNE, t-distributed stochastic neighbour embedding. **l**, The RNA Magnet algorithm determined that PBM cluster 2 interacts preferentially with VSMCs and capillary endothelial cells (cECs), whereas PBM clusters 0 and 1 preferentially interact with pericytes. aECs, arterial endothelial cells. All data are presented as the mean \pm s.e.m. P values calculated using two-tailed unpaired Welch's t -test (**c**, **e**, **h**) or repeated measures two-way ANOVA with Geisser–Greenhouse correction (**g**, **j**). Scale bars, 30 μ m (**f**, **i**), 200 μ m (**a**, right) or 2 mm (**a**, left). The illustrations of mice in **d**, **f** and **i** are from Servier Medical Art, CC BY 3.0.

including *Mrc1* and *Ms4a7*) and obtained 5 PBM clusters (Fig. 3k). To delineate crosstalk between PBMs and other cell types, we used the RNA Magnet algorithm, which predicts paired physical and signalling interactions between cell types³³. Notably, we found that cluster 2, which exhibited high expression of scavenger markers such as *Lyve1* and *Cd163*, interacted specifically with VSMCs, which are located at the arterial level (Fig. 3l). Spatial proximity between PBMs and VSMCs was confirmed by electron microscopy, which indicated that these two cell types may interact, although they are separated by the basal lamina (Extended Data Fig. 7b). These results confirmed recent findings that described important interactions between VSMCs and perivascular macrophages to allow their migration at the perivascular space². Looking at differentially expressed genes between PBM clusters, cluster 2 was identified as potential professional scavenger cells (*Cd163*, *Cd38*, *Lyve1*, *Msr1* and *Cd36*) when compared to the other clusters, which expressed genes related to antigen presentation (*H2-Ab1*, *Cd74*, *Cd83*, *Cd14* and *Nlrp3*) (Extended Data Fig. 7c–e). Immunostaining confirmed that LYVE1⁺ PBMs were highly concentrated at the vicinity of α SMA⁺ brain arteries and arterioles, whereas MHCII⁺ PBMs were mostly localized to α SMA⁻ brain blood vessels (Extended Data Fig. 7f,g). We then took advantage of LYVE1 expression by PBMs to genetically target these cells using *Lyve1*^{Cre::Csf1r}^{fl/fl} mice³⁴ (Cre⁺; Extended Data Fig. 7h). Mice at 3 months of age showed about 50% depletion of PBMs compared

with their littermate controls not expressing Cre (Cre⁻; Extended Data Fig. 7i). We confirmed by flow cytometry that CD38⁺ PBMs were depleted by this genetic ablation, without affecting microglial cells or MHCII⁺ PBMs (Extended Data Fig. 7j–n). In support of the results from pharmacological ablation experiments, genetic ablation of LYVE1⁺ PBMs also affected ECM protein levels (Extended Data Fig. 7o,p) and CSF influx (Extended Data Fig. 7q–v). However, there were no changes in vessel coverage, MMP activity or intracranial pressure (Extended Data Fig. 7w–y), and CSF flow impairment was more subtle in these mice (Extended Data Fig. 7q–v). The differences may be because these mice have reduced PBM depletion compared with mice treated with CLO, or because a lifelong reduction in CSF flow resulted in adaptation or emergence of alternative pathways to regulate intracranial pressure. In summary, these observations suggest that PBMs regulate CSF dynamics along the perivascular space and its efflux and influx of the brain parenchyma. The mechanism underlying PBM regulation of CSF dynamics is based on their ability to regulate ECM remodelling, which in turn affects arterial stiffness.

PBMs in ageing and AD

CSF flow is impaired in old mice, and this impairment could be ameliorated in part through enhancement of meningeal lymphatic vessels²⁵.

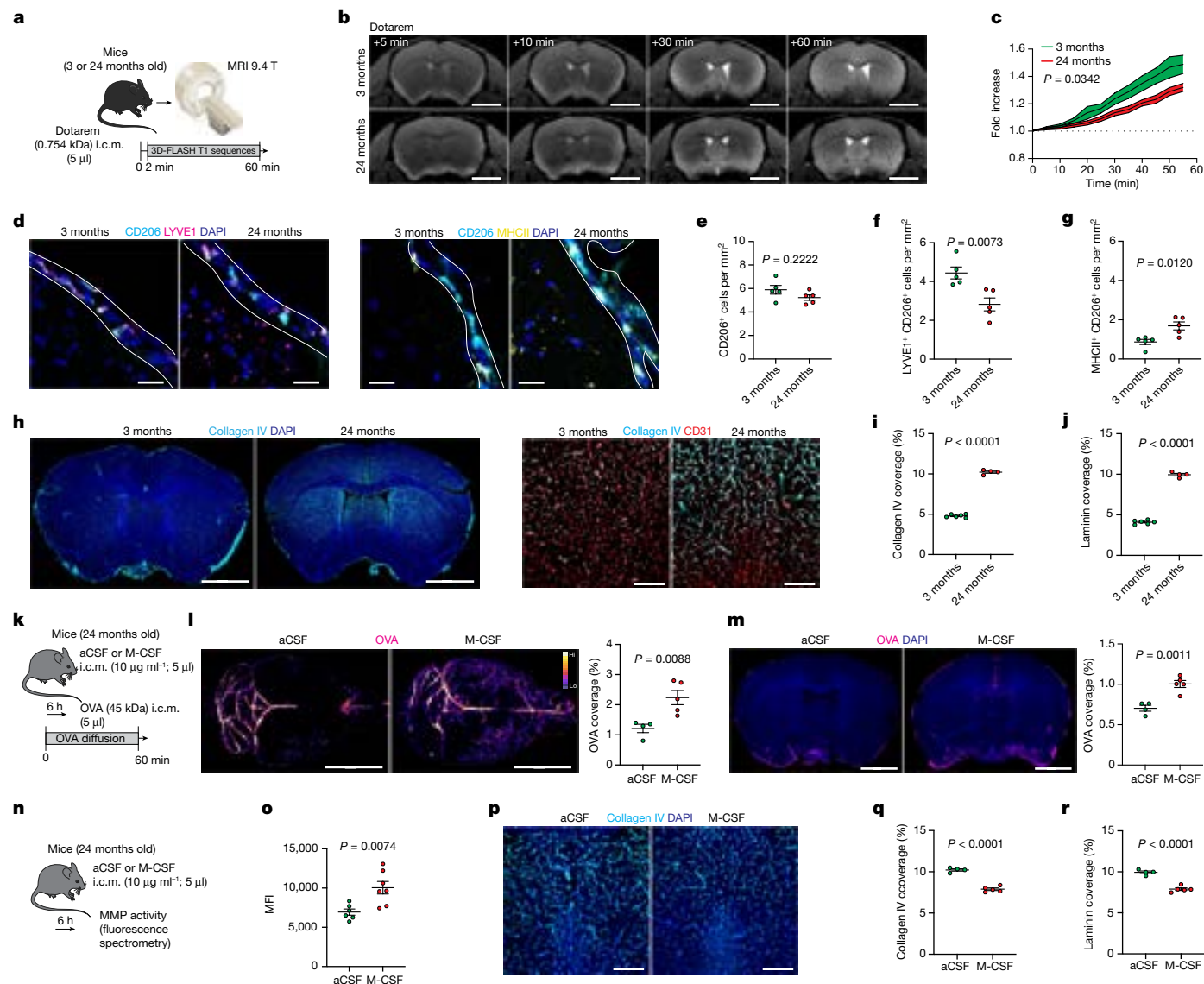


Fig. 4 | PBMs in aged mice. **a**, Schematic of experiment. Young (3 months old) and aged (24 months old) mice received Dotarem through i.c.m. injection and were placed into the MRI device. **b**, Representative images showing Dotarem distribution over 1 h. **c**, Quantification of Dotarem signal fold-increase over time, $n = 5$ mice (3 months old) or 6 mice (24 months old). **d**, Representative images showing CD206, LYVE1, MHCII and DAPI staining. **e**, Quantification of CD206⁺ PBMs. **f**, Quantification of LYVE1⁺ CD206⁺ PBMs. **g**, Quantification of MHCII⁺ CD206⁺ PBMs. For **e–g**, $n = 5$ mice per group. **h**, Left, representative images brain coronal sections showing collagen IV and DAPI staining. Right, high-magnification images showing collagen IV association with CD31⁺ blood vessels. **i**, Quantification of collagen IV coverage. **j**, Quantification of laminin coverage. For **i** and **j**, $n = 6$ mice (3 months old) or 4 mice (24 months old). **k**, Schematic of experiment. Six hours after i.c.m. injection of M-CSF or aCSF, mice received i.c.m. injection of OVA and perfused 1 h later. **l, m**, Representative

images (left) and quantification (right) of OVA distribution in whole brains (**l**) and in brain coronal sections (**m**). $n = 4$ mice (treated with aCSF) or 5 mice (treated with M-CSF). **n**, Schematic of experiment. Six hours after M-CSF treatment, brains were extracted and incubated with MMP substrate. **o**, Quantification of MMP activity. $n = 6$ mice (treated with aCSF) or 7 mice (treated with M-CSF). **p**, High-magnification brain coronal sections images showing collagen IV and DAPI staining. **q**, Quantification of collagen IV coverage. **r**, Quantification of laminin coverage. For **q** and **r**, $n = 4$ mice (treated with aCSF) or 5 mice (treated with M-CSF). All data are presented as the mean \pm s.e.m. P values calculated using two-tailed unpaired Welch's t -test (**e–g, i, j, l, m, o, q, r**) or repeated measures two-way ANOVA with Geisser–Greenhouse correction (**c**). Scale bars, 20 μ m (**d**), 200 μ m (**h**, right; **p**), 2 mm (**h**, left; **l**), 3 mm (**b**). The illustrations of mice (**a, k, n**) and the MRI scanner (**a**) are from Servier Medical Art, CC BY 3.0.

We proposed that PBMs participate in the age-related deterioration of CSF dynamics. MRI analyses demonstrated that CSF flow is globally impaired in old mice. Fluorescent tracers also confirmed impairment at the MCA level, and different molecular weight fluorescent tracers confirmed impairment in brain coronal sections (Fig. 4a–c and Extended Data Fig. 8a–f). Comparison of the PBMs in young adult (3-month-old) and old (24-month-old) mice showed no difference in overall CD206⁺ cell numbers, but aged mice exhibited a significant reduction in LYVE1⁺ cells and an increase in MHCII⁺ cells, which is in agreement with previous reports²¹ (Fig. 4d–g and Extended Data Fig. 8g–k). CD38⁺ PBMs in young

mice were the major cell type that phagocytosed i.c.m. injected pHrodo particles (Extended Data Fig. 8l–o). The change in PBM phenotype observed in aged mice appeared to be associated with impaired pHrodo particle phagocytosis (Extended Data Fig. 8p–r), reduced functional perivascular space filled by the beads (Extended Data Fig. 8s–y) and accumulation of ECM proteins (Fig. 4h–j and Extended Data Fig. 8z).

M-CSF has been previously shown to improve pathophysiology of AD, presumably through the enhancement of amyloid- β (A β) phagocytosis by blood-derived monocytes³⁵. We proposed that such acute activation of PBMs in old mice might enhance their ECM degradation

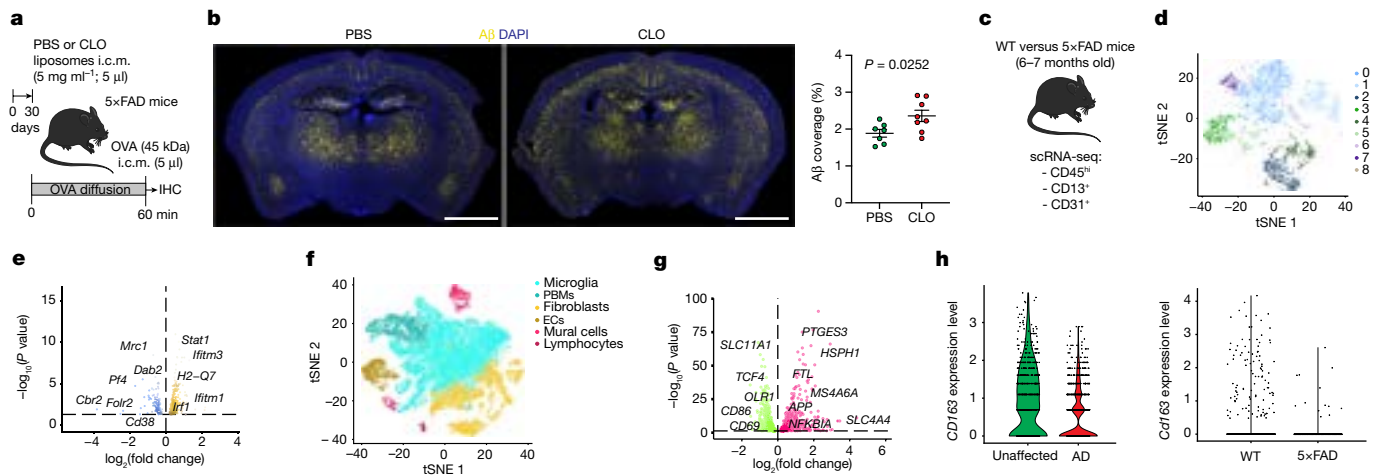


Fig. 5 | PBMs in human AD and a 5×FAD mouse model of amyloidosis.

a, Schematic of experiment. 5×FAD mice received an i.c.m. injection of PBS or CLO liposomes. One month later, mice received an i.c.m. injection of OVA and brains were collected 1 h later. **b**, Representative brain coronal section images showing A β plaque load (left) and corresponding quantification (right). Scale bar, 2 mm. $n = 7$ mice (treated with PBS) or 8 mice (treated with CLO); two-tailed unpaired Welch's t -test. **c**, Schematic of experiment. scRNA-seq of the brain cortex from 6–7-month-old 5×FAD mice and their WT littermates. $n = 8$ mice per group. **d**, Macrophage populations were isolated from the 5×FAD mice and subjected to scRNA-seq. Nine clusters were identified. **e**, Volcano plot corresponding to downregulated and upregulated genes in PBMs comparing 5×FAD mice and their WT littermates. F -test with adjusted degrees of freedom

capacity and improve CSF dynamics. Using scRNA-seq, we confirmed that brain cells expressing *Csf1r* were mainly PBMs, microglial cells and monocytes, although *Csf1* was mostly expressed by microglial and mural cells (Extended Data Fig. 9a). A single i.c.m. injection of M-CSF (or artificial CSF (aCSF) as a control) was performed in old mice, and CSF dynamics was evaluated after i.c.m. injection of OVA tracer 6 h after M-CSF treatment (Fig. 4k). At 1 h after OVA injection, brains were collected and analysed by stereomicroscopy. OVA distribution at the MCA level in M-CSF-treated old mice was significantly enhanced compared with control old mice (Fig. 4l). The same phenotypes were also found in brain coronal sections (Fig. 4m). Notably, acute M-CSF treatment in aged mice significantly increased MMP activity (Fig. 4n,o) and decreased ECM protein deposition (Fig. 4p–r and Extended Data Fig. 9b, c). However, subacute M-CSF treatment (24 h) in aged mice was ineffective at enhancing CSF flow, although MMP activity was still significantly increased, but to a lesser extent than at 6 h. These results indicate that M-CSF treatment acutely drives MMP activity, which results in a short-term improvement in CSF flow (Extended Data Fig. 9d–g).

Our scRNA-seq results revealed that VSMC-associated PBMs can be differentiated from other PBMs by their expression of scavenger receptors (Extended Data Fig. 7c–e). Pathway analysis confirmed that cluster 2 showed upregulated genes characteristic of receptor-mediated endocytosis and phagocytosis (Extended Data Fig. 7e). This analysis also showed that cluster 2 was linked to a cellular response to A β . Furthermore, it has been shown that depletion of perivascular macrophages worsens outcome in a mouse model of cerebral amyloid angiopathy (CAA)³⁶, which suggests that PBMs are processing brain-derived A β . Finally, our CSF proteomics data indicated that PBM depletion leads to an accumulation of AD-associated risk factors such as CLU, APOE and APP (Extended Data Fig. 3i–k). We therefore proposed that PBMs might be involved in A β clearance. To test this hypothesis, 2-month-old 5×FAD mice (a mouse model of AD) each received a single i.c.m. injection of CLO liposomes or, as a control, PBS liposomes (Fig. 5a). CSF flow was impaired in PBM-depleted 5×FAD mice compared with their 5×FAD control littermates (Extended Data Fig. 10a,b). When their A β

based on weights calculated per gene with a zero-inflation model and Benjamini–Hochberg adjusted P values. **f**, Human single-nucleus RNA-seq from patients with familial AD and from unaffected individuals. Six cell populations were used in this dataset: microglia, fibroblasts, endothelial cells (ECs), mural cells, lymphocytes and PBMs. **g**, Volcano plot corresponding to downregulated and upregulated genes in PBMs comparing patients with familial AD and unaffected individuals. F -test with adjusted degrees of freedom based on weights calculated per gene with a zero-inflation model and Benjamini–Hochberg adjusted P values. **h**, Violin plots corresponding to *CD163* gene expression from both human single-nucleus RNA-seq (left) and mouse scRNA-seq (right). All data are presented as the mean \pm s.e.m. The illustrations of mice in **a** and **c** are from Servier Medical Art, CC BY 3.0.

plaque loads were evaluated 1 month later, PBM-depleted 5×FAD mice exhibited significantly increased plaque load compared with their 5×FAD control littermates (Fig. 5b), specifically in the brain cortex and amygdala (Extended Data Fig. 10c). To better understand the role of PBMs in AD pathophysiology, we performed scRNA-seq on brains from 6–7-month-old 5×FAD and their wild-type (WT) littermates (Fig. 5c and Extended Data Fig. 10d). We reclustered all macrophages and identified PBMs using the gene marker *Mrc1* (Fig. 5d and Extended Data Fig. 10e). We also identified a damage-associated microglia (DAM) cluster specifically in 5×FAD mice, as previously described³⁷ (Extended Data Fig. 10f). PBMs from 5×FAD mice exhibited altered phagocytosis and endocytosis and response to IFN γ pathways (Fig. 5e and Extended Data Fig. 10g). We confirmed using the RNA Magnet algorithm that PBMs interact with mural cells, notably VSMCs and fibroblasts (fibroblast-like cells) (Extended Data Fig. 10h). Of note, a human dataset that we had previously used to assess microglial function in AD³⁸ also contained a small population of PBMs (Fig. 5f). PBM populations from unaffected individuals and from patients with familial AD substantially differed, with 445 upregulated and 249 downregulated genes, respectively (Fig. 5g and Extended Data Fig. 10i). Among the most notably dysregulated gene signatures in human PBMs from patients with familial AD were those involved in phagocytosis and endocytosis (*CD163* expression) and IFN γ signalling (Fig. 5h and Extended Data Fig. 10j), which recapitulated the findings from the AD mouse model. Notably, both the IFN γ receptor genes *Ifngr1* and *Ifngr2* were more highly expressed in brain immune cells (that is, microglia and PBMs) than in stromal cells in our mouse single-cell dataset, which indicated an important interaction between PBMs and IFN γ (Extended Data Fig. 10k). To test the possibility that excess IFN γ in CSF may cause dysfunction in CSF dynamics, we injected (i.c.m.) young adult WT mice with IFN γ . These mice exhibited impaired CSF flow compared with mice injected with PBS (Extended Data Fig. 10l,m).

Collectively, these findings reveal that PBMs are pivotal players in CSF flow dynamics in ageing and in AD (Extended Data Fig. 10n). Therefore, PBMs should be further explored as potential new therapeutic targets

for AD and other age-associated diseases characterized by protein aggregation and CSF dysfunction.

Discussion

The results of this study demonstrated that perivascular and leptomeningeal macrophages express similar markers and are located around the CNS parenchyma, constantly interacting with CSF. Given their location, function and marker expression, we suggest referring to them as a single functional population, namely PBMs.

PBMs are composed of two major subtypes: LYVE1⁺MHCII^{lo/neg} and LYVE1^{lo/neg}MHCII⁺. Although PBMs and microglia are both derived from early erythromyeloid progenitors in the yolk sac³⁹, a recent study suggested that LYVE1⁺ macrophages predominantly originated from embryonic-derived progenitors and are maintained locally in the peritoneal mesothelium³⁴. Our data demonstrated that LYVE1⁺MHCII^{lo/neg} PBMs regulate arterial motion and ECM remodelling (along large vessels and capillaries). Indeed, depletion or dysfunction of PBMs resulted in impaired arterial motion, accumulation of ECM and impairment of CSF flow. Previous studies that used CLO liposomes to deplete perivascular macrophages did not observe major changes in cerebral blood flow^{17,19}. The apparent discrepancy may be a result of the use of cranial windows and dura mater removal used in those studies, which might have masked the effects we observed here with thinned-skull preparations. Spontaneous low-frequency oscillations of arterioles in brain parenchyma have been proposed as the driving force of CSF and interstitial fluid clearance⁸. Notably, this paravascular clearance was impaired in the context of CAA. Moreover, depletion of perivascular macrophages in CAA exacerbates the disease³⁶, and perivascular macrophages can produce excessive reactive oxygen species, which then leads to neurovascular dysfunction in the context of hypertension and AD^{17,19}. Together with our data, it is plausible that PBMs are at the interface between spontaneous arterial oscillations, ECM remodelling, neuronal activity and CSF flow.

Notably, aged mice exhibited an increase in LYVE1^{lo/neg}MHCII⁺ PBMs, increased ECM deposition and impaired CSF dynamics. We showed here that treatment of aged mice with M-CSF increased MMP activity, reduced ECM accumulation and acutely restored impaired CSF flow. PBM depletion also resulted in increased accumulation of parenchymal plaques in the 5×FAD mouse model of amyloidosis. PBMs from patients with familial AD exhibited altered expression profiles compared with individuals without AD, including dysregulated pathways involving phagocytosis and endocytosis and IFN γ signalling on PBMs. Similar pathways were also among the most differentially regulated in PBMs of mice from WT compared with 5×FAD mice. Stimulation of PBMs in vivo in young mice through acute injection of IFN γ resulted in CSF flow impairment. Given the pleiotropic nature of IFN γ , however, its effect on CSF dynamics may not be solely as a result of its signalling on PBMs, although expression of both IFN γ receptors was higher in PBMs than other cell types in the brain. Future studies should analyse in further depth the role of IFN γ in CSF flow dynamics and developing intervention therapies for AD and other age-associated disorders based on IFN γ signalling or alternative modulations of PBMs.

Macrophages have previously been associated with cardiovascular diseases such as chronic hypertension^{17,40} and with neurovascular coupling in both AD and homeostasis⁴¹. Although our appreciation of the part played by tissue-resident macrophages in tissue homeostasis has increased in recent years, the exact functions performed by the PBM population are still largely unknown. In this study, we unravelled an unexpected role for PBMs in CSF flow dynamics and demonstrated their potential therapeutic capacities in ageing and in AD. These findings may lead to the development of new therapeutic approaches for diseases associated with CSF dysfunction and with protein accumulation and aggregation, such as AD, Parkinson's disease, among others.

Online content

Any methods, additional references, Nature Research reporting summaries, source data, extended data, supplementary information, acknowledgements, peer review information; details of author contributions and competing interests; and statements of data and code availability are available at <https://doi.org/10.1038/s41586-022-05397-3>.

- Ginhoux, F. & Williams, M. Tissue-resident macrophage ontogeny and homeostasis. *Immunity* **44**, 439–449 (2016).
- Masuda, T. et al. Specification of CNS macrophage subsets occurs postnatally in defined niches. *Nature* **604**, 740–748 (2022).
- Alves de Lima, K. et al. Meningeal $\gamma\delta$ T cells regulate anxiety-like behavior via IL-17a signaling in neurons. *Nat. Immunol.* **21**, 1421–1429 (2020).
- Filiano, A. J. et al. Unexpected role of interferon- γ in regulating neuronal connectivity and social behaviour. *Nature* **535**, 425–429 (2016).
- Konsman, J. P., Parnet, P. & Dantzer, R. Cytokine-induced sickness behaviour: mechanisms and implications. *Trends Neurosci.* **25**, 154–159 (2002).
- Mestre, H. et al. Flow of cerebrospinal fluid is driven by arterial pulsations and is reduced in hypertension. *Nat. Commun.* **9**, 4878 (2018).
- Iliff, J. J. et al. Cerebral arterial pulsation drives paravascular CSF–interstitial fluid exchange in the murine brain. *J. Neurosci.* **33**, 18190–18199 (2013).
- van Veluw, S. J. et al. Vasomotion as a driving force for paravascular clearance in the awake mouse brain. *Neuron* **105**, 549–561.e5 (2020).
- Iliff, J. J. et al. A paravascular pathway facilitates CSF flow through the brain parenchyma and the clearance of interstitial solutes, including amyloid β . *Sci. Transl. Med.* **4**, 147ra111 (2012).
- Louveau, A. et al. Structural and functional features of central nervous system lymphatic vessels. *Nature* **523**, 337–341 (2015).
- Li, X. et al. Meningeal lymphatic vessels mediate neurotropic viral drainage from the central nervous system. *Nat. Neurosci.* **25**, 577–587 (2022).
- Rustenhoven, J. et al. Functional characterization of the dural sinuses as a neuroimmune interface. *Cell* **184**, 1000–1016.e27 (2021).
- Kierdorf, K., Masuda, T., Jordão, M. J. C. & Prinz, M. Macrophages at CNS interfaces: ontogeny and function in health and disease. *Nat. Rev. Neurosci.* **20**, 547–562 (2019).
- Faraco, G., Park, L., Anrather, J. & Iadecola, C. Brain perivascular macrophages: characterization and functional roles in health and disease. *J. Mol. Med.* **95**, 1143–1152 (2017).
- Van Hove, H. et al. A single-cell atlas of mouse brain macrophages reveals unique transcriptional identities shaped by ontogeny and tissue environment. *Nat. Neurosci.* **22**, 1021–1035 (2019).
- Goldmann, T. et al. Origin, fate and dynamics of macrophages at central nervous system interfaces. *Nat. Immunol.* **17**, 797–805 (2016).
- Faraco, G. et al. Perivascular macrophages mediate the neurovascular and cognitive dysfunction associated with hypertension. *J. Clin. Invest.* **126**, 4674–4689 (2016).
- Thanopoulou, K., Fragkouli, A., Stylianopoulou, F. & Georgopoulos, S. Scavenger receptor class B type I (SR-BI) regulates perivascular macrophages and modifies amyloid pathology in an Alzheimer mouse model. *Proc. Natl Acad. Sci. USA* **107**, 20816–20821 (2010).
- Park, L. et al. Brain perivascular macrophages initiate the neurovascular dysfunction of Alzheimer A β peptides. *Circ. Res.* **121**, 258–269 (2017).
- Jordão, M. J. C. et al. Single-cell profiling identifies myeloid cell subsets with distinct fates during neuroinflammation. *Science* **363**, eaat7554 (2019).
- Mrdjen, D. et al. High-dimensional single-cell mapping of central nervous system immune cells reveals distinct myeloid subsets in health, aging, and disease. *Immunity* **48**, 380–395.e6 (2018).
- Wardlaw, J. M. et al. Perivascular spaces in the brain: anatomy, physiology and pathology. *Nat. Rev. Neurol.* **16**, 137–153 (2020).
- Mestre, H. et al. Aquaporin-4-dependent glymphatic solute transport in the rodent brain. *eLife* **7**, e40070 (2018).
- Yang, L. et al. Evaluating glymphatic pathway function utilizing clinically relevant intrathecal infusion of CSF tracer. *J. Transl. Med.* **11**, 107 (2013).
- Da Mesquita, S. et al. Functional aspects of meningeal lymphatics in ageing and Alzheimer's disease. *Nature* **560**, 185–191 (2018).
- Ahn, J. H. et al. Meningeal lymphatic vessels at the skull base drain cerebrospinal fluid. *Nature* **572**, 62–66 (2019).
- Mestre, H. et al. Cerebrospinal fluid influx drives acute ischemic tissue swelling. *Science* **367**, eaax7171 (2020).
- Polfliet, M. M. et al. A method for the selective depletion of perivascular and meningeal macrophages in the central nervous system. *J. Neuroimmunol.* **116**, 188–195 (2001).
- Hablitz, L. M. et al. Increased glymphatic influx is correlated with high EEG delta power and low heart rate in mice under anesthesia. *Sci. Adv.* **5**, eaav5447 (2019).
- Gakuba, C. et al. General anesthesia inhibits the activity of the 'glymphatic system'. *Theranostics* **8**, 710–722 (2018).
- Lim, H. Y. et al. Hyaluronan receptor LYVE-1-expressing macrophages maintain arterial tone through hyaluronan-mediated regulation of smooth muscle cell collagen. *Immunity* **49**, 326–341.e7 (2018).
- Chow, B. W. et al. Caveolae in CNS arterioles mediate neurovascular coupling. *Nature* **579**, 106–110 (2020).
- Baccin, C. et al. Combined single-cell and spatial transcriptomics reveal the molecular, cellular and spatial bone marrow niche organization. *Nat. Cell Biol.* **22**, 38–48 (2020).
- Zhang, N. et al. LYVE1⁺ macrophages of murine peritoneal mesothelium promote omentum-independent ovarian tumor growth. *J. Exp. Med.* **218**, e20210924 (2021).

35. Boissonneault, V. et al. Powerful beneficial effects of macrophage colony-stimulating factor on β -amyloid deposition and cognitive impairment in Alzheimer's disease. *Brain* **132**, 1078–1092 (2009).
36. Hawkes, C. A. & McLaurin, J. Selective targeting of perivascular macrophages for clearance of β -amyloid in cerebral amyloid angiopathy. *Proc. Natl Acad. Sci. USA* **106**, 1261–1266 (2009).
37. Keren-Shaul, H. et al. A unique microglia type associated with restricting development of Alzheimer's disease. *Cell* **169**, 1276–1290.e17 (2017).
38. Da Mesquita, S. et al. Meningeal lymphatics affect microglia responses and anti-A β immunotherapy. *Nature* **593**, 255–260 (2021).
39. Utz, S. G. et al. Early fate defines microglia and non-parenchymal brain macrophage development. *Cell* **181**, 557–573.e18 (2020).
40. Pires, P. W. et al. Improvement in middle cerebral artery structure and endothelial function in stroke-prone spontaneously hypertensive rats after macrophage depletion. *Microcirculation* **20**, 650–661 (2013).
41. Császár, E. et al. Microglia modulate blood flow, neurovascular coupling, and hypoperfusion via purinergic actions. *J. Exp. Med.* **219**, e20211071 (2022).

Publisher's note Springer Nature remains neutral with regard to jurisdictional claims in published maps and institutional affiliations.

Springer Nature or its licensor (e.g. a society or other partner) holds exclusive rights to this article under a publishing agreement with the author(s) or other rightsholder(s); author self-archiving of the accepted manuscript version of this article is solely governed by the terms of such publishing agreement and applicable law.

© The Author(s), under exclusive licence to Springer Nature Limited 2022

Dominantly Inherited Alzheimer Network

Richard Perrin^{2,6}, Celeste M. Karch^{5,6}, Randall J. Bateman⁶, Jared Brosch⁷, Jill Buck⁷, Marty Farlow⁷, Bernardino Ghetti⁷, Jasmeer Chhatwal⁸, Sarah Adams⁹, Nicolas Barthelemy⁹, Tammie Benzinger⁹, Susan Brandon⁹, Virginia Buckles⁹, Lisa Cash⁹, Charlie Chen⁹, Jasmin Chua⁹, Carlos Cruchaga⁹, Darcy Denner⁹, Aylin Dincer⁹, Tamara Donahue⁹, Anne Fagan⁹, Becca Feldman⁹, Shaney Flores⁹, Erin Franklin⁹, Nelly Joseph-Mathurin⁹, Alyssa Gonzalez⁹, Brian Gordon⁹, Julia Gray⁹, Emily Gremminger⁹, Alex Groves⁹, Jason Hassenstab⁹, Cortaiga Hellm⁹, Elizabeth Herries⁹, Laura Hoechst-Swisher⁹,

David Holtzman⁹, Russ Hornbeck⁹, Gina Jerome⁹, Sarah Keefe⁹, Deb Koudelis⁹, Yan Li⁹, Jacob Marsh⁹, Rita Martinez⁹, Kwasi Mawuenyega⁹, Austin McCullough⁹, Eric McDade⁹, John Morris⁹, Joanne Norton⁹, Kristine Shady⁹, Wendy Sigurdson⁹, Jennifer Smith⁹, Peter Wang⁹, Qing Wang⁹, Chengjie Xiong⁹, Jinbin Xu⁹, Xiong Xu⁹, Ricardo Allegrri¹⁰, Patricio Chrem Mendez¹⁰, Noelia Egido¹⁰, Aki Araki¹¹, Takeshi Ikeuchi¹¹, Kenji Ishii^{11,12}, Kensaku Kasuga¹¹, Jacob Bechara¹³, William Brooks¹³, Peter Schofield¹³, Sarah Berman¹⁴, Sarah Goldberg¹⁴, Snezana Ikonovic¹⁴, William Klunk¹⁴, Oscar Lopez¹⁴, James Mountz¹⁴, Neelesh Nadkarni¹⁴, Riddhi Patira¹⁴, Lori Smith¹⁴, Beth Snitz¹⁴, Sarah Thompson¹⁴, Elise Weamer¹⁴, Courtney Bodge¹⁵, Stephen Salloway¹⁵, Kathleen Carter¹⁶, Duc Duong¹⁶, Erik Johnson¹⁶, Allan Levey¹⁶, Lingyan Ping¹⁶, Nicholas T. Seyfried¹⁶, Colleen Fitzpatrick¹⁷, Helena Chui¹⁸, John Ringman¹⁸, Gregory S. Day¹⁹, Neill Graff-Radford¹⁹, Morgan Graham¹⁹, Sochenda Stephens¹⁹, Chrismary De La Cruz²⁰, Jill Goldman²⁰, Arlene Mejia²⁰, Katie Neimeyer²⁰, James Noble²⁰, Anna Diefenbacher²¹, Igor Yakushev²¹, Johannes Levin²¹, Jonathan Vöglein²¹, Jane Douglas²², Nick Fox²², Miguel Grilo²², Cath Mummery²², Antoinette O'Connor²², Bianca Esposito²³, Alison Goate²³, Alan Renton²³, Hisako Fujii²⁴, Michio Senda²⁴, Hiroyuki Shimada²⁴, Samantha Gardener²⁵, Ralph Martins²⁵, Hamid Sohrabi²⁵, Kevin Taddei²⁵, Susanne Gräber-Sultan²⁶, Lisa Hästler²⁶, Anna Hofmann²⁶, Mathias Jucke²⁶, Stephan Käser²⁶, Elke Kuder-Buletta²⁶, Christoph Laske²⁶, Oliver Preische²⁶, Christian Haass²⁷, Estrella Morenas-Rodriguez²⁷, Brigitte Nuscher²⁷, Ryoko Ihara¹², Akemi Nagamatsu¹², Yoshiki Niimi¹², Clifford Jack²⁸, Robert Koeppe²⁹, Neal Scott Mason³⁰, Colin Masters³¹ & Ulricke Obermüller³²

⁹School of Medicine, Washington University in St Louis, St Louis, MO, USA. ¹⁰Institute of Neurological Research Fleni, Buenos Aires, Argentina. ¹¹Niigata University, Niigata, Japan. ¹²Tokyo University, Tokyo, Japan. ¹³Neuroscience Research Australia, Sydney, New South Wales, Australia. ¹⁴University of Pittsburgh, Pittsburgh, PA, USA. ¹⁵Brown University–Butler Hospital, Providence, RI, USA. ¹⁶Emory University School of Medicine, Atlanta, GA, USA. ¹⁷Brigham and Women's Hospital–Massachusetts General Hospital, Boston, MA, USA. ¹⁸University of Southern California, Los Angeles, CA, USA. ¹⁹Mayo Clinic Jacksonville, Jacksonville, FL, USA. ²⁰Columbia University, New York, NY, USA. ²¹German Center for Neurodegenerative Diseases (DZNE), Munich, Germany. ²²University College London, London, UK. ²³Icahn School of Medicine at Mount Sinai, New York, NY, USA. ²⁴Osaka City University, Osaka, Japan. ²⁵Edith Cowan University, Perth, Western Australia, Australia. ²⁶German Center for Neurodegenerative Diseases (DZNE), Tübingen, Germany. ²⁷Ludwig-Maximilians University, Munich, Germany. ²⁸Mayo Clinic, Rochester, NY, USA. ²⁹University of Michigan, Ann Arbor, MI, USA. ³⁰University of Pittsburgh Medical Center, Pittsburgh, PA, USA. ³¹University of Melbourne, Parkville, Victoria, Australia. ³²Hertie Institute for Clinical Brain Research, Tübingen, Germany.

Methods

Mice

Mice were bred in-house or obtained from the Jackson Laboratory (JAX) or provided by the National Institutes of Health/National Institute on Aging (24-month-old mice). Mice were housed in a 12-h light–dark cycle in a temperature-controlled and humidity-controlled environment with water and food provided ad libitum. Mice were housed for at least 1 week at the animal facility before any experimentation. Both males and females were used in this study. The following mouse strains were used: C57BL/6J (WT; JAX 000664), C57BL/6-Tg (Ubc^{GFP}; JAX 004353), hemizygous B6SJL-Tg (APPSwFllon, PSEN1^{M146L}*L286V)6799Vas/Mmjax (5×FAD mice; JAX 008730), *Lyve1*^{Cre} (B6;129P2-*Lyve1*^{tm1.1(EGFP/cre)Cys}/J; JAX 012601), *Csf1r*^{fl/fl} (B6.Cg-*Csf1r*^{tm1.2Jwp}/J; JAX 021212) and *Aldh1l1*^{Cre/ERT2} (B6; JAX 031008). Sample sizes were chosen on the basis of standard power calculations (with $\alpha = 0.05$ and power of 0.8) performed for similar experiments that have been previously published. Animals from different cages, but within the same experimental group, were selected to ensure randomization. Mice from the same cage received different treatments (for example, in a cage of five mice, two mice received PBS-loaded liposomes and three mice received CLO-loaded liposomes). Treatment was given in a blind manner and could be identified by a corresponding ear tag (for example, for treatment A, the left ear was tagged whereas for treatment B, the right ear was tagged). All experiments were approved by the Institutional Animal Care and Use Committee of the University of Virginia and the Institutional Animal Care and Use Committee of the Washington University in Saint Louis.

Treatments with i.c.m. injections

Mice were anaesthetized using an intraperitoneal injection of KX cocktail (100 mg kg⁻¹ ketamine and 10 mg kg⁻¹ xylazine) diluted in 0.9% Na (saline) solution. The fur of the neck was shaved and cleaned with 70% iodine. Then, mice were placed in a stereotaxic frame to maintain the head in a fixed position, and an ophthalmic solution was applied to prevent dry eyes. The skin from the neck was longitudinally incised, and muscles were retracted using hooks to expose the cisterna magna. The solutions, diluted in aCSF, were injected using a 33-gauge Hamilton syringe (1–5 μ l; 2.5 μ l min⁻¹). The syringe was left in place for 1 min after injection to prevent backflow. For survival surgeries, the skin was sutured and mice were kept on a heating pad until fully awake. Mice received a subcutaneous injection of ketoprofen (2.5 mg kg⁻¹) at the end of the surgery.

To deplete PBMs, mice received an i.c.m. injection of CLO-loaded liposomes (5 μ l; 5 mg ml⁻¹; Fisher Scientific, CLD-8901). The control group consisted of mice that received an i.c.m. injection of PBS-loaded liposomes. The effect of PBM depletion was mostly studied 1 week after liposome injection to avoid any side effects from an inflammatory reaction due to the depletion. Moreover, at 1 week, we observed strong depletion (80–85% depletion), as previously described²⁸. We chose to wait for 1 month instead of 1 week to evaluate the mid-to-long-term effect of PBM depletion on plaque accumulation in the 5×FAD mouse model of AD.

To evaluate CSF flow dynamics in different contexts, Alexa 647-conjugated OVA (45 kDa; 5 μ l; 1 mg ml⁻¹ diluted in aCSF; Thermo Fisher Scientific, O34784), FITC-dextran (4 kDa; 5 μ l; 5 mg ml⁻¹ diluted in aCSF; Sigma-Aldrich, 46944), Texas Red dextran (3 kDa; 5 μ l; 1 mg ml⁻¹ diluted in aCSF; Fisher Scientific, D3328), fluorescent beads (0.1 μ m thick; 5 μ l; 1:5 dilution in aCSF; Life Technologies, F8888) or Dotarem (gadolinium-based MRI contrast agent; 0.754 kDa; 5 μ l; 0.5 mmol ml⁻¹; Guerbet) were injected through i.c.m. and mice were perfused 1 h later.

To evaluate the role of PBMs on CSF flow in old mice, 24-month-old mice received an i.c.m. injection of 5 μ l aCSF or M-CSF (10 μ g ml⁻¹ diluted in aCSF; Sigma-Aldrich, M9170). Six hours or 24 h later, mice received an i.c.m. injection of OVA to evaluate CSF flow.

To evaluate the effect of IFN γ on CSF flow, young adult mice (2–3 months old) received an i.c.m. injection of 1 μ l aCSF or recombinant IFN γ (20 μ g ml⁻¹ diluted in aCSF; Fisher Scientific, 485-MI-100/CF). Three hours later, mice received an i.c.m. injection of 5 μ l OVA to evaluate CSF flow.

To evaluate PBM phagocytosis, mice received an i.c.m. injection of pHrodo particles (1 mg ml⁻¹ in aCSF; Deep Red *Escherichia coli* bioparticles, Life Technologies, P35360). These particles emit 647 nm wavelength fluorescence only after being phagocytosed by cells (pH-dependent). Phagocytic activity was measured by pHrodo coverage by IHC, and pHrodo⁺ cells was quantified by flow cytometry.

Intrastriatal injections

Anaesthetized mice (through KX cocktail) were shaved on the top of the head and placed in a stereotaxic frame. After skin incision, a small craniectomy was made using a drill, and the different solutions were injected using a glass capillary (1 μ l; 0.2 μ l min⁻¹) (coordinates from the Bregma: anterior–posterior: +1.5 mm; medial–lateral: –1.5 mm; dorsal–ventral: +2.5 mm). The glass capillary was left in place for five additional minutes to prevent backflow. Mice were then sutured and placed on a heating pad until further experiments.

Dobutamine injection

For one experiment, mice received an intraperitoneal injection of dobutamine (40 μ g kg⁻¹ diluted in saline; Sigma Aldrich, D0676), a β_1 adrenergic agonist, or saline as a control, before CSF flow evaluation.

Proteomics analysis of CSF

CSF collection. Mice were anaesthetized using a KX cocktail. The fur of the neck was shaved and cleaned with 70% iodine. Mice were then placed in a stereotaxic frame to maintain the head in a fixed position, and an ophthalmic solution was applied to prevent dry eyes. The skin from the neck was longitudinally incised and muscles were retracted using hooks to expose the cisterna magna. A glass capillary was inserted into the cisterna magna to collect CSF, which was transferred into 1.5 ml Eppendorf tubes for further analyses.

Peptide preparation. CSF (7–10 μ l) samples from mice were dried in a speed-vac and solubilized with 30 μ l of SDS buffer (4% (w/v), 100 mM Tris-HCl pH 8.0, and 0.2% dichloroacetone (DCA)). The protein disulfide bonds were reduced using 100 mM dithiothreitol with heating to 95 °C for 10 min. Peptides were prepared as previously described using a modification of the filter-aided sample preparation method⁴². The samples were mixed with 200 μ l of 100 mM Tris-HCl buffer, pH 8.5, containing 8 M urea and 0.2% DCA (UA buffer). The samples were transferred to the top chamber of a 30,000 MWCO cut-off filtration unit (Millipore, part MRCFOR030) and spun in a microcentrifuge at 14,000 r.c.f. for 10 min. An additional 200 μ l of UA buffer was added, and the filter unit was spun at 14,000 r.c.f. for 15–20 min. The cysteine residues were alkylated using 100 μ l of 50 mM iodoacetamide (Pierce, A39271) in UA buffer. Iodoacetamide in UA buffer was added to the top chamber of the filtration unit.

The samples were gyrated at 550 r.p.m. for 30 min in the dark at room temperature using a thermomixer (Eppendorf). The filter was spun at 14,000 r.c.f. for 15 min, and the flow through was discarded. Unreacted iodoacetamide was washed through the filter with two sequential additions of 200 μ l of 100 mM Tris-HCl buffer, pH 8.5 containing 8 M urea and 0.2% DCA, and the samples were centrifuged at 14,000 r.c.f. for 15–20 min after each buffer addition. The flow through was discarded after each buffer exchange–centrifugation cycle. The urea buffer was exchanged with digestion buffer (DB; 50 mM ammonium bicarbonate buffer, pH 8, containing 0.2% DCA). Two sequential additions of DB (200 μ l) with centrifugation after each addition to the top chamber was performed. The top filter units were transferred to a new collection tube, and 100 μ l DB containing 1 mAU of LysC (Wako Chemicals,

129-02541) was added and samples were incubated at 37 °C for 2 h. Trypsin (1 µg; Promega, V5113) was added and samples were incubated overnight at 37 °C. The filters were spun at 14,000 r.c.f. for 15 min to recover the peptides in the lower chamber. The filter was washed with 5 µl of 100 mM ABC buffer and the wash was combined with the peptides. Residual detergent was removed by ethyl acetate extraction⁴². After extraction, the peptides were dried in a speed-vac concentrator (Thermo Scientific, Savant DNA 120 speed-vac concentrator) for 15 min. The dried peptides were dissolved in 1% (v/v) trifluoroacetic acid (TFA) and desalted using stage tips (C18) as previously described⁴³. The peptides were eluted with 60 µl of 60% (v/v) MeCN in 0.1% (v/v) formic acid (FA) and dried in a speed-vac (Thermo Scientific, Savant DNA 120 concentrator). The peptides were dissolved in 20 µl of 1% (v/v) MeCN in water. An aliquot (10%) was removed for quantification using a Pierce Quantitative Fluorometric Peptide Assay kit (Thermo Scientific, 23290).

The remaining peptides were transferred to autosampler vials (Sun-Sri, 200046), dried and stored at -80 °C.

Ultra performance liquid chromatography–Orbitrap mass spectrometry. The peptides were analysed using ultra performance liquid chromatography–Orbitrap mass spectrometry with the modifications described below. A volume of 2.5 µl of sample in 1% (v/v) FA (1%) was loaded onto a 75 µm i.d. × 50 cm Acclaim PepMap 100 C18 RSLC column (Thermo-Fisher Scientific) on an EASY nanoLC (Thermo Fisher Scientific) at a constant pressure of 700 bar at 100% buffer A (0.1% FA). Before sample loading, the column was equilibrated to 100% buffer A for a total of 11 µl at 700 bar pressure. Peptide chromatography was initiated with mobile phase A (1% FA) containing 2% buffer B (100% acetonitrile (ACN), 1% FA) for 5 min, then increased to 20% B over 100 min, to 32% B over 20 min, to 95% B over 1 min and held at 95% B for 19 min, with a flow rate of 250 nl min⁻¹. Data were acquired in data-dependent acquisition mode. The full-scan mass spectra were acquired with an Orbitrap mass analyzer with a scan range of $m/z = 325-1,500$ and a mass resolving power set to 70,000. Ten data-dependent high-energy collisional dissociations were performed with a mass resolving power set to 17,500, a fixed lower value of m/z of 110, an isolation width of 2 Da, and a normalized collision energy setting of 27. The maximum injection time was 60 ms for parent-ion analysis and product-ion analysis. The target ions that were selected for tandem mass spectrometry (MS/MS) were dynamically excluded for 30 s. The automatic gain control was set at a target value of 1×10^6 ions for full MS scans and 1×10^5 ions for MS2. Peptide ions with charge states of unassigned or one were excluded for higher energy collisional dissociation acquisition

Identification of proteins. MS raw data were converted to peak lists using Proteome Discoverer (v.2.1.0.81, Thermo Fisher Scientific). MS/MS spectra with charges greater than or equal to two were analysed using Mascot search engine (Matrix Science, v.2.7.0). Mascot was set up to search against a custom non-redundant UniProt database of mouse (version March 2021, 16,997 entries), assuming the digestion enzyme was trypsin with a maximum of 4 missed cleavages allowed. The searches were performed with a fragment ion mass tolerance of 0.02 Da and a parent ion tolerance of 20 ppm. Carbamidomethylation of cysteine was specified in Mascot as a fixed modification. Deamidation of asparagine, deamidation of glutamine, formation of pyro-glutamic acid from amino-terminal glutamine, acetylation of protein N terminus and oxidation of methionine were specified as variable modifications. Peptides and proteins were filtered at 1% false-discovery rate by searching against a reversed protein sequence database.

Intracranial pressure measurements

Mice were anaesthetized using a KX cocktail and placed in a stereotaxic frame. After the cisterna magna was exposed, a glass capillary containing a pressure sensor was inserted into the cisterna magna. A baseline

measure was done in saline solution. The capillary was left in place in the cisterna magna for 3 min. Intracranial pressure was recorded using FISO Evolution software (v. 2.2.0.0). Respiratory rates were also measured using this method (breaths per min).

Western blots of isolated brain blood vessels

Brains were homogenized in a 2-ml tissue grinder in 1.5 ml of microvesSEL isolation buffer (MIB; 15 mM HEPES, 147 mM NaCl, 4 mM KCl, 3 mM CaCl₂ and 12 mM MgCl₂), containing a cocktail of protease inhibitors (complete, mini, EDTA-free protease inhibitor cocktail, Sigma-Aldrich). Samples were then transferred into a 15-ml conical tube and centrifuged at 1,000g for 10 min at 4 °C. The supernatant was removed and the pellet was resuspended in 5 ml of MIB containing 18% dextran (from *Leuconostoc mesenteroides*, MW 60,000–90,000; Sigma-Aldrich) and spun at 4000g for 20 min at 4 °C. The resulting supernatant was discarded, and the pellet was resuspended in 1 ml of MIB. The homogenate was then filtered through a 20-µm nylon filter (PluriStrainer 20 µm, Fisher Scientific). Microvessels were retained on the filter, whereas the parenchymal fraction was contained in the filtrate. The vascular fraction was then rinsed from the filter with PBS containing 1% BSA and pelleted at 4,000g for 10 min. The pellet was re-suspended in 1.5 ml PBS and transferred into an Eppendorf tube and pelleted again at 4,000g for 10 min.

Isolated vessels were lysed in RIPA buffer (Bioworld) containing protease inhibitors, and protein concentration was determined using a bicinchoninic acid assay kit (Pierce). Thirty micrograms of protein was separated by PAGE on 7.5% Mini-Protean TGX precast protein gels (Bio-Rad) and transferred onto nitrocellulose membranes. Ponceau S (Sigma-Aldrich) was used to confirm loading of equal amounts of protein and to monitor the transfer procedure. After blocking with blocking buffer (TBS (50 mM Tris, 150 mM NaCl, pH 7.6) containing 0.1% Tween-20 and 5% milk), the membranes were probed overnight (4 °C) with a primary antibody (collagen IV antibody 134001, Bio-Rad, 1:500) diluted in blocking buffer. Membranes were rinsed in TBS containing 0.1% Tween-20 and incubated with appropriate horseradish peroxidase (HRP)-conjugated secondary antibody (donkey anti-goat IgG (Abcam ab97120, 1:10,000) diluted in blocking buffer.

Behavioural tests

Behavioural tests were conducted at least 1 h after the dark cycle started. Behavioural tests were conducted in the following sequence: elevated plus maze > open-field test > three-chamber social-interaction test > forced-swim test (group 1) or cued-fear conditioning test (group 2). Each behavioural test was conducted with 50 dB white noise and at least 2 days apart to prevent stress. Experimental and social target mice were handled for 3 days before starting the first experiment. Before any behavioural tests, cages were located in a dark room with 50 dB white noise for 30 min.

Three-chamber social-interaction test. The size of the three-chambered apparatus was 40 × 20 × 26 cm (width, height and depth, respectively), with a centre chamber that was 12 cm wide and side chambers that were 14 cm wide. Illuminance was kept at 50 lux. In the first session, the mouse could freely move around the entire three-chambered apparatus with two small containers in the left or right corner for 10 min (session 1). The mouse was then gently confined in the centre chamber while a new 'object' and a WT stranger mouse, 'stranger 1' (aged-matched C57BL/6J strain), was placed in one of the two plastic containers. The subject mouse was then allowed to freely explore all three chambers for 10 min (session 2). In the third session, the subject mouse was again gently guided to the centre chamber while the object was replaced with a WT 'stranger 2' mouse. The subject mouse again freely explored all three chambers for 10 min (session 3). Object and stranger exploration was defined by the nose of the subject mouse being oriented towards the target and coming within 2 cm of it as measured by EthoVision XT 15 (Noldus).

Open-field test. Mice were placed in an open-field box (35 × 35 × 35 cm) and recorded with a video camera for 60 min. The centre zone line was 9 cm apart from the edge. The testing room was illuminated at 0 lux. Mice movements were analysed using EthoVision XT 15 (Noldus).

Elevated plus maze. The elevated plus maze consisted of two open arms, two closed arms (for all arms, dimensions were 35 × 7 cm) and a centre zone, and was elevated to a height of 1 m above the floor. The illuminance of the closed arm was 80 lux, whereas the open arm was 120 lux. Mice were placed in the centre zone and allowed to explore the space for 8 min. Data were analysed using EthoVision XT 15 (Noldus).

Forced-swim test. Mice were placed into a 4-litre beaker that was three-quarter filled with tap water and recorded with a video camera on the top and side for 5 min. Water temperatures were kept at 20–21 °C, and the room was at 120 lux. Behaviour was manually analysed.

Cued-fear conditioning test. On the first day, mice were placed in the fear conditioning chamber (Ugo Basile). Before starting the experiment, 70% ethanol was sprayed once in the chamber. After 2 min of acclimation in white noise and the experimental condition, 1 kHz tone was applied for 20 s accompanied by 0.7 mA electric shock in the last 2 s. After 1 min of waiting time, tone-to-waiting was repeated three times in total. After repetition, mice were taken out of the conditioning chamber and returned to their home cage. On the second day (24 h after), the chamber was wiped with vanilla-flavoured oil, and the floor was exchanged with a grey-coloured plastic plate. Mice were placed in the chamber. After 2 min of acclimation to white noise, a 1 kHz tone was applied for 1 min, followed by 2 min of white noise. Mice were returned to the home cage. After 7 days of conditioning, the protocol for the second day was repeated. The data were analysed using activity parameters of EthoVision XT 15 (Noldus). Freezing time was measured during the waiting time (for the first day) and during the cue (for the second and eighth day).

Tissue collection and processing

Mice received a lethal intraperitoneal injection of euthasol (10% v/v in saline, 250 µl) and transcardially perfused with PBS containing 10 U ml⁻¹ heparin. In some experiments, mice received an intravenous injection of lectin (30 µl; Dylight 649 labelled *Lycopersicon Esculentum*; Fisher Scientific, DL-1178) 5 min before perfusion. After removal of the skin, muscles and mandibles, the head was drop-fixed in 4% PFA for 24 h. Then, the skull caps (skull and attached dorsal dura mater) were detached and brains were kept in 4% PFA for an additional 24 h (48 h in total). When collected, the dCLNs were drop-fixed in 4% PFA for 12 h. After fixation, the tissues were cryoprotected with 30% sucrose solution and frozen in Tissue-Plus OCT compound (Thermo Fisher Scientific). Brains were sliced (100-µm-thick sections) with a cryostat and kept in 24-well plates filled with PBS at 4 °C. The dCLNs were sliced (30-µm-thick sections) and collected on gelatin-coated slides. In one experiment, whole brains were post-fixed with 4% PFA, then washed with PBS and were directly stained and imaged by stereomicroscopy.

Ex vivo stereomicroscopy imaging

Mice received a lethal intraperitoneal injection of euthasol (10% v/v in saline, 250 µl) and transcardially perfused with PBS containing 10 U ml⁻¹ heparin. After removal of the skin, muscles and mandibles, the head was drop-fixed in 4% PFA for 24 h. Then, the skull caps (skull and attached dorsal dura mater) were detached and brains were kept in 4% PFA for an additional 24 h (48 h in total). The whole brains were then placed on a Petri dish and imaged by stereomicroscopy. For OVA measurements, whole brains were imaged using the following parameters: CY5 channel: zoom = 0.78, exposure time = 2 s. Quantification of OVA coverage at the MCA level was done using the following parameters: CY5 channel:

zoom = 5, exposure time = 500 ms. For bead or pHrodo experiments, brains were placed on the side, and quantifications were done using the following parameters: GFP or CY5 channels: zoom = 5, exposure time = 250 ms or 500 ms, respectively.

Light sheet microscopy

For whole brain imaging, the vDISCO method was used to clear the brain⁴⁴. In brief, mice received an i.c.m. injection of OVA (5 µl). One hour later, mice received an intravenous injection of lectin (30 µl) and were perfused 5 min later. Whole brain was post-fixed in 4% PFA for 24 h, then permeabilized and cleared using vDISCO protocol with passive tissue immersion. Brains were immersed in ethyl cinnamate (Sigma-Aldrich, W243019) and placed in chambered coverglass (Thermo Fisher, 155360) for light sheet imaging (LaVision BioTec).

IHC, imaging and quantifications

Tissues were rinsed in PBS and incubated in PBS 0.25% Triton X-100 with the following appropriate primary antibodies: rat anti-mouse CD206 (Bio-Rad MCA2235; 1:500); goat anti-mouse IBA1 (Abcam, ab5076; 1:500); Armenian hamster anti-mouse CD31 (Millipore Sigma, MAB1398Z; clone 2H8, 1:200); rabbit anti-mouse AQP4 (Millipore Sigma, A5971; 1:500); eFluor 660 conjugated anti-mouse LYVE1 (eBioscience, clone ALY7; 1:200); Alexa Fluor 594 conjugated anti-mouse I-A/I-E (MHCII; BioLegend, 107650; 1:200); rabbit anti-mouse laminin (Abcam, ab7463; 1:500); rabbit anti-mouse collagen IV (EMD Millipore, AB756P; 1:500); FITC-conjugated anti-mouse αSMA (Sigma Aldrich, F3777; 1:200); goat anti-mouse CD13 (R&D Systems, AF2335; 1:200); and rabbit anti-mouse Aβ (Cell Signaling Technology, 8243S, D54D2; 1:400). Sections were washed with a PBS solution containing 1:40,000 4',6-diamidino-2-phenylindole (DAPI) and mounted on Superfrost Plus slides (Fisher Scientific) and coverslipped with Aqua-Mount (Lerner) or ProLong Gold (Thermo Fisher). Slices were acquired using wide-field (Olympus, VS200-S6) or confocal (Leica, DMI-8 Stellaris) microscopes. Quantitative analyses of imaging measurements were performed using the Fiji package for ImageJ software. For brain tracer coverage measurements, six sections per mouse were used and manually thresholded to match observed signals. All six images were quantified as area of signal/total area (DAPI coverage) and averaged to obtain one value per mouse. For ECM coverage, whole brain sections, cortical regions or lectin⁺ αSMA⁺ large vessels (two whole sections per mouse) were manually thresholded and quantified as area of signal/total area.

In vivo fluorescent tracer dynamics evaluation

Mice were anaesthetized with a KX cocktail, the head was shaved and mice were placed on a stereotaxic frame. A lateral incision was made between the right eye and the right ear. The temporalis muscle was gently separated from the temporal bone. The surface of the skull was cleaned with a cotton bud. After i.c.m. injection of the fluorescent tracer, mice were positioned on a heating pad on their side to expose the right temporal bone under a stereomicroscope (Leica, M205 FA). The average time between the i.c.m. injection and the first image was 2 min. Mice were imaged over 1 h (240 frames in total: 4 frames per min). At the end of the imaging session, mice were euthanized using euthasol and tissues were collected for further analyses. For one experiment, mice were anaesthetized with KX or isoflurane (induction at 4.5% and continuously exposed at 0.75–2%). The fold increase was measured by calculating the ratio between *x* value divided by the minimal value.

For in vivo dCLN imaging, mice were anaesthetized with a KX cocktail, and the fur of the neck was shaved. After receiving an i.c.m. injection of OVA (5 µl), mice were placed on supine position, the skin from the neck was incised and retracted using hooks to expose the dCLNs. Live imaging was done under the stereomicroscope, as previously described³⁸ (average of 10 min between the i.c.m. injection and the beginning of the imaging).

MRI

Immediately after i.c.m. injection of Dotarem (a gadolinium-based MRI contrast agent; 0.754 kDa; 5 μ l) under KX anaesthesia (average time between i.c.m. injection and start of the MRI acquisitions: 2 min), mice were placed in a prone position on the MRI device (9.4 Tesla MRI, Bruker Biospin). During the imaging session, 0.5–0.8% isoflurane was provided through a nose mask to prevent mice from waking up. Body temperature and respiratory rates were monitored during imaging. Isoflurane levels were adjusted with respiratory rates, and body temperature was controlled using a heating pad. A series of post-contrast T1 Fast Low Angle SHot (FLASH)-3D weighted images were taken through the head with the following parameters: repetition time = 30 ms; echo time = 8 ms; number of echo images = 1; number of averages = 1; number of repetitions = 12; scan time = 272,640 ms per sequence (4 m 54 s); flip angle = 20, field of view = 160 \times 160 \times 80 μ m with a 128 \times 128 \times 64 matrix; spatial resolution = 125 \times 125 \times 125 μ m (8 pixels per mm; voxel size = 0.125 mm³), number of slices = 64; receiving coil 4 elements RF ARR 400 1H M. The total acquisition time was about 1 h per mouse (4 m 54 s \times 12 sequences per mouse). To calculate the volume of ventricles, mice were placed on supine position on the MRI device (7 Tesla MRI, Bruker Biospin). T2-weighted sequences were taken through the mouse head using the following parameters: repetition time = 3,000 ms, time to echo = 139 ms, field of view = 26 \times 20.5 mm, slice thickness = 0.13 mm, number of slices = 160 and number of excitations = 3 (total acquisition = 16 min per mouse).

In vivo photoacoustic microscopy

Mice were anaesthetized using a bolus of 4% isoflurane and medical air and maintained in 1–2% isoflurane during the surgical procedure. After fixing the head in a stereotaxic frame, a longitudinal incision was made to expose the skull. A small cranial window was made to be able to image brain blood vessels. Mice were sutured and allowed to recover after surgery in a clean cage. On the same day, mice were anaesthetized with 4% isoflurane and were transferred to the photoacoustic microscope, restrained using a nut and medical air was used for inhalation. The imaging session started 20 min after the mouse woke up. Thirty seconds after the acquisition started (average of 5,000 frames per mouse, frequency = 12 Hz), mice received a mixture of 10% CO₂ in medical air for 5 min. The vessel diameter fold-increase was measured by calculating the ratio between the measured values and the average of the first thousand values (before CO₂ challenge).

In vivo whisker stimulation

Mice were anaesthetized using a KX cocktail and placed in a stereotaxic frame. The body temperature was constantly monitored and adjusted using a heating pad. Whiskers on the right side of the mice were cut to about 0.5 cm. A longitudinal incision was made to expose the skull, and a thinned-skull window was made at the left barrel cortex to enable imaging of the distal part of the MCA. Mice were then placed under a stereomicroscope for imaging. Mechanical whisker stimulation was performed for 10 s, 6 s after the beginning of the imaging session. An average of ten videos were made per mouse (five with stimulations and five without stimulation), using the following parameters: bright-field channel; \times 16 zoom; exposure time: 200 ms (5 frames per s). Heart rates (beats per min) and basal arterial pulsations (pulsatile amplitude per vessel diameter) were measured using the videos without whisker stimulations.

Flow cytometry

Mice received a lethal intraperitoneal injection of euthasol (10% v/v in saline, 250 μ l) and transcardially perfused with PBS containing 10 U ml⁻¹ heparin. Lateral choroid plexuses were removed from half or whole brains. Brains were then digested for 40 min at 37 °C with 1.4 U ml⁻¹ of collagenase VIII and 35 U ml⁻¹ of DNase I in DMEM. The cell pellets were

washed and resuspended in FACS buffer and stained with the following antibodies (1:200 dilution; eBioscience): rat anti-mouse Ly6C (BioLegend, 128033, BV510); rat anti-mouse XCR1 (BioLegend, 148216, BV421); rat anti-mouse CD24 (BioLegend, 101819, Pacific Blue); rat anti-mouse Ly6G (BD Biosciences, 741587, BUV661); rat anti-mouse CD45 (BD Biosciences, 746947, BV750); rat anti-mouse CD19 (BD Biosciences, 751213, BUV615); rat anti-mouse CD11b (BD Biosciences, 741242, BUV563); rat anti-mouse TCRb (BD Biosciences, 748405, BUV805); rat anti-mouse CD4 (BD Biosciences, 563790, BUV395); rat anti-mouse F4/80 (BioLegend, 123133, BV605); rat anti-mouse CD64 (BD Biosciences, 139308, PerCP-Cy5.5); rat anti-mouse CD206 (BioLegend, 141710, AF488); rat anti-mouse CD38 (BioLegend, 102716, AF647 or BioLegend, 102719, Pacific Blue); and rat anti-mouse MHCII (BioLegend, 107641, BV650). Cell viability was determined using DAPI staining. Fluorescence data were acquired using Cytek Aurora spectral flow cytometer (Cytek) then analysed using FlowJo Software (Tree Star, v.5.0). For one experiment, mice received an i.c.m. injection of pHrodo particles (Life Technologies, P35360), which were detected by A647.

Electron microscopy

Mice received a lethal dose of euthasol by intraperitoneal injection and were transcardially perfused with warm Ringer's solution followed by perfusion with warm fixative containing 2.5% glutaraldehyde and 2% paraformaldehyde in 0.15 M cacodylate buffer (2 mM CaCl₂ at pH 7.4). Brains were transferred to a fixative solution and allowed to fix overnight at 4 °C. Brains were rinsed in cacodylate buffer 3 times for 10 min and fixed in 1% osmium tetroxide and 1.5% potassium ferrocyanide in cacodylate buffer for 1 h. Brains were then washed in ultrapure water 3 times for 10 min and stained in 1% thiocarbohydrazide solution for 1 h, followed by 1 h staining in aqueous 2% osmium tetroxide. Brains were rinsed in ultrapure water 3 times for 10 min and stained overnight in 1% uranyl acetate at 4 °C. The brains were then washed in ultrapure water 3 times for 10 min and stained with 20 mM lead aspartate at 60 °C for 30 min. After staining was complete, samples were washed in ultrapure water, dehydrated in a graded acetone series (50%, 70%, 90%, 100% three times) for 10 min in each step, and infiltrated with microwave assistance (Pelco BioWave Pro) into Durcupan resin. Samples were flat embedded and cured in an oven at 60 °C for 48 h. After resin curing, 70-nm-thick sections from brain cortex were prepared on copper grids, post-stained with uranyl acetate and Reynold's lead and imaged on a scanning electron microscope (Zeiss Merlin FE-SEM) using the following parameters: voltage = 5.00 kV; probe current = 3.0 nA; and WD = 6.9 mm.

MMP activity assay

The left hemisphere of the brain was homogenized in 6 volumes of PBS using a mini bead beater (Sigma Aldrich) and 2.3 mm diameter zirconia/silica beads (Biospec). The homogenate was then centrifuged in a microcentrifuge (Eppendorf) at 14,000 r.c.f. for 20 min at 4 °C. Protein (100 μ g) from the supernatant (representing the soluble fraction of the brain) was incubated with 25 μ m of the quenched fluorescent MMP substrate BML-P128-0001 (Enzo Life Sciences) in PBS and incubated at 37 °C for 15 min. Afterwards, the fluorescence of the cleaved fluorescent product was measured using a BioTek Synergy H1 plate reader (excitation/emission = 340 nm/440 nm).

RNA-seq

Mus musculus Dil-liposome leptomenigeal scRNA-seq. Sample preparation. Fifteen mice (3-month-old males; C57BL6/J) received an i.c.m. injection of 5 μ l (23 mg ml⁻¹) of Dil-liposomes (Liposoma, I-005). Mice were perfused with heparinized PBS and tissues were collected the next day. Subdural meninges were gently collected from the brains and were dissected in FACS buffer and digested in a digestion solution containing 1:50 collagenase VIII, 1:500 DNase, 1:50 FBS in FACS buffer for 15 min. Tissues were then mashed through 70- μ m strainers in 50-ml

Article

tubes containing FACS buffer and 10% FBS to stop enzymatic digestion. After centrifugation, the supernatant was removed and cells were resuspended in FACS buffer and transferred to a V-bottom plate. Cells were sorted, and only live Dll1⁺ cells were used for sequencing.

Single-cell data pre-processing. Reads were aligned to the mm10 genome using the Cellranger software pipeline (v.3.0.2) provided by 10x genomics. The resulting filtered gene-by-cell matrix of unique molecular identifier (UMI) counts was read in R using the read10xCounts function from the Droplet Utils package. Filtering was applied to remove low-quality cells by excluding cells expressing fewer than 200 or greater than 5,000 unique genes, having fewer than 1,000 or greater than 30,000 UMI counts, as well as cells with greater than 20% mitochondrial gene expression. Expression values for the remaining cells were then normalized using the scran and scater packages. The resulting log₂ values were transformed to the natural log scale for compatibility with the Seurat (v.3) pipeline^{45–47}.

Dimensionality reduction and clustering. The filtered and normalized matrix was used as input to the Seurat pipeline, and cells were scaled across each gene before the selection of the top 2,000 most highly variable genes using variance stabilizing transformation. Principal components analysis was conducted, and an elbow plot was used to select the first ten principal components (PCs) for t-distributed stochastic neighbour embedding (tSNE) analysis and clustering. Shared nearest neighbour (SNN) clustering optimized with the Louvain algorithm, as implemented by the Seurat FindClusters function, was performed before manual annotation of clusters based on the expression of canonical gene markers. Macrophages were then subset out, rescaled and clustered as above with the first 21 PCs and a resolution of 0.3.

***M. musculus* CLO depletion scRNA-seq. Sample preparation.**

To deplete PBMs, mice received an i.c.m. injection of CLO-loaded liposomes (5 µl; 5 mg ml⁻¹; Fisher Scientific; CLD-8901). The control group consisted of mice that received an i.c.m. injection of PBS-loaded liposomes. One week later, mice received a lethal intraperitoneal injection of euthasol (10% v/v in saline, 250 ml) and transcardially perfused with PBS containing 10 U ml⁻¹ heparin. Lateral choroid plexuses were gently removed, then whole brains were digested, myelin was removed and brain were stained with CD13 (to stain for mural cells), CD31 (endothelial cells) and CD45 (immune cells). Stromal cells (that is, endothelial plus mural cells) were then sorted and prepared for single-cell sequencing.

Single-cell data pre-processing. Reads were aligned to the mm10 genome using the Cellranger software pipeline (v.6.0.0) provided by 10x genomics. The resulting filtered gene-by-cell matrix of UMI counts was read in R using the read10xCounts function from the Droplet Utils package. Filtering was applied to remove low-quality cells by excluding cells expressing fewer than 200 or greater than 6,000 unique genes, having fewer than 1,000 or greater than 30,000 UMI counts, as well as cells with greater than 10% mitochondrial gene expression. Expression values for the remaining cells were then normalized using the scran and scater packages. The resulting log₂ values were transformed to the natural log scale for compatibility with the Seurat (v.3) pipeline^{45–47}.

Dimensionality reduction and clustering. The filtered and normalized matrix was used as input to the Seurat pipeline, and cells were scaled across each gene before the selection of the top 2,000 most highly variable genes using variance stabilizing transformation. Principal components analysis was conducted, and an elbow plot was used to select the first 30 PCs for tSNE analysis and clustering. SNN clustering optimized with the Louvain algorithm, as implemented by the Seurat FindClusters function, was performed before manual annotation of clusters based on the expression of canonical gene markers.

***M. musculus* brain scRNA-seq. Sample preparation.** Four mice (4-month-old males; Aldh1l1Cre-ER¹²/RosaCAG-tdTomato (C57BL6/J background)) received 100 µl of tamoxifen solution (20 mg ml⁻¹) on

three consecutive days to induce expression of tdTomato in astrocytes. A sham surgery of ligation of the lymphatic vessels afferent to the dCLNs consisting of skin incision and sternocleidomastoid muscle retraction was also performed. Afterwards, the skin was sutured and mice were allowed to recover on a heating pad until fully awake. Five weeks after surgery, mice were perfused with heparinized PBS. Brains were gently dissected using scissors and incubated in digestion solution 3 times for 20 min each (brains were also mechanically ground using descending diameter plastic pipettes between incubations). Tissues were then mashed through 70-µm strainers in 50-ml tubes containing FACS buffer and 10% FBS to stop enzymatic digestion. Myelin was removed by transferring samples into 3 ml FACS buffer containing 22% BSA and centrifuged (1,000g, 9 accelerations, 2 decelerations for 10 min at 4 °C). The remaining supernatant and the myelin layer were carefully removed, the pellet resuspended in FACS buffer and transferred to a V-bottom plate. FcBlock solution (1:50; 50 µl) was added to the wells and after 20 min, and antibodies (CD13 (BD Biosciences, 558744), CD31 (BioLegend, 102516) and CD45 (eBioscience, 550994); 1:200) were added (total volume = 200 µl). Cells were enriched in CD11b and negative for Ly6G and sorted in four different categories: CD45⁺CD13⁻CD31⁻ (immune), CD45⁻CD13⁺CD31⁻ (mural), CD45⁻CD13⁻CD31⁺ (endothelial) and CD45⁻tdTomato⁺ astrocytes. Overall, the recovered yield of astrocytes was low, and the maximum number of sorted astrocytes was used for sequencing. For the remaining cell populations, equal cell numbers were pooled and used for subsequent analyses.

Single-cell data pre-processing. Reads were aligned to the mm10 genome using the Cellranger software pipeline (v.6.0.0) provided by 10x genomics. The resulting filtered gene-by-cell matrix of UMI counts was read in R using the read10xCounts function from the Droplet Utils package. Filtering was applied to remove low-quality cells by excluding cells expressing fewer than 200 or greater than 7,000 unique genes, having fewer than 1,000 or greater than 50,000 UMI counts, as well as cells with greater than 15% mitochondrial gene expression. Expression values for the remaining cells were then normalized using the scran and scater packages. The resulting log₂ values were transformed to the natural log scale for compatibility with the Seurat (v.3) pipeline^{45–47}.

Dimensionality reduction and clustering. The filtered and normalized matrix was used as input to the Seurat pipeline, and cells were scaled across each gene before the selection of the top 2,000 most highly variable genes using variance stabilizing transformation. Principal components analysis was conducted, and an elbow plot was used to select the first 30 PCs for tSNE analysis and clustering. SNN clustering optimized with the Louvain algorithm, as implemented by the Seurat FindClusters function, was performed before manual annotation of clusters based on the expression of canonical gene markers.

Cell–cell interaction analysis. To evaluate potential cell–cell or ligand–receptor interactions in an unbiased way, the RNA Magnet package³³ was utilized with membrane, ECM, as well as both, ligand–receptor pairs queried and all vascular network cell types (arterial, capillary and venous endothelial cells, pericytes and VSMCs) included as anchors for RNAMagnetAnchors. Signalling interactions were also investigated with RNAMagnetSignaling, and the top signalling pair molecules were examined for both endothelial cells and mural cells with each other cell type present in the dataset. Macrophages were then subset out, rescaled and clustered as above with the first seven PCAs and a resolution of 0.3.

***M. musculus* 5×FAD scRNA-seq. Sample preparation.** Mice received a lethal intraperitoneal injection of euthasol (10% v/v in saline, 250 ml) and transcardially perfused with PBS containing 10 U ml⁻¹ heparin. Cortices were gently dissected in PBS, digested and stained after myelin removal with CD13 (to stain for mural cells), CD31 (endothelial cells) and CD45 (immune cells). Stromal cells (that is, endothelial and mural) and immune cells were then sorted and prepared for single-cell sequencing.

Single-cell data pre-processing. Reads were aligned to the mm10 genome using the Cellranger software pipeline (v.6.0.0) provided by 10x genomics. The resulting filtered gene-by-cell matrix of UMI counts was read in R using the read10xCounts function from the Droplet Utils package. Filtering was applied to remove low-quality cells by excluding cells expressing fewer than 200 or greater than 7,500 unique genes, having fewer than 1,000 or greater than 40,000 UMI counts, as well as cells with greater than 25% mitochondrial gene expression. Expression values for the remaining cells were then normalized using the scran and scater packages. The resulting \log_2 values were transformed to the natural log scale for compatibility with the Seurat (v.3) pipeline^{45–47}.

Dimensionality reduction and clustering. The filtered and normalized matrix was used as input to the Seurat pipeline, and cells were scaled across each gene before the selection of the top 2,000 most highly variable genes using variance stabilizing transformation. Principal components analysis was conducted, and an elbow plot was used to select the first 22 PCs for tSNE analysis and clustering. SNN clustering optimized with the Louvain algorithm, as implemented by the Seurat FindClusters function, was performed before manual annotation of clusters based on the expression of canonical gene markers.

Cell–cell interaction analysis. To evaluate potential cell–cell or ligand–receptor interactions in an unbiased way, the RNA Magnet package³³ was utilized with membrane, ECM, as well as both, ligand–receptor pairs queried and all vascular, stromal and mural cell types (arterial, capillary and venous endothelial cells, ependymal cells, fibroblasts, pericytes and VSMCs) included as anchors for RNAMagnetAnchors. Macrophages were then subset out, rescaled and clustered as above with the first 14 PCs and a resolution of 0.6.

Homo sapiens single-nucleus RNA-seq. Sample preparation. The Neuropathology Core of the Knight Alzheimer’s Disease Research Center and the Dominantly Inherited Alzheimer Network (DIAN) provided the parietal lobe tissue of postmortem brains for each sample. These samples were obtained with informed consent for research use and were approved by the review board of Washington University in St Louis. AD neuropathological changes were assessed according to the criteria of the National Institute on Aging–Alzheimer’s Association (NIA–AA). From the 60 frozen human parietal lobes, approximately 500 mg of tissue was cut and weighed on dry ice using sterile disposable scalpels. The parietal tissue was homogenized in ice-cold homogenization buffer (0.25 M sucrose, 150 mM KCl, 5 mM MgCl₂, 20 mM tricine-KOH pH 7.8, 0.15 mM spermine, 0.5 mM spermidine, EDTA-free protease inhibitor and recombinant RNase inhibitors) with a dounce homogenizer. Homogenates were centrifuged for 5 min at 500g, at 4 °C, to pellet the nuclear fraction. The nuclear fraction was mixed with an equal volume of 50% iodixanol and added on top of a 35% iodixanol solution for 30 min at 10,000g, at 4 °C. After myelin removal, the nuclei were collected at the 30–35% iodixanol interface. Nuclei were resuspended in nuclei wash and resuspension buffer (1% BSA and recombinant RNase inhibitors in PBS) and pelleted for 5 min at 500g and 4 °C. Nuclei were passed through a 40- μ m cell strainer to remove cell debris and large clumps. Nuclei concentration was manually determined using DAPI counterstaining and a haemocytometer. Nuclei concentration was adjusted to 1,200 nuclei per μ l and processed immediately following the 10x Genomics Single Cell Protocol instructions. We generated single-nucleus RNA-seq libraries using a 10x Chromium single cell reagent Kit v3 for 10,000 cells per sample and sequenced 50,000 reads per cell from 31 frozen human parietal lobes.

Single-cell data pre-processing. We prepared a pre-mRNA reference according to the steps detailed by 10x Genomics based on the GRCH38 (3.0.0) reference, and reads were aligned to the using the Cellranger software pipeline (v.3.0.2). The resulting filtered gene-by-cell matrices of UMI counts for each sample were read in R using the read10xCounts function from the Droplet Utils package. Filtering was applied

to remove low-quality cells by excluding cells expressing fewer than 500 or greater than 10,000 unique genes, having fewer than 2,000 or greater than 100,000 UMI counts, as well as cells with greater than 25% mitochondrial gene expression. Samples were then randomly assigned to one of five cohorts and individually processed to screen for the possible presence of perivascular macrophages. Expression values for the remaining cells in each cohort were merged by gene symbol into one dataframe and normalized using the scran and scater packages. The resulting \log_2 values were transformed to the natural log scale for compatibility with the Seurat (v.3) pipeline⁴⁷. Each was then scaled across each gene before the selection of the top 2,000 most highly variable genes using variance stabilizing transformation. Principal components analysis was conducted, and an elbow plot was used to select PCs for tSNE analysis and clustering. SNN clustering optimized with the Louvain algorithm, as implemented by the Seurat FindClusters function, was performed before manual annotation of clusters based on the expression of canonical gene markers. After removal of cells identified as neurons, oligodendrocytes, oligodendrocyte precursor cells and astrocytes, the remaining cells were split by original sample identity.

Integration, dimensionality reduction and clustering. Reference samples were chosen as those with more than 500 cells per sample and were prepped for integration utilizing the SCT normalization provided by Seurat with functions SelectIntegrationFeatures and PrepSCTIntegration. Sample integration was then performed with FindIntegrationAnchors specifying a k.filter = 100 and the reference samples determined above, and IntegrateData. Principal components analysis was conducted, and an elbow plot was used to select the first 30 PCs for tSNE analysis and clustering. SNN clustering optimized with the Louvain algorithm, as implemented by the Seurat FindClusters function, was performed before manual annotation of clusters based on the expression of canonical gene markers.

Differential expression. For analysis of differentially expressed genes between conditions, each cluster was filtered to include genes that had at least 5 transcripts in at least 5 cells, then the top 2,000 highly variable genes were determined and included for further analysis using the SingleCellExperiment modelGeneVar and getTopHVGs functions. After filtering, observational weights for each gene were calculated using the ZINB-WaVE zinbFit and zinbwave functions⁴⁸. These were then included in the edgeR model, which was created with the glmFit function, by using the glmWeightedF function^{49,50}. Results were then filtered using a Benjamini–Hochberg-adjusted *P* value threshold of less than 0.05 as statistically significant.

Pathway enrichment. Over-representation enrichment analysis with Fisher’s exact test was used to determine significantly enriched Gene ontology terms (adjusted *P* < 0.05) for the sets of significantly differentially expressed genes. For each gene set, genes were separated into upregulated and downregulated, and separately, the enrichGO function from the clusterProfiler package was used with a gene set size set between 10 and 500 genes and *P* values adjusted using Benjamini–Hochberg correction.

Statistical analyses and reproducibility

All data are presented as the mean \pm s.e.m. All the experiments (except single-cell and single-nucleus RNA-seq data) were repeated independently at least two times (biological replicates). Statistical significance was determined using two-tailed unpaired Welch’s *t*-test (nonparametric) when comparing two independent groups or by paired *t*-test when comparing values from the same group. For comparisons of multiple factors, one-way or two-way analysis of variance (ANOVA) with appropriate multiple-comparisons tests were used. Statistical analyses were performed using Prism 9.0 (GraphPad software). Exact *P* values are all provided in figures. We provide all raw data and the statistical analyses as a PRISM file in Supplementary Data 1. All experiments were done blinded, and groups were revealed only after all the analyses were performed.

Reporting summary

Further information on research design is available in the Nature Research Reporting Summary linked to this article.

Data availability

Mouse single-cell mRNA sequencing data are available at the Gene Expression Omnibus under the accession number GSE188285. The human single-nucleus data from the Knight ADRC is publicly available by request from the National Institute on Aging Genetics of Alzheimer's Disease Data Storage Site with accession number NG00108.v1 (<https://www.niagads.org/datasets/ng00108>). To access the data from the DIAN brain bank, special request must be made using this URL: <https://dian.wustl.edu/our-research/for-investigators/>.

Code availability

Custom code used to analyse the mRNA sequencing data is freely available at <https://doi.org/10.5281/zenodo.7047054>.

42. Erde, J., Loo, R. R. O. & Loo, J. A. Improving proteome coverage and sample recovery with enhanced FASP (eFASP) for quantitative proteomic experiments. *Methods Mol. Biol.* **1550**, 11–18 (2017).
43. Rappsilber, J., Mann, M. & Ishihama, Y. Protocol for micro-purification, enrichment, pre-fractionation and storage of peptides for proteomics using StageTips. *Nat. Protoc.* **2**, 1896–1906 (2007).
44. Cai, R. et al. Panoptic imaging of transparent mice reveals whole-body neuronal projections and skull–meninges connections. *Nat. Neurosci.* **22**, 317–327 (2019).
45. Lun, A. T. L., McCarthy, D. J. & Marioni, J. C. A step-by-step workflow for low-level analysis of single-cell RNA-seq data with Bioconductor. *F1000Research* **5**, 2122 (2016).
46. McCarthy, D. J., Campbell, K. R., Lun, A. T. L. & Wills, Q. F. Scater: pre-processing, quality control, normalization and visualization of single-cell RNA-seq data in R. *Bioinformatics* **33**, 1179–1186 (2017).
47. Butler, A., Hoffman, P., Smibert, P., Papalexi, E. & Satija, R. Integrating single-cell transcriptomic data across different conditions, technologies, and species. *Nat. Biotechnol.* **36**, 411–420 (2018).
48. Van den Berge, K. et al. Observation weights unlock bulk RNA-seq tools for zero inflation and single-cell applications. *Genome Biol.* **19**, 24 (2018).
49. Robinson, M. D., McCarthy, D. J. & Smyth, G. K. edgeR: a Bioconductor package for differential expression analysis of digital gene expression data. *Bioinformatics* **26**, 139–140 (2010).
50. Hong, G., Zhang, W., Li, H., Shen, X. & Guo, Z. Separate enrichment analysis of pathways for up- and downregulated genes. *J. R. Soc. Interface* **11**, 20130950 (2014).

Acknowledgements We thank S. Smith for editing the manuscript; S. Blackburn, N. Al-Hamadani, X. Wang and E. Griffin for animal care; S. Brophy for laboratory management; all the members of the Kipnis Laboratory for their valuable comments during numerous discussions of this work; all the members of the Washington University Center for Cellular

Imaging core (WUCCI) for their valuable contribution of electron microscopy imaging; staff at the University of Virginia Flow Cytometry Core and from the Sequencing Core for their help with cell sorting and sequencing; all the members of the Washington University Small Animal MR Imaging Facility and the University of Virginia Molecular Imaging Core Facility for their help in MRI. We acknowledge the expert technical assistance of Y. Mi, P. Erdmann-Gilmore, A. Davis and R. Connors for the CSF proteomics experiment performed at the Washington University Proteomics Shared Resource (WU-PSR), and R. Reid Townsend (Director) and R. Sprung and T. Zhang (Co-directors); the staff of the Neuropathology Cores and other personnel of the Charles F. and Joanne Knight Alzheimer's Disease Research Center (ADRC); and the altruism of the participants and their families and contributions of the Knight ADRC and DIAN research and support staff at each of the participating sites for their contributions to this study. This work was supported by grants from the National Institutes of Health/National Institute on Aging (AG034113, AG057496, AG078106), the Cure Alzheimer's Fund and the Ludwig Foundation to J.K.; AG057777 and AG067764 to O.H.; and AG062734 to C.M.K. O.H. is an Archer Foundation Research Scientist. The WU-PSR is supported in part by the WU Institute of Clinical and Translational Sciences (NCATS UL1 TR000448), the Mass Spectrometry Research Resource (NIGMS P41 GM103422; R24GM136766) and a Sitman Comprehensive Cancer Center Support grant (NCI P30 CA091842). The Neuropathology Cores and the Charles F. and Joanne Knight ADRC are supported by P30 AG066444, P01AG026276 and P01AG03991. Data collection and sharing for this project was supported by the DIAN (UFIAG032438) funded by the National Institute on Aging (NIA), the German Center for Neurodegenerative Diseases (DZNE), Raul Carrea Institute for Neurological Research (FLENI), partial support by the Research and Development Grants for Dementia from Japan Agency for Medical Research and Development, AMED, and the Korea Health Technology R&D Project through the Korea Health Industry Development Institute (KHIDI). This manuscript has been reviewed by DIAN Study investigators for scientific content and consistency of data interpretation with previous DIAN Study publications. The illustrations of the mice and MRI are freely available from Servier Medical Art (<https://smart.servier.com>). The brain cartoon and the summary illustration were created by the authors.

Author contributions A.D. designed and performed experiments, analysed and interpreted data, created the figures and wrote the manuscript. S.D. and S.E.S. performed experiments, analysed and interpreted data. F.Z. and S.H. performed the photoacoustic imaging experiment. Z.P. performed the live imaging on dCLNs. S.B. assisted in experiments and data analyses. J.R. and T.M. provided intellectual contribution and assisted in experiments. T.D. performed the mouse scRNA-seq data analyses, analysis of human single-nucleus RNA-seq data and participated in methods writing. K.K. performed the behavioural experiments and analyses. O.H. supervised and interpreted the scRNA-seq data analysis. C.M.K., R.J.B., R.P., M.F., J.C. and P.S. generated the datasets for the DIAN network. G.J.R. provided *Lyve1^{Cre}; Csf1r^{fl/fl}* mice and intellectual contribution. I.S. assisted with animal surgeries and blinded data analyses and quantifications. J.K. designed the experiments, provided resources and intellectual contribution, oversaw data analysis and interpretation, and wrote the manuscript.

Competing interests J.K. is a scientific advisor and collaborator with PureTech. J.K. and A.D. are holding provisional patent applications related to the findings described herein. R.J.B. co-founded and is on the scientific advisory board of C2N Diagnostics. C2N Diagnostics has licensed certain anti-tau antibodies to AbbVie for therapeutic development. He receives research support from Biogen, Eisai and the DIAN-TU Pharma Consortium. He is also an advisor to Amgen and Hoffman La-Roche.

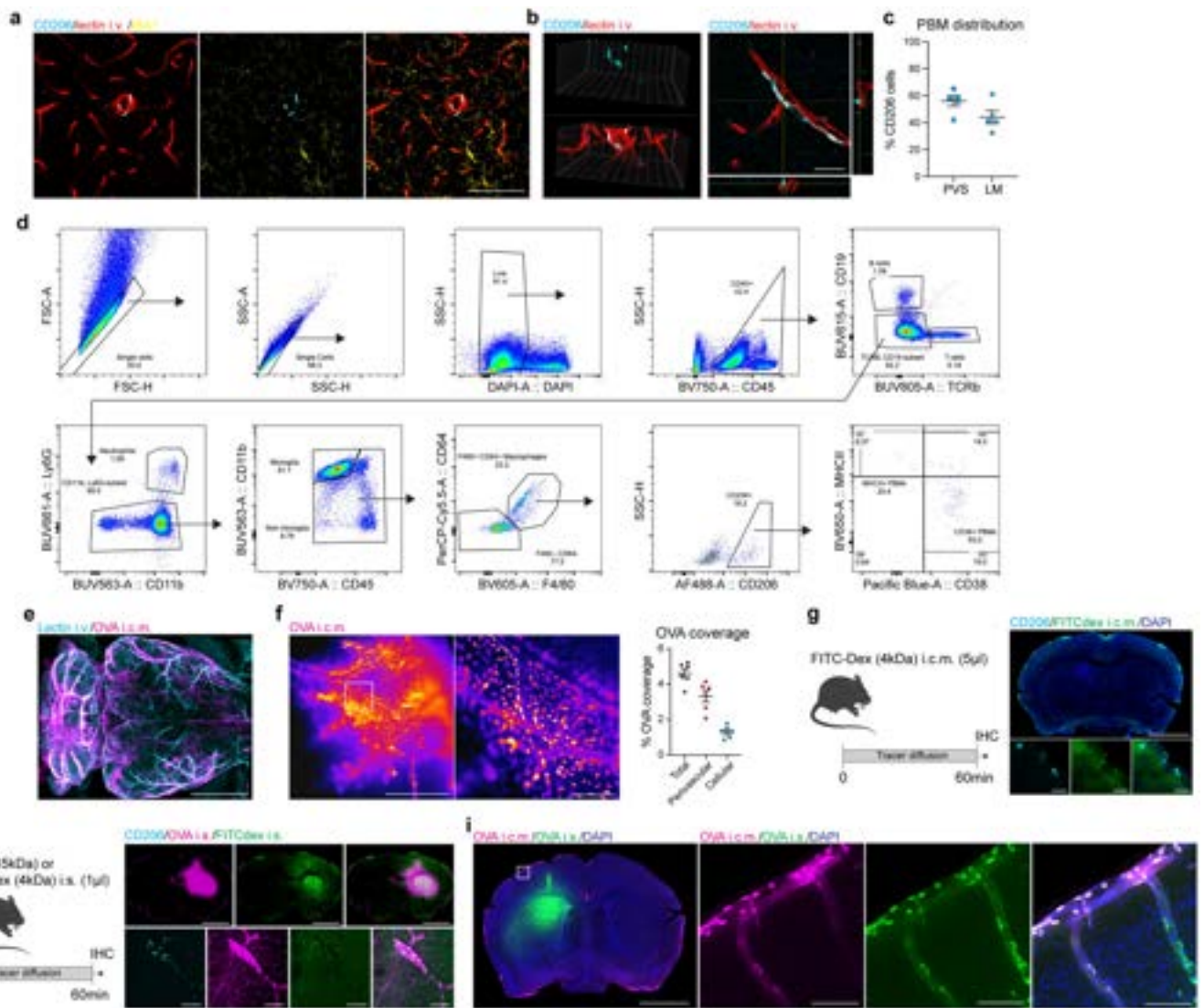
Additional information

Supplementary information The online version contains supplementary material available at <https://doi.org/10.1038/s41586-022-05397-3>.

Correspondence and requests for materials should be addressed to Antoine Drieu or Jonathan Kipnis.

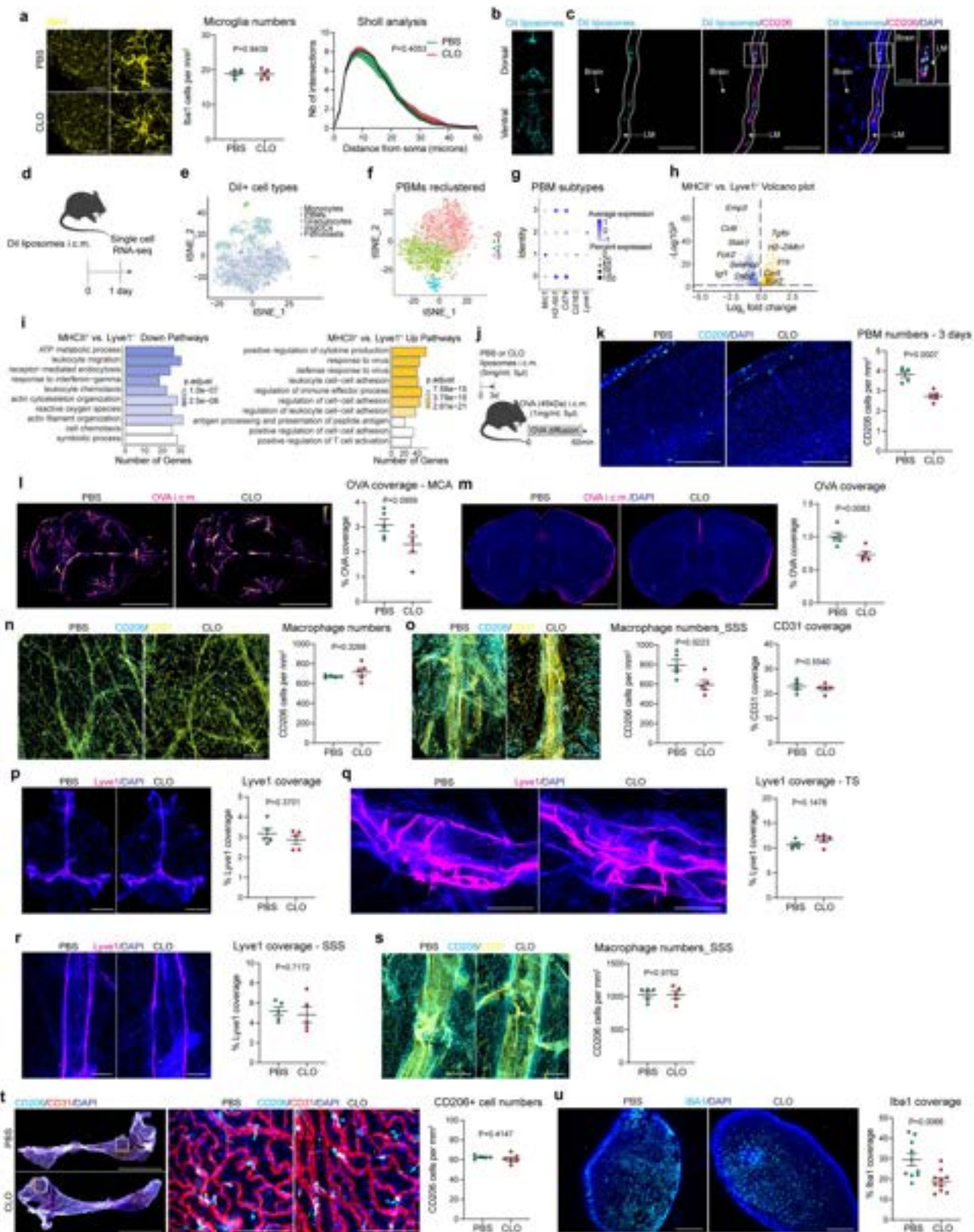
Peer review information Nature thanks Kiavash Movahedi and the other, anonymous, reviewer(s) for their contribution to the peer review of this work.

Reprints and permissions information is available at <http://www.nature.com/reprints>.



Extended Data Fig. 1 | PBMs are distinct from microglia and sample CSF and ISF. **a**, CD206⁺ PBMs (cyan) are easily distinguishable from IBA1⁺ microglia (yellow) and are located at the vicinity of i.v. lectin⁺ large blood vessels (red). Scale bar, 100 μ m. **b**, PBMs are located outside of the brain vasculature, in the perivascular space. **c**, Quantification of whole brain sections showing spatial distribution of PBMs through both perivascular space (PVS) and leptomeninges (LM). Scale bar, 20 μ m. $n = 5$ mice. **d**, Gating strategy for PBM detection. PBMs were defined as DAPI⁺ CD45⁻ TCR β ⁻ CD19⁻ CD11b⁻ CD64^{hi} F4/80^{hi} CD206⁺ cells. PBMs can be divided in subtypes using MHCII and CD38. **e**, WT mice received an i.c.m. injection of Alexa-647 conjugated ovalbumin (OVA; 45 kDa; 1 mg/ml; 5 μ l). One hour after OVA injection, mice received an i.v. injection of Alexa-594 conjugated lectin (30 μ l) and were perfused five minutes later. Maximum projection image obtained by light sheet microscopy from a cleared mouse brain showing brain OVA (magenta) distribution at the vicinity of i.v.-injected lectin⁺ blood vessels (cyan). Scale bar, 1mm. **f**, WT mice received an i.c.m. injection of Alexa-647 conjugated ovalbumin (OVA; 45 kDa; 1 mg/ml; 5 μ l). Mice

were perfused one hour after OVA injection. Representative stereomicroscopy images showing whole brain OVA distribution from the distal part of the middle cerebral artery (MCA), and quantification of both perivascular and cellular OVA distribution. Scale bars, 1mm and 200 μ m (inset). $n = 6$ mice. **g**, Experimental schematic: WT mice received an i.c.m. injection of FITC Dextran (FITC-Dex; 4 kDa; 10 mg/ml; 5 μ l) and brain were harvested one hour later. Brain coronal sections were stained for anti-CD206 (cyan) and DAPI. Scale bars, 2 mm and 50 μ m (insets). **h**, Experimental schematic: WT mice received an intrastriatal (i.s.) injection of a cocktail containing 0.5 μ l of FITC-Dex (10 mg/ml; green) and 0.5 μ l of OVA (1 mg/ml; magenta) and brains were harvested one hour later. Brains were then stained for anti-CD206 (cyan). Scale bars, 2 mm and 50 μ m (insets). **i**, Mice received an i.s. injection of A488-OVA (green) and an i.c.m. injection of A647-OVA (magenta) one hour later. Mice were perfused one hour later (two hours after the i.s. injection). Some cells sampled both i.s. and i.c.m. OVAs. Scale bars, 2 mm and 100 μ m (inset). All data are presented as mean values \pm SEM. The illustration of mice in **g** and **h** are from Servier Medical Art, CC BY 3.0.

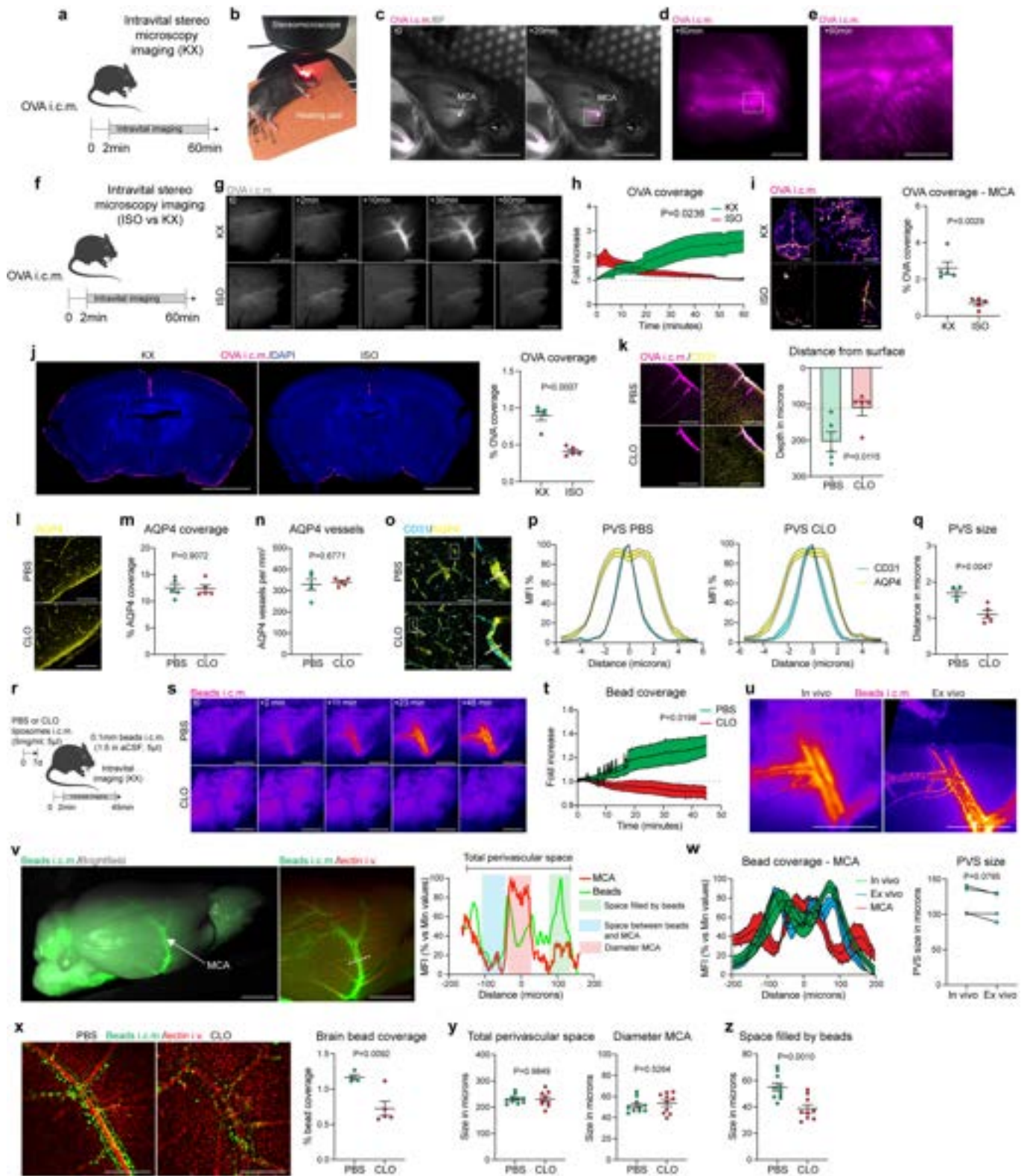


Extended Data Fig. 2 | See next page for caption.

Extended Data Fig. 2 | Effect of PBM depletion. **a**, WT mice received an i.c.m. injection of clodronate-loaded liposomes (CLO) or PBS-loaded liposomes (PBS). Microglial cells were identified using anti-IBA1 staining (yellow). Cells that were not in the leptomeninges and CD206⁻ were used for quantifications of cell numbers and Sholl analysis. Scale bars, 100 μ m and 20 μ m. n = 5 mice/group, two-tailed unpaired Welch's *t*-test; repeated measures 2-way ANOVA with Geisser-Greenhouse correction. **b**, WT mice received an i.c.m. injection of Dil-liposomes (5 mg/ml; 5 μ l) and mice were perfused 24 h later. Representative images showing Dil-liposome coverage in whole brains. Scale bar: 2mm. **c**, Representative images showing Dil-liposome (cyan) uptake by CD206⁺ PBMs (magenta) in leptomeninges (LM) co-stained for DAPI. Scale bars: 50 μ m and 10 μ m (inset). **d**, Experimental schematic: Twenty-four hours after i.c.m. injection of Dil-liposomes, leptomeninges were harvested, Dil-positive cells were sorted and single-cell RNA sequencing was performed. **e**, tSNE plot showing Dil-positive cells: monocytes, PBMs, granulocytes, migratory dendritic cells (migDCs), fibroblasts and NK/T cells. **f**, Single-cell RNA sequencing demonstrating 4 PBM clusters. **g**, Dot plots showing *Mrc1*, *H2-Ab1*, *Cd74*, *Cd163* and *Lyve1* gene expression in the 4 PBM subtypes. **h**, Volcano plot corresponding to down- and up-regulated genes comparing MHCII^{hi} vs. Lyve1^{hi} PBMs. *F*-test with adjusted degrees of freedom based on weights calculated per gene with a zero-inflation model and Benjamini-Hochberg adjusted P values. **i**, GO Pathway analysis showing up- and down-regulated pathways comparing MHCII^{hi} vs. Lyve1^{hi} PBMs. Over-representation test. **j**, Experimental schematic: WT mice received an i.c.m. injection of CLO or PBS liposomes. OVA was injected i.c.m. three days later and mice were perfused one hour later. **k**, Representative images showing CD206⁺ PBMs (cyan) on brain coronal section co-stained for DAPI, and corresponding quantification. Scale bar, 200 μ m. n = 5 mice/group; two-tailed unpaired Welch's *t*-test. **l**, Representative images and quantification of OVA distribution in whole brains one hour after OVA injection. Scale bar, 5mm. **m**, Representative images and quantification of OVA coverage in brain coronal sections. Scale bar, 2 mm. For **l** and **m**: n = 5 mice/group; two-tailed unpaired Welch's *t*-test. **n**, Representative images from non-superior sagittal sinus region of the dura mater three days after CLO treatment co-stained for anti-CD206 (cyan) and anti-CD31 (yellow) and corresponding quantifications. **o**, Representative images from the superior sagittal sinus region from the dura mater three days after CLO treatment co-stained for anti-CD206 (cyan) and anti-CD31 (yellow), and corresponding quantifications. For **n** and **o**: Scale bars, 200 μ m; n = 5 mice/group; two-tailed unpaired Welch's *t*-test. **p–u**, WT mice received an i.c.m. injection of CLO or PBS liposomes. Tissues were harvested one week later. **p**, Representative images of total Lyve1 (magenta) coverage in the dura mater co-stained for DAPI and corresponding quantification. Scale bar, 3 mm. **q**, High magnification images showing LYVE1 staining at the transverse sinus level co-stained for DAPI and corresponding quantification. Scale bar, 500 μ m. **r**, High magnification images showing LYVE1 staining at the superior sagittal sinus level co-stained for DAPI and corresponding quantification. Scale bar, 200 μ m. **s**, High magnification images showing CD206 staining (cyan) co-stained for anti-CD31 (yellow) and corresponding quantification. Scale bar, 500 μ m. For **p–s**: n = 5 mice/group; two-tailed unpaired Welch's *t*-test. **t**, Representative images from lateral choroid plexuses whole mounts co-stained for anti-CD206 (cyan), anti-CD31 (red) and DAPI with corresponding high magnifications and quantification. Scale bars, 2mm and 200 μ m (insets). n = 5 mice treated with PBS, and 6 mice treated with CLO; two-tailed unpaired Welch's *t*-test. **u**, Representative images from deep cervical lymph nodes co-stained for anti-IBA1 (cyan) and DAPI and corresponding quantification. Scale bar, 200 μ m. n = 10 mice/group; two-tailed unpaired Welch's *t*-test. All data are presented as mean values \pm SEM. The illustrations of mice in **d** and **j** are from Servier Medical Art, CC BY 3.0.

Extended Data Fig. 3 | CSF flow after PBM depletion. **a**, One week after PBM depletion, mice received an i.c.m. injection of FITC-Dextran (FITCdex; 4 kDa; 5 μ l), brains were harvested one hour later and FITCdex (green) coverage was measured on coronal sections co-stained for DAPI. Representative images and corresponding quantifications are shown. Scale bar, 2 mm. $n = 5$ mice/group; two-tailed unpaired Welch's t -test. **b**, One week after PBM depletion, mice received an i.c.m. injection of Texas Red (3 kDa; 5 μ l), brains were harvested one hour later and Texas Red (red) coverage was measured on coronal sections co-stained for DAPI. Representative images and corresponding quantifications are shown. Scale bar, 2 mm. $n = 4$ mice treated with PBS, and 5 mice treated with CLO; two-tailed unpaired Welch's t -test. **c**, One week after PBM depletion, mice received an intrastriatal injection of OVA (45 kDa; 1 μ l) and brains were harvested one hour later. Representative images and corresponding quantifications are shown. Scale bar, 2 mm. $n = 4$ mice treated with PBS, and 5 mice treated with CLO; two-tailed unpaired Welch's t -test. **d**, One week after PBM depletion, mice received an intrastriatal (i.s.) injection of FITC-Dextran (FITCdex; 4 kDa; 1 μ l) and brains were harvested one hour later. Representative images and corresponding quantifications are shown. Scale bar, 2 mm. $n = 4$ mice/group; Two-tailed unpaired Welch's t -test. **e**, One week after CLO or PBS liposome injection, mice were anesthetized, and a glass capillary was inserted i.c.m. to collect CSF for proteomic analyses. **f**, Volcano plot corresponding to down- and up-regulated proteins in CSF comparing PBM-depleted and control mice. F -test with adjusted degrees of freedom based on weights calculated per gene with a zero-inflation model and Benjamini-Hochberg adjusted P values. **g**, Corresponding GO Pathway analysis showing down- and up-regulated pathways in PBM-depleted and control mice. Over-representation test. **h**, Sunburst plot representing the location of the upregulated CSF-derived neuronal/synaptic-related proteins after PBM depletion. **i-k**, Quantification of relative spectral counts for **i**, Clusterin (CLU); **j**, Apolipoprotein E (APOE) and **k**, Amyloid Precursor Peptide (APP). For **e-k**: $n = 4$ mice treated with PBS, and 5 mice treated with CLO; two-tailed unpaired Welch's t -test. **l**, MRI based

T2-weighted anatomical sequences were performed before and one week after PBM depletion. **m**, Representative T2 images showing lateral ventricles (in hypersignal) before and after PBM depletion. Scale bar, 2 mm. **n**, Quantification of ventricle volume in mm^3 . $n = 5$ mice/group; one-way ANOVA with Tukey multiple comparisons test. **o**, Intracranial pressure was measured one- (7d) and three (21d) weeks after PBM depletion. $n = 5$ mice treated with PBS, 7 mice treated with CLO at 7d; 6 mice treated with PBS, and 7 mice treated with CLO at 21d; two-way ANOVA with Sidak's multiple comparisons test. **p**, Sagittal view of a T1-FLASH 3D image showing Dotarem (0.754 kDa; 5 μ l) accumulation in different brain compartments, including the olfactory bulbs (OB), the lateral ventricles (Lat vtl) and the middle cerebral artery (MCA). Scale bar, 3 mm. **q**, Representative T1-FLASH 3D images showing Dotarem distribution at the MCA level over time. Scale bar, 3 mm. **r**, Quantification of Dotarem signal fold increase over an hour. $n = 5$ mice treated with PBS, and 7 mice treated with CLO; repeated measures 2-way ANOVA with Geisser-Greenhouse correction. **s**, One week after CLO or PBS liposome injection, mice received an i.c.m. injection of OVA, and deep cervical lymph nodes (dCLNs) were harvested one hour later. **t**, Representative images showing OVA coverage on dCLN sections. Scale bar, 200 μ m. **u**, Quantification of dCLN area. **v**, Quantification of OVA coverage. For **u** and **v**: $n = 10$ mice/group; two-tailed unpaired Welch's t -test. **w**, One week after CLO or PBS liposome injection, mice received an i.c.m. injection of OVA and then placed in supine position under the stereomicroscope for dynamic imaging of OVA diffusion in the exposed lymph nodes. **x**, Representative images showing OVA coverage in dCLNs over time. Scale bar, 500 μ m. **y**, Quantifications of both OVA influx (left) and efflux (right) over time. $n = 3$ mice treated with PBS, and 7 mice treated with CLO; repeated measures 2-way ANOVA with Geisser-Greenhouse correction. **z**, Proportion of mice that showed OVA outflow from dCLNs. All data are presented as mean values \pm SEM. The illustrations of mice in **e**, **s** and **w** are from Servier Medical Art, CC BY 3.0.

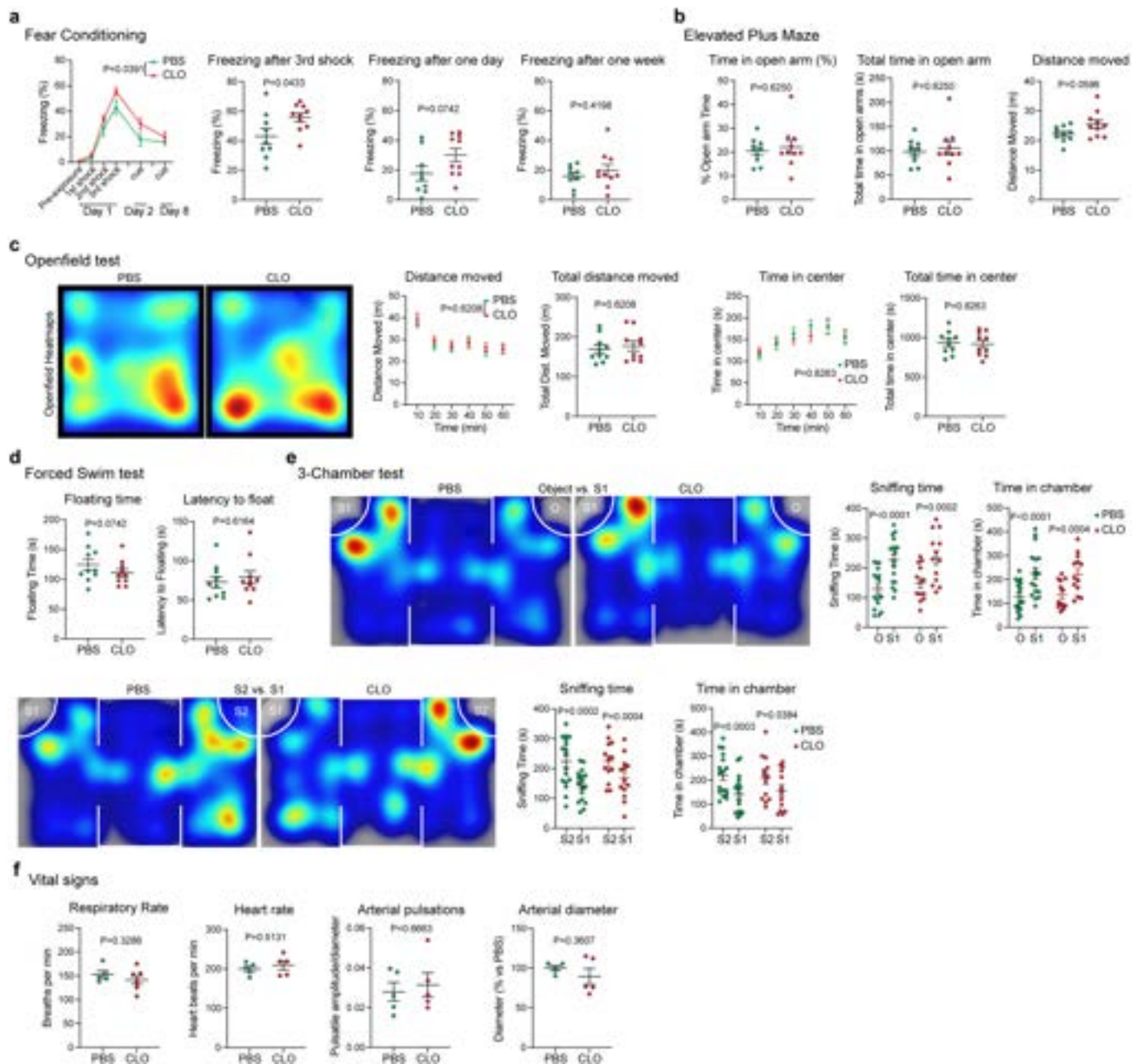


Extended Data Fig. 4 | See next page for caption.

Extended Data Fig. 4 | *In vivo* recording of tracer diffusion at the middle cerebral artery (MCA) level and evaluation of the perivascular space.

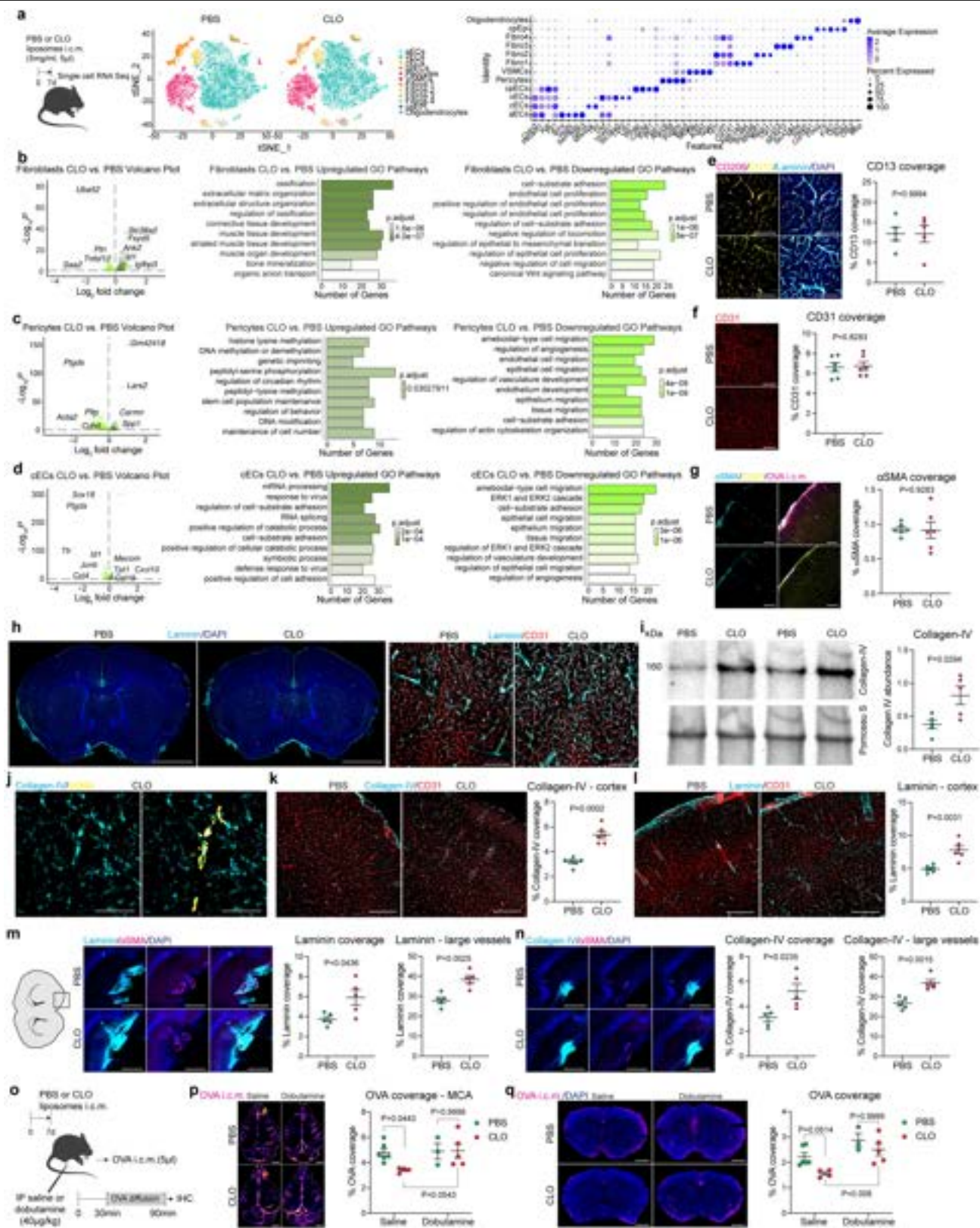
A, Experimental schematic: One week after CLO or PBS liposome injection, mice were placed in a stereotaxic frame, the top and the right side of the head were shaved, the skin was incised, and the right temporalis muscle was gently removed. **b**, After cleaning the area with a cotton bud, mice received an i.c.m. injection of OVA and were immediately placed on their side under the stereomicroscope. **c**, Example of OVA distribution at the middle cerebral artery level (MCA) before and 20min after injection. Scale bar, 5 mm. **d**, Inset of **c**. Higher magnification image showing OVA distribution one hour after injection. The tracer is located around the vessel, at the perivascular level. Scale bar, 1 mm. **e**, High magnification from **d** showing that OVA can be sampled by perivascular cells. Scale bar, 100 μ m. **f**, Experimental schematic: mice were anesthetized with either KX or isoflurane (4% induction, 1-2% during dynamic imaging) and received an i.c.m. injection of OVA. Mice were maintained with the same anesthesia regime during the dynamic imaging. **g**, Representative images showing OVA distribution over time. Scale bar, 1 mm. **h**, Quantification of OVA coverage over time. $n = 5$ mice/group; two-way ANOVA mixed-effects analysis (30 last min only). **i** and **j**, Mice were then perfused and whole brains were imaged by stereomicroscopy, then the brains were sliced and analyses were made on brain coronal sections. **i**, Representative images showing OVA distribution and quantification in whole brains and a zoom on the middle cerebral artery. Scale bars, 2 mm (left panels) and 1mm (right panels). **j**, Representative images showing OVA coverage on brain coronal sections. Scale bar, 2 mm. For **i** and **j**, $n = 5$ mice/group; two-tailed unpaired Welch's t -test. **k**, One week after PBM depletion and one hour after i.c.m. injection of OVA, mice were perfused, brains were extracted, and OVA distribution was analyzed on coronal sections stained for DAPI, and corresponding quantification of OVA depth distribution from the brain surface. Scale bars, 100 μ m and 50 μ m (insets). $n = 5$ mice/group; two-tailed unpaired Welch's t -test. **l**, Representative images showing anti-aquaporin 4 (AQP4) staining. Scale bar, 50 μ m. **m**, Quantification of AQP4 coverage. **n**, Quantification of AQP4+ blood vessels. For **m** and **n**, $n = 5$ mice/

group; two-tailed unpaired Welch's t -test. **o**, Brain sections were co-stained for anti-AQP4 (yellow) and anti-CD31 (cyan), and perpendicular lines to blood vessels were used to measure the perivascular space. Scale bars, 50 μ m and 10 μ m (insets). **p**, Representation of the perivascular space (PVS) in PBS (left) and CLO (right) treated mice. **q**, Quantification of perivascular space. $n = 4$ mice treated with PBS, and 5 mice treated with CLO; two-tailed unpaired Welch's t -test. **r**, One week after PBM depletion, mice received an i.c.m. injection of fluorescent beads (0.1 μ m thick; 5 μ l) and then were immediately placed on their side under the stereomicroscope for dynamic bead imaging at the MCA level. **s**, Representative images showing bead distribution over an hour at the proximal part of the MCA. Scale bar, 1mm. **t**, Quantification of bead coverage at the MCA level over time. $n = 4$ mice treated with PBS, and 7 mice treated with CLO; repeated measures 2-way ANOVA with Geisser-Greenhouse correction. **u**, Representative images showing beads located at the MCA perivascular space *in vivo* (left) and *ex vivo* after perfusion with PBS and post-fixation in 4% PFA (right) from the same mouse. Scale bar, 1mm. **v**, Representative images from extracted whole brain showing bead repartition at low (left image) and higher magnification (right image) and corresponding plot profile. The beads (green line) are located outside of the MCA (red line), at the perivascular level. Scale bar, 2 mm. **w**, Measure of the perivascular space (PVS) between *in vivo* and *ex vivo* from the same mice. $n = 4$ mice; Two-tailed paired t -test. **x**, Representative images showing *ex vivo* bead repartition at the MCA level in PBM-depleted mice and PBS-treated control mice, and corresponding quantification of bead coverage. Scale bar, 500 μ m; $n = 4$ mice treated with PBS, and 5 mice treated with CLO; two-tailed unpaired Welch's t -test. **y**, Quantifications of total perivascular space (space between the two sides of the MCA where beads were found to accumulate) and MCA diameter (identified by the i.v. lectin injection). **z**, Quantification of the functional space where beads were found to be accumulated. For **y** and **z**: $n = 10$ mice treated with PBS, and 9 mice treated with CLO; two-tailed unpaired Welch's t -test. All data are presented as mean values \pm SEM. The illustration of mice in **a**, **f** and **r** are from Servier Medical Art, CC BY 3.0.



Extended Data Fig. 5 | PBM depletion has mild effect on mouse behavior and no effect on vital signs. One week after PBM depletion, mice underwent a battery of different behavioral tests. **a**, Cued fear conditioning: quantification of the percentage of time spent freezing during the three shocks the first day, and exposure to conditioned clues at one- and seven days after fear conditioning. **b**, Elevated plus maze: quantifications of the percentage of time spent in the open arm (left), the total time spent in the open arm (middle) and the total distance moved (right). **c**, Open field test: quantification of the distance moved over an hour, the total distance moved, the time spent in the center of the box over an hour and the total time spent in the center of the box. **d**, Forced swim

test: quantification of the total floating time (left) and the latency to float (right). For **a-d**: $n = 10$ mice/group; two-tailed unpaired Welch's t -test. **e**, Three-chamber test: mice were first exposed to a mouse (S1) or an object (O), and then to a previously-exposed mouse (S1) or a new mouse (S2). Quantifications of the total sniffing time and the total time spent in the chamber for the two tests. $n = 17$ mice treated with PBS, and 13 mice treated with CLO; two-tailed unpaired Welch's t -test. **f**, One week after PBM depletion, respiratory rate, heart rate, arterial pulsation and diameter were monitored. $n = 5$ mice/group; two-tailed unpaired Welch's t -test. All data are presented as mean values \pm SEM.

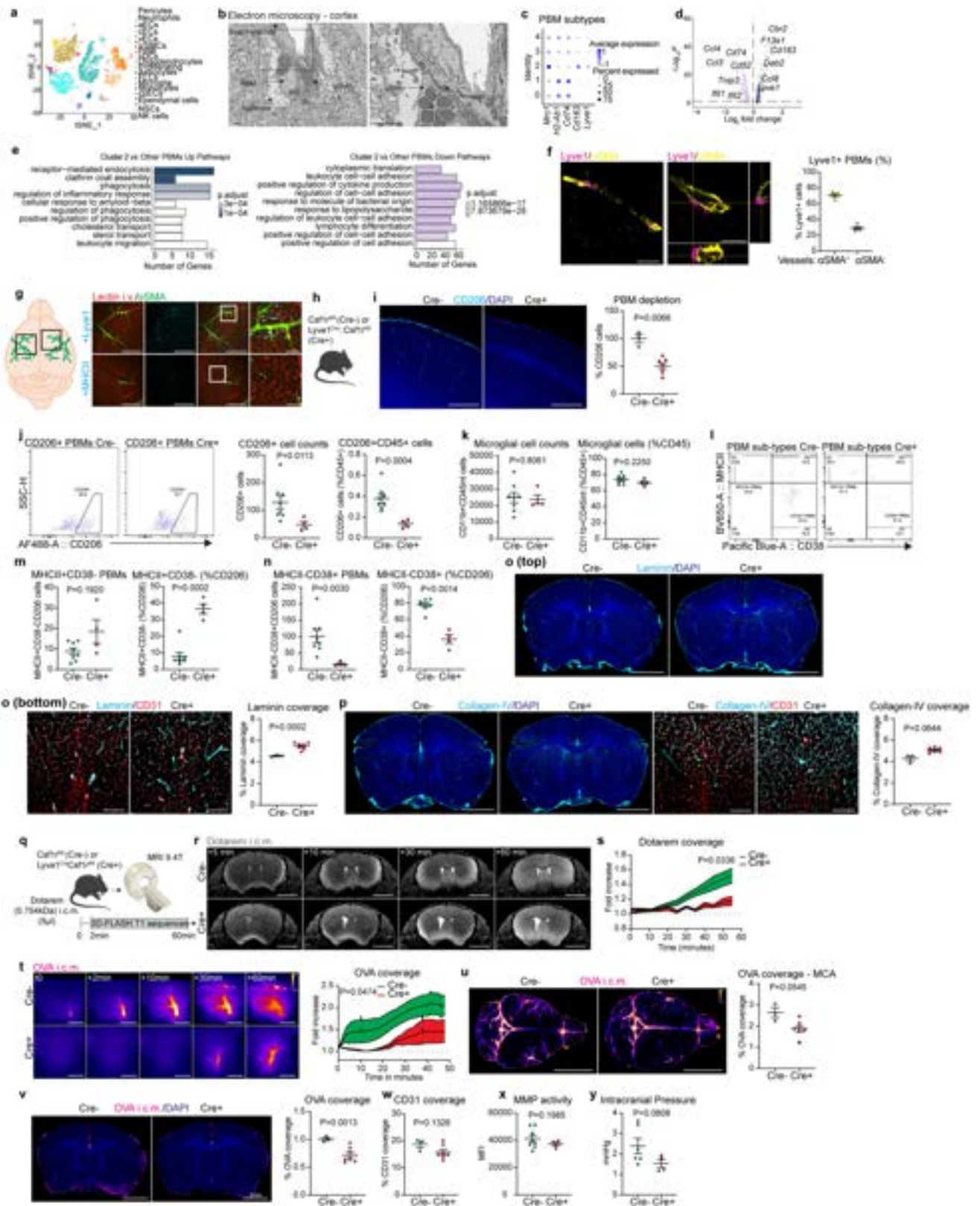


Extended Data Fig. 6 | See next page for caption.

Extended Data Fig. 6 | PBMs and extracellular matrix remodelling.

a, One week after CLO or PBS liposome injection, mice were perfused, brains were extracted, lateral choroid plexuses were removed, CD45-CD13+ and CD45-CD31+ cells were sorted and used for single-cell RNA sequencing. Nine different cell types were identified based on canonical markers. **b**, Volcano plot corresponding to up- and down-regulated genes comparing fibroblasts in PBM-depleted mice and PBS-treated control mice, and corresponding GO Pathway analyses showing up- (left) and down-regulated (right) pathways. **c**, Volcano plot corresponding to up- and down-regulated genes comparing pericytes in PBM-depleted mice and PBS-treated control mice, and corresponding GO Pathway analyses showing up- (left) and down-regulated (right) pathways. **d**, Volcano plot corresponding to up- and down-regulated genes comparing capillary endothelial cells (cECs) in PBM-depleted mice and PBS-treated control mice, and corresponding GO Pathway analyses showing up- (left) and down-regulated (right) pathways. For **b–d**, Volcano plots: *F*-test with adjusted degrees of freedom based on weights calculated per gene with a zero-inflation model and Benjamini-Hochberg adjusted *P* values; GO-pathways analyses: over-representation test. **e**, Representative images showing cortical brain sections stained for anti-CD13 (mural cells, yellow) co-stained for anti-CD206 (magenta), anti-Laminin (cyan) and DAPI, and corresponding quantification. Scale bar, 100 μ m; *n* = 5 mice/group; two-tailed unpaired Welch's *t*-test. **f**, Representative images showing cortical brain sections stained for anti-CD31 (endothelial cells) and corresponding quantification. Scale bar, 200 μ m; *n* = 6 mice/group; two-tailed unpaired Welch's *t*-test. **g**, Representative images showing cortical brain sections of mice that were i.c.m. injected with OVA (magenta), stained for anti- α SMA (vascular smooth muscle cells, cyan) and co-stained for anti-CD31 (yellow), and corresponding quantification. Scale bar, 200 μ m; *n* = 6 mice/group; two-tailed unpaired Welch's *t*-test. **h**, One week after

CLO or PBS liposome injection, brain coronal sections were stained for anti-Laminin (cyan) and DAPI (blue). Scale bar, 2 mm. **k**, High magnification images showing Laminin (cyan) in association with CD31+ blood vessels (red). Scale bar, 200 μ m. **i**, Representative Western blot images of Collagen-IV (160 kDa) and Ponceau S from isolated brain blood vessels one week after PBM depletion, and corresponding quantification. *n* = 5 mice/group; two-tailed unpaired Welch's *t*-test. **j**, Representative images showing Collagen-IV (cyan) deposition at both α SMA+ (arteries/arterioles; yellow) and α SMA- blood vessels. Scale bar, 200 μ m. **k** and **l**, Representative images from mouse cortex showing accumulation of **k**: Collagen-IV; and **l**: Laminin (cyan), co-stained for anti-CD31 (red), and respective quantifications. Scale bars, 200 μ m; *n* = 6 mice/group; two-tailed unpaired Welch's *t*-test. **m**, High magnification images showing Laminin (cyan) in association with α SMA+ surface and penetrating large blood vessels (magenta), and corresponding quantifications. **n**, High magnification images showing Collagen-IV (cyan) in association with α SMA+ surface and penetrating large blood vessels (magenta), and corresponding quantifications. For **m** and **n**: Scale bar, 200 μ m; *n* = 5 mice/group; two-tailed unpaired Welch's *t*-test. **o**, Experimental schematic: mice received an i.p. injection of dobutamine (40 μ g/kg) or saline 30min prior to receiving an i.c.m. injection of OVA (1mg/ml; 5 μ l). Mice were perfused one hour later. **p**, Representative images showing OVA distribution in whole brains and corresponding quantifications. **q**, Representative images showing OVA coverage on brain coronal sections and corresponding quantifications. For **p** and **q**, Scale bars, 2 mm; *n* = 6 mice treated with PBS, 4 mice treated with CLO in saline group; 3 mice treated with PBS, and 5 mice treated with CLO in dobutamine group; two-way ANOVA with multiple comparisons. All data are presented as mean values \pm SEM. The illustrations of mice in **a** and **o** are from Servier Medical Art, CC BY 3.0.

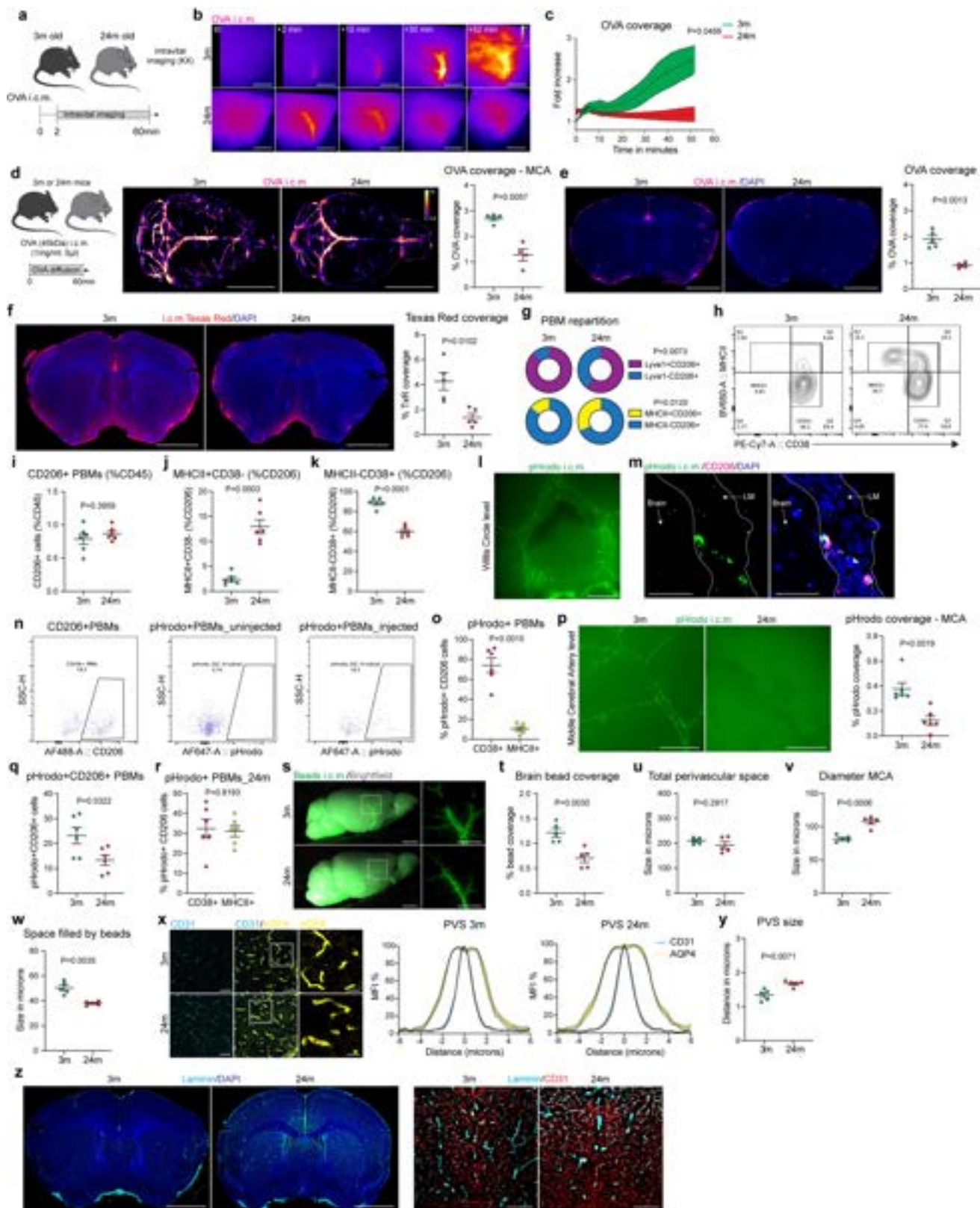


Extended Data Fig. 7 | See next page for caption.

Article

Extended Data Fig. 7 | LYVE1+ PBMs drive CSF flow dynamics. **a**, Single-cell RNA sequencing of the whole brain was performed. Eighteen cell types were identified based on canonical markers. **b**, Scanning electron microscopy image from a mouse cortex suggesting interactions between a PBM and a vascular smooth muscle cell (VSMC). Scale bars, 2 μ m. **c**, Dot plot for *Mrc1* (CD206), *H2-Ab1* (MHCII), *Cd74*, *Cd163* and *Lyve1* expression in each PBM cluster. **d** and **e**, Volcano plot and GO pathway analysis showing up- and down-regulated pathways in PBM cluster 2 versus other PBM clusters. Volcano plots: *F*-test with adjusted degrees of freedom based on weights calculated per gene with a zero-inflation model and Benjamini-Hochberg adjusted *P* values; GO-pathways analyses: over-representation test. **f**, Representative images suggesting interactions between LYVE1+ PBMs (magenta) and α SMA+ (yellow) VSMC. Scale bar, 200 μ m and 50 μ m (inset). **g**, Quantification of LYVE1+ cells associated or not with α SMA+ blood vessels. *n* = 5 mice. **h**, Mice received an i.v. injection of lectin and were perfused few minutes later. Whole brains were extracted, post-fixed with 4% PFA, and stained for anti- α SMA (green) and anti-LYVE1 (top panels) or anti-MHCII (bottom panels) (cyan). Scale bars: 1mm and 200 μ m (insets). **i**, Characterization of PBM depletion in *Lyve1^{Cre}::Csf1r^{fl/fl}* mice (Cre+) in brain coronal sections using CD206 staining (co-stained for DAPI) versus control littermates not expressing Cre (*Csf1r^{fl/fl}*; Cre-). Scale bar, 500 μ m; *n* = 7 Cre- mice, and 3 Cre+ mice; two-tailed unpaired Welch's *t*-test. **j**, Flow cytometry panels showing CD206+ cells in *Csf1r^{fl/fl}* mice (Left; Cre-) and *Lyve1^{Cre}::Csf1r^{fl/fl}* mice (Right; Cre+), and quantifications of CD206+ PBM cell numbers (left), and frequency of CD206+ PBMs from total CD45+ cells (right). **k**, Quantification of CD11b+CD45^{int} microglial cell numbers (left), and frequency of CD11b+CD45^{int} microglial cells from total CD45+ cells (right). **l**, Flow cytometry panels showing CD38+ and/or MHCII+ CD206+ PBMs in *Csf1r^{fl/fl}* mice (Left; Cre-) and *Lyve1^{Cre}::Csf1r^{fl/fl}* mice (Right; Cre+). **m**, Quantification of MHCII+CD38- PBMs (left), and frequency of MHCII+CD38- PBMs from total CD206+ cells (right). **n**, Quantification of MHCII-CD38+ PBMs (left), and frequency of MHCII-CD38+ PBMs from total CD206+ cells (right). For **i**–**n**: *n* = 8 Cre- mice, and 4 Cre+ mice; two-tailed unpaired Welch's *t*-test. **o**, (Top) Representative images of coronal brains sections from *Lyve1^{Cre}::Csf1r^{fl/fl}* (Cre+)

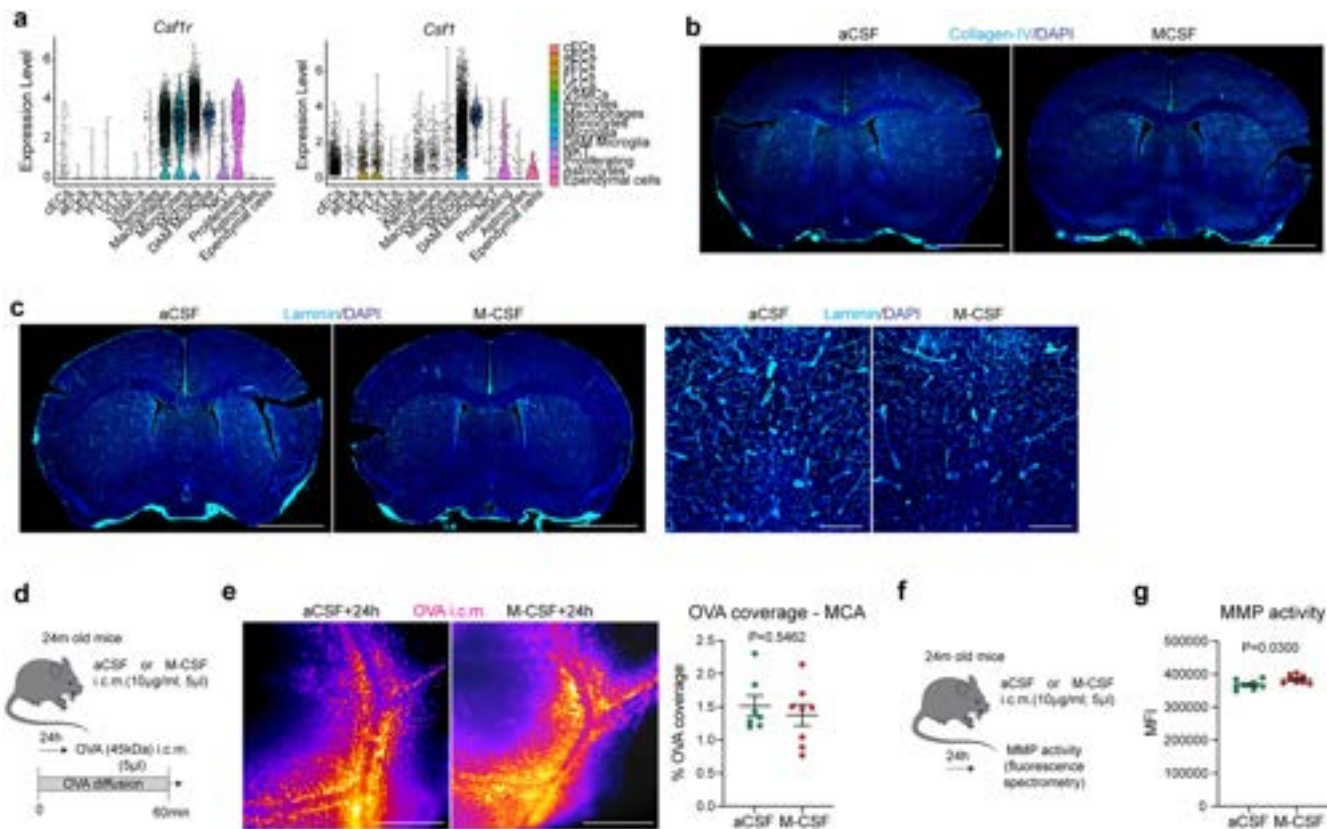
and *Csf1r^{fl/fl}* (Cre-) mice co-stained for anti-Laminin (cyan) and DAPI. (Bottom) High magnification images showing Laminin location at the vicinity of CD31+ blood vessels (red), and corresponding quantification. Scale bars, 2mm (top) and 200 μ m (bottom). **p**, (Left) Representative images of coronal brains sections from *Lyve1^{Cre}::Csf1r^{fl/fl}* (Cre+) and *Csf1r^{fl/fl}* (Cre-) mice co-stained for anti-Collagen-IV (cyan, right panels) and DAPI. (Right) High magnification images showing Collagen-IV location at the vicinity of CD31+ blood vessels (red), and corresponding quantification. Scale bars, 2 mm (left) and 200 μ m (Right). **q**, Three-month-old Cre+ and Cre- mice received an i.c.m. injection of Dotarem (0.754kDa; 5 μ l) and were immediately placed in prone position into the MRI device for dynamic imaging. **r**, Representative brain coronal images showing Dotarem distribution over an hour. Scale bar, 3mm. **s**, Quantification of Dotarem signal fold increase over time, *n* = 8 Cre- mice, and 5 Cre+ mice; repeated measures 2-way ANOVA with Geisser-Greenhouse correction. **t**, *In vivo* imaging of OVA coverage at the MCA level in *Lyve1^{Cre}::Csf1r^{fl/fl}* (Cre+) and *Csf1r^{fl/fl}* (Cre-) mice, with corresponding representative images and quantification. Scale bar, 1 mm; *n* = 7 Cre- mice, and 5 Cre+ mice; repeated measures 2-way ANOVA with Geisser-Greenhouse correction. **u**, Representative images showing OVA distribution in whole brains in *Lyve1^{Cre}::Csf1r^{fl/fl}* (Cre+) and *Csf1r^{fl/fl}* (Cre-) mice. Scale bar, 5 mm. **v**, OVA coverage in coronal sections of *Lyve1^{Cre}::Csf1r^{fl/fl}* (Cre+) and *Csf1r^{fl/fl}* (Cre-) mice. Scale bar, 2mm. For **u** and **v**: *n* = 7 Cre- mice, and 3 Cre+ mice; two-tailed unpaired Welch's *t*-test. **x**, Quantification of CD31 coverage in *Lyve1^{Cre}::Csf1r^{fl/fl}* (Cre+) and *Csf1r^{fl/fl}* (Cre-) mouse brain sections. *n* = 7 Cre- mice, and 3 Cre+ mice; two-tailed unpaired Welch's *t*-test. **y**, Quantification of MMP activity from *Lyve1^{Cre}::Csf1r^{fl/fl}* (Cre+) and *Csf1r^{fl/fl}* (Cre-) mice measured by fluorescence spectrometry after 15 min of incubation. *n* = 8 Cre- mice, and 4 Cre+ mice; two-tailed unpaired Welch's *t*-test. **z**, Quantification of intracranial pressure from *Lyve1^{Cre}::Csf1r^{fl/fl}* (Cre+) and *Csf1r^{fl/fl}* (Cre-) mice. *n* = 6 Cre- mice, and 4 Cre+ mice; two-tailed unpaired Welch's *t*-test. All data are presented as mean values \pm SEM. The illustrations of mice (**h**, **q**) and the MRI scanner (**q**) are from Servier Medical Art, CC BY 3.0.



Extended Data Fig. 8 | See next page for caption.

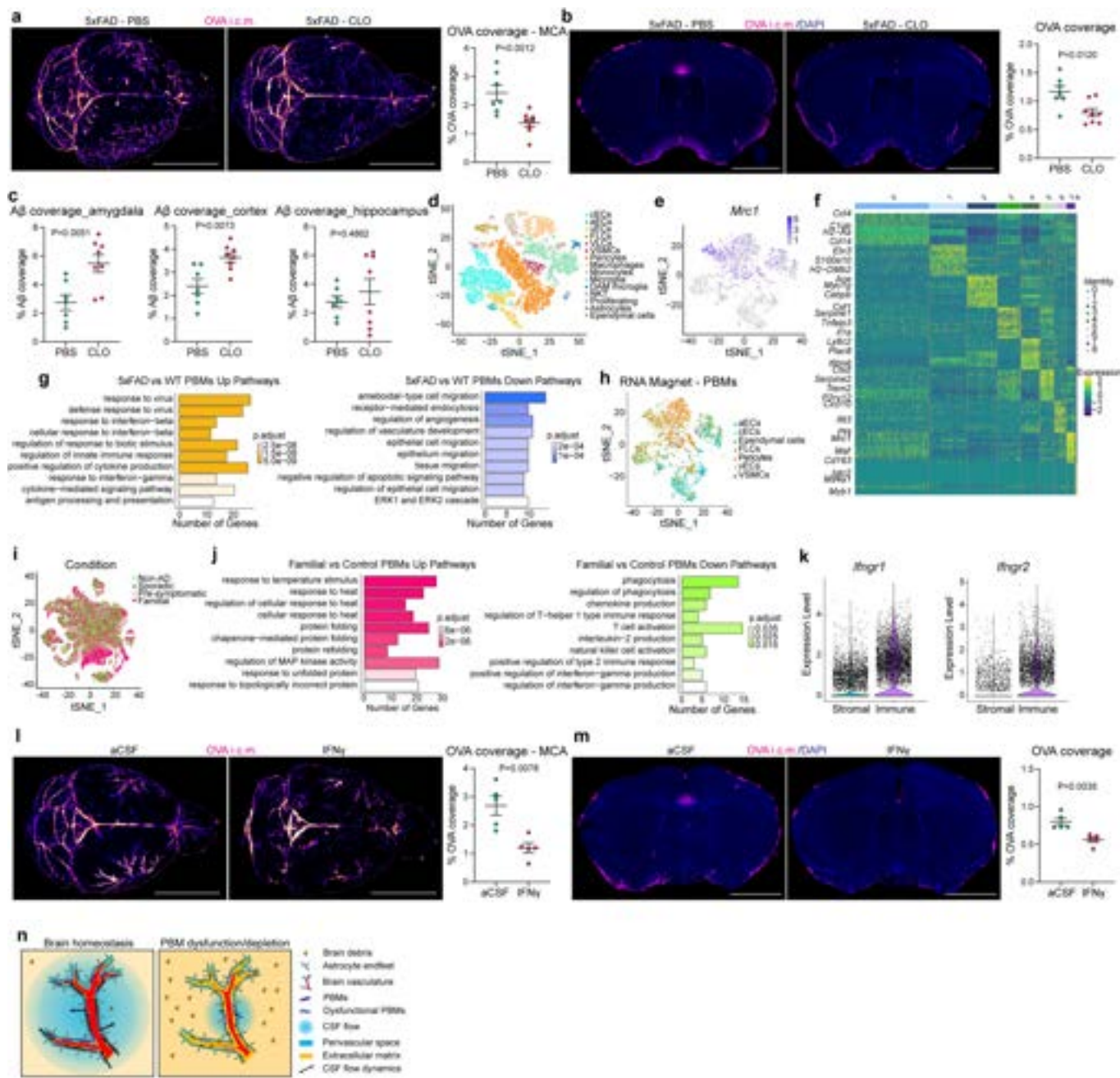
Article

Extended Data Fig. 8 | PBMs in normal aging. **a**, Experimental schematic: young adult (3-month-old) and aged (24-month-old) mice received an i.c.m. injection of OVA (45 kDa; 1mg/ml; 5 μ l). Immediately after the injection, mice were placed on their side under the stereomicroscope for dynamic imaging. **b**, Representative images showing OVA distribution over time. Scale bar, 1 mm. **c**, Quantification of OVA signal fold increase over time in 3 m and 24 m old mice. $n = 5$ mice/group; repeated measures 2-way ANOVA with Geisser-Greenhouse correction. **d** and **e**, 3m and 24 m old mice received an i.c.m. injection of OVA. Mice were perfused one hour later. **d**, Representative images showing OVA distribution in whole brains in 3 m and 24 m old mice, and corresponding quantification. Scale bar, 5 mm. **e**, OVA coverage in coronal sections in 3 m and 24 m old mice, and corresponding quantification. Scale bar, 2 mm. For **d** and **e**: $n = 5$ 3 m mice, and 4 24 m mice; two-tailed unpaired Welch's t -test. **f**, 3m and 24m old mice received an i.c.m. injection of Texas Red (3 kDa; 1mg/ml; 5 μ l), brains were harvested one hour later. Representative images of Texas Red coverage (red) and corresponding quantification. Scale bar, 2 mm. $n = 5$ mice/group; two-tailed unpaired Welch's t -test. **g**, Pie chart representation of the quantification of LYVE1+MHCII- versus LYVE1-MHCII+ PBMs by immunostaining. $n = 5$ mice/group; two-tailed unpaired Welch's t -test. **h**, Representative flow cytometry plots from 3 m and 24 m old mice showing PBM subtypes, characterized by their expression of CD38 and MHCII. **i-k**, Quantification of **i**: CD206+ PBMs; **j**: MHCII+CD38- PBMs and **k**: MHCII-CD38+ PBMs. For **i-k**, $n = 6$ mice/group; two-tailed unpaired Welch's t -test. **l**, 3m and 24m old mice received an i.c.m. injection of pHrodo particles (1 μ m; 5 μ l), which became fluorescent only after being phagocytosed. Scale bar, 2 mm. **m**, Representative confocal image showing pHrodo particles being phagocytosed by CD206+ PBMs. Scale bar, 50 μ m. **n**, pHrodo-positive PBMs can also be detected by flow cytometry. **o**, Quantification of pHrodo+MHCII-CD38+ versus pHrodo+MHCII+CD38- PBMs in 3 m old mice. $n = 6$ mice; paired t -test. **p**, Representative images of 3 m and 24 m old mice showing pHrodo particle repartition at the MCA level, and corresponding quantification. Scale bar, 2 mm. **q**, Quantification of pHrodo+CD206+ PBMs in 3 m and 24 m old mice. For **p** and **q**: $n = 6$ mice/group; two-tailed unpaired Welch's t -test. **r**, Quantification of pHrodo+MHCII-CD38+ versus pHrodo+MHCII+CD38- PBMs in 24 m old mice. $n = 6$ mice; paired t -test. **s**, 3 m and 24 m old mice received an i.c.m. injection of fluorescent beads (0.1 μ m thick; 5 μ l). Mice were perfused one hour later. Representative image from extracted whole brain showing bead repartition at low (left images) and higher magnification (insets, right images). Scale bars, 2 mm and 1 mm (insets). **t**, Quantification of brain bead coverage. **u**, Quantifications of total perivascular space (space between the two sides of the MCA where beads were found to accumulate) **v**, Quantification of MCA diameter (identified by the i.v. lectin injection). **w**, Quantification of the functional space where beads were found to be accumulated. For **t-w**: $n = 5$ mice/group; two-tailed unpaired Welch's t -test. **x**, Brain coronal sections from 3 m and 24 m old mice were co-stained for anti-AQP4 (yellow) and anti-CD31 (cyan) to measure the perivascular space size. Scale bars, 50 μ m and 10 μ m (insets), and representation of the perivascular space (PVS) diameter in 3 m (middle) and 24 m (right) old mice. **y**, Quantification of perivascular space diameter. $n = 5$ mice/group; two-tailed unpaired Welch's t -test. **z**, (Left) Brain coronal sections were stained for anti-Laminin (cyan) and DAPI (blue). Scale bar, 2 mm. (Right) High magnification images showing Laminin (cyan) in association with CD31+ blood vessels (red). Scale bar, 200 μ m. All data are presented as mean values \pm SEM. The illustrations of mice in **a** and **d** are from Servier Medical Art, CC BY 3.0.



Extended Data Fig. 9 | M-CSF treatment in old mice. **a**, Violin plots showing expression of *Csf1r* mostly by PBMs, monocytes and microglia, as well as expression of *Csf1*, expressed mostly by endothelial, mural and microglial cells, from the mouse 5xFAD single-cell RNA sequencing dataset. **b** and **c**, Brain coronal sections of aged mice six hours after i.c.m. injection of artificial CSF (aCSF) or M-CSF (10 µg/ml; 5 µl) were stained for **b**: anti-Collagen-IV (left panels) or **c**: anti-Laminin (right panels) and co-stained for DAPI. Scale bars, 2 mm and 200 µm. **d**, Experimental schematic: 24 m old mice received an i.c.m. injection of M-CSF (or aCSF as a control), and mice received an i.c.m. injection

of OVA to assess CSF flow 24 h later. **e**, Representative images showing OVA coverage at the MCA level, and corresponding quantification. Scale bar, 500 µm. $n = 7$ mice treated with aCSF, and 8 mice treated with M-CSF; two-tailed unpaired Welch's *t*-test. **f**, Experimental schematic: 24 m old mice received an i.c.m. injection of M-CSF (or aCSF as a control), and MMP activity was assessed by fluorescence spectrometry 24 h later. **g**, Quantification of MMP activity. $n = 8$ mice/group; two-tailed unpaired Welch's *t*-test. All data are presented as mean values \pm SEM. The illustrations of mice in **d** and **f** are from Servier Medical Art, CC BY 3.0.



Extended Data Fig. 10 | PBMs in an Alzheimer's disease mouse model and in AD patients.

a and **b**. One month after CLO or PBS liposome injection, 5xFAD mice received an i.c.m. injection of OVA, and brains were analyzed one hour later. **a**, Representative images and quantification of OVA distribution in whole brains. Scale bar, 2 mm. **b**, Representative images and quantification of OVA coverage on brain coronal sections. Scale bar, 2 mm. For **a** and **b**, $n = 7$ 5xFAD mice treated with PBS, and 8 5xFAD mice treated with CLO; two-tailed unpaired Welch's t -test. **c**, Quantification of A β coverage in amygdala, cortex and hippocampus. $n = 7$ 5xFAD mice treated with PBS, and 8 5xFAD mice treated with CLO; two-tailed unpaired Welch's t -test. **d**, tSNE plot showing 35 different clusters on the 5xFAD mouse single-cell RNA sequencing dataset, based on expression of CD13, CD31 and CD45. **e**, *Mrc1* expression in macrophage cluster allows PBM identification. **f**, Heatmap showing top 10 positively differentially expressed genes per cluster by adjusted p -value. **g**, GO Pathway analysis showing up- and down-regulated pathways in 5xFAD mice compared to their WT littermates. Over-representation test. **h**, The RNA Magnet algorithm

determined that PBMs interact preferentially with vascular smooth muscle cells (VSMCs), pericytes and fibroblast-like cells (FLCs). **i**, Single-nuclei RNA sequencing on familial, pre-symptomatic, sporadic and non-AD patients. **j**, GO Pathway analysis showing up- and down-regulated pathways in familial AD patients compared to controls. Over-representation test. **k**, Gene expression levels of *Ifngr1* and *Ifngr2* from immune versus stromal cells from the mouse 5xFAD single-cell RNA sequencing dataset. **l** and **m**, Wild-type mice received an i.c.m. injection of artificial CSF (aCSF) or interferon gamma (IFN γ , 20 ng/ml; 1 μ l). The same mice received an i.c.m. injection of OVA (1mg/ml; 5 μ l) 3 h later and brains were harvested one hour later. **l**, Representative images and quantification of OVA distribution in whole brains. **m**, Representative images showing OVA coverage on brain coronal sections and corresponding quantification. For **l** and **m**, $n = 5$ mice/group; two-tailed unpaired Welch's t -test. **n**, Proposed model that recapitulates the findings. All data are presented as mean values \pm SEM.

Reporting Summary

Nature Research wishes to improve the reproducibility of the work that we publish. This form provides structure for consistency and transparency in reporting. For further information on Nature Research policies, see [Authors & Referees](#) and the [Editorial Policy Checklist](#).

Statistics

For all statistical analyses, confirm that the following items are present in the figure legend, table legend, main text, or Methods section.

n/a Confirmed

- The exact sample size (n) for each experimental group/condition, given as a discrete number and unit of measurement
- A statement on whether measurements were taken from distinct samples or whether the same sample was measured repeatedly
- The statistical test(s) used AND whether they are one- or two-sided
Only common tests should be described solely by name; describe more complex techniques in the Methods section.
- A description of all covariates tested
- A description of any assumptions or corrections, such as tests of normality and adjustment for multiple comparisons
- A full description of the statistical parameters including central tendency (e.g. means) or other basic estimates (e.g. regression coefficient) AND variation (e.g. standard deviation) or associated estimates of uncertainty (e.g. confidence intervals)
- For null hypothesis testing, the test statistic (e.g. F , t , r) with confidence intervals, effect sizes, degrees of freedom and P value noted
Give P values as exact values whenever suitable.
- For Bayesian analysis, information on the choice of priors and Markov chain Monte Carlo settings
- For hierarchical and complex designs, identification of the appropriate level for tests and full reporting of outcomes
- Estimates of effect sizes (e.g. Cohen's d , Pearson's r), indicating how they were calculated

Our web collection on [statistics for biologists](#) contains articles on many of the points above.

Software and code

Policy information about [availability of computer code](#)

Data collection

The following softwares were used to collect the data in this study:

- LAS X Version: 4.3.0.24308, Leica Microsystems CMS GmbH
- Olympus V200 ASW 3.3 (Build 24382)
- Kaluza Analysis Software v1.0
- Paravision 360.2.0.pl.1

Data analysis

The following softwares were used to analyze the data in this study:

- FIJI image processing software (NIH) - v2.3.0/1.53f
- Prism v9.2.0 (GraphPad Software, Inc)
- FastQC v0.11.5
- Salmon v0.8.2
- R v3.5.0
- MATLAB 9.7
- Cytobank 7.2
- Bioconductor DESeq2 v3.5
- Custom code used for single-cell and single-nucleus RNA-seq analysis is available from the corresponding authors upon reasonable request.

For manuscripts utilizing custom algorithms or software that are central to the research but not yet described in published literature, software must be made available to editors/reviewers. We strongly encourage code deposition in a community repository (e.g. GitHub). See the Nature Research [guidelines for submitting code & software](#) for further information.

Data

Policy information about [availability of data](#)

All manuscripts must include a [data availability statement](#). This statement should provide the following information, where applicable:

- Accession codes, unique identifiers, or web links for publicly available datasets
- A list of figures that have associated raw data
- A description of any restrictions on data availability

Source data files depicting the quantification values mentioned in the text or plotted in graphs shown in Figs. 1-5 and Extended Data Figs. 1-10, are available in the online version of this paper at <http://www.nature.com/nature>. RNA-seq data sets have been deposited online in the Gene Expression Omnibus (GEO database) under the accession numbers GSE188283, GSE188284, GSE188285. Custom code used to analyze the RNA sequencing data is freely available at <https://doi.org/10.5281/zenodo.7047054>. All other data generated in this study are available online in a GraphPad Prism file. To access the data from the DIAN brain bank, special request must be made using this URL: <https://dian.wustl.edu/our-research/for-investigators/>.

Field-specific reporting

Please select the one below that is the best fit for your research. If you are not sure, read the appropriate sections before making your selection.

Life sciences Behavioural & social sciences Ecological, evolutionary & environmental sciences

For a reference copy of the document with all sections, see nature.com/documents/nr-reporting-summary-flat.pdf

Life sciences study design

All studies must disclose on these points even when the disclosure is negative.

Sample size	Sample sizes were chosen on the basis of standard power calculations (with $\alpha = 0.05$ and power of 0.8) performed for similar experiments that were previously published (Louveau et al., Nature Neuroscience 2018; Da Mesquita et al., Nature 2021). In general, statistical methods were not used to re-calculate or predetermine sample sizes.
Data exclusions	The ROUT test was used to identify and discard potential outliers. No exclusion criteria were pre-established. Mice that died during the Magnetic Resonance Imaging (MRI) were excluded from the study (2 mice).
Replication	Number of reliable reproductions of each experimental finding is stated in each Figure legend. Unless stated otherwise, main experimental findings were replicated at least once. Experimental replication was not attempted for negative data.
Randomization	Reported in Methods section, Statistical analysis and reproducibility subsection: Animals from different cages, but within the same experimental group, were selected to assure randomization. Mice from the same cage received different treatments (for example, in a cage of 5 mice, 2 mice received PBS-loaded liposomes and 3 mice received CLO-loaded liposomes). Treatment was given in a blind manner and could be identified by a corresponding ear tag (treatment A: left ear was tagged; treatment B: right ear was tagged).
Blinding	Reported in Methods section, Statistical analysis and reproducibility subsection: Experimenters were blinded to the identity of experimental groups from the time of experimental treatment until the end of data collection and analysis for all the independent experiments. One exception was the experiment regarding CSF flow dynamics between young (3-month-old) and aged (24-month-old) mice, which are distinguishable by their weight/fur.

Reporting for specific materials, systems and methods

We require information from authors about some types of materials, experimental systems and methods used in many studies. Here, indicate whether each material, system or method listed is relevant to your study. If you are not sure if a list item applies to your research, read the appropriate section before selecting a response.

Materials & experimental systems

n/a	Involved in the study
<input type="checkbox"/>	<input checked="" type="checkbox"/> Antibodies
<input checked="" type="checkbox"/>	<input type="checkbox"/> Eukaryotic cell lines
<input checked="" type="checkbox"/>	<input type="checkbox"/> Palaeontology
<input type="checkbox"/>	<input checked="" type="checkbox"/> Animals and other organisms
<input type="checkbox"/>	<input checked="" type="checkbox"/> Human research participants
<input checked="" type="checkbox"/>	<input type="checkbox"/> Clinical data

Methods

n/a	Involved in the study
<input checked="" type="checkbox"/>	<input type="checkbox"/> ChIP-seq
<input type="checkbox"/>	<input checked="" type="checkbox"/> Flow cytometry
<input type="checkbox"/>	<input checked="" type="checkbox"/> MRI-based neuroimaging

Antibodies

Antibodies used

The following primary antibodies were used for IHC:

- primary antibodies: rat anti-mouse CD206 (Bio-Rad MCA2235, 1:500), goat anti-mouse Iba1 (Abcam, ab5076, 1:500), Armenian hamster anti-mouse CD31 (Millipore Sigma, MAB1398Z, clone 2H8, 1:200), rabbit anti-mouse AQP4 (Millipore Sigma, A5971, 1:500), eFluor 660 conjugated anti-mouse Lyve1 (eBioscience, clone ALY7, 1:200), Alexa Fluor 594 conjugated anti-mouse I-A/I-E (MHCII; BioLegend, 107650, 1:200), rabbit anti-mouse Laminin (Abcam, ab7463, 1:500), rabbit anti-mouse Collagen-IV (EMD Millipore, AB756P, 1:500), FITC conjugated anti-mouse alpha SMA (Sigma Aldrich, F3777, 1:200), goat anti-mouse CD13 (R&D systems, AF2335, 1:200), rabbit anti-mouse amyloid beta (Cell Signaling Technology, 8243S, D54D2, 1:400). in PBS-T containing 0.5% BSA.

- secondary antibodies: rat, chicken, goat or donkey eFluor570 or Alexa Fluor® 488, 594, or 647 conjugated anti-rat, -goat, -rabbit, -mouse or -Armenian hamster IgG antibodies (Thermo Fisher Scientific, all at 1:500 in PBS-T).

The following antibodies were used for Western Blot analysis: primary antibody goat anti-mouse Collagen-IV (BioRad 134001; 1:500) with a HRP-conjugated donkey anti-goat secondary antibody (Abcam, ab97120, 1:10000) diluted in blocking buffer.

The following antibodies were used for fluorescence-activated cell sorting:

- rat anti-mouse CD16/32 (BioLegend, 101302); rat anti-mouse CD13 (BD Biosciences, 558744, FITC), rat anti-mouse Ly6C (BioLegend, 128033, BV510), rat anti-mouse XCR1 (BioLegend, 148216, BV421), rat anti-mouse CD24 (BioLegend, 101819, Pacific Blue), rat anti-mouse Ly6G (BD Biosciences, 741587, BUV661), rat anti-mouse CD45 (BD Biosciences, 746947, BV750), rat anti-mouse CD19 (BD Biosciences, 751213, BUV615), rat anti-mouse CD11b (BD Biosciences, 741242, BUV563), rat anti-mouse TCRb (BD Biosciences, 748405, BUV805), rat anti-mouse CD4 (BD Biosciences, 563790, BUV395), rat anti-mouse F4/80 (BioLegend, 123133, BV605), rat anti-mouse CD64 (BD Biosciences, 139308, PerCP-Cy5.5), rat anti-mouse CD206 (BioLegend, 141710, AF488), rat anti-mouse CD38 (BioLegend, 102716, A647 or BioLegend, 102719, Pacific Blue), rat anti-mouse MHCII (BioLegend, 107641, BV650). All at 1:200 in FACS buffer, except for anti-CD13 (at 1:50).

Validation

Each antibody was validated for the species (mouse) and application (immunohistochemistry, cell sorting) by the correspondent manufacturer. The usage was described in full detail the methods section of the manuscript.

Immunohistochemistry:

Tissue was rinsed in PBS and incubated with appropriate dilutions of primary antibodies (from the list described in the previous section) in PBS 0.5% Triton-X-100 overnight at 4°C. Whole mounts or tissue sections were then washed 3 times for 5 min at RT in PBS 0.5% Triton-X-100 followed by incubation with the appropriate secondary antibodies (from the list described in the previous section) for 2 hours at RT in PBS 0.5% Triton-X-100.

Sorting of whole brain hemisphere myeloid (microglia/macrophage), blood endothelial and mural cells or of brain cortical myeloid cells:

Briefly, after tissue digestion, the cell pellets were washed, resuspended in ice-cold FACS buffer, preincubated for 10 min at 4°C with Fc-receptor blocking solution (anti-CD16/32, 101302, BioLegend, 1:200 in FACS buffer) and stained for extracellular markers with a mix of primary antibodies from the list described in the previous section, for 25 minutes at 4°C.

Animals and other organisms

Policy information about [studies involving animals](#); [ARRIVE guidelines](#) recommended for reporting animal research

Laboratory animals

Mice were bred in house or obtained from the Jackson Laboratory or provided by the National Institutes of Health/National Institute on Aging (24-month-old mice). Mice were housed in 12-hour light-dark cycle in a temperature- and humidity-controlled environment with water and food ad libitum. Mice were housed at least one week at the animal facility before any experimentation. Both males and females were used in this study. The following mouse strains were used in this study: C57BL/6J (WT; JAX 000664), C57BL/6-Tg (UbcGFP; JAX 004353), hemizygous B6SJL-Tg (APPSwFILon, PSEN1*M146L*L286V)6799Vas/Mmjax (5xFAD mice; JAX 008730), Lyve1cre (B6;129P2-Lyve1tm1.1(EGFP/cre)Cys/J; JAX 012601), Csf1rf1/fl (B6.Cg-Csf1rtm1.2Jwp/J; JAX 021212), Aldh1l1Cre/ERT2(B6; JAX 031008).

Wild animals

The study did not involve wild animals.

Field-collected samples

The study did not involve samples collected from the field.

Ethics oversight

All experiments were approved by the Institutional Animal Care and Use Committee of the University of Virginia and the Institutional Animal Care and Use Committee of the Washington University in Saint-Louis.

Note that full information on the approval of the study protocol must also be provided in the manuscript.

Human research participants

Policy information about [studies involving human research participants](#)

Population characteristics

Covariate-relevant population characteristics are publicly available in Da Mesquita et al., Nature 2021, Supplementary Table 3.

Recruitment

The Neuropathology Cores of the Charles F. and Joanne Knight Alzheimer's Disease Research Center (Knight-ADRC) and the Dominantly Inherited Alzheimer Network (DIAN) provided the parietal lobe tissue of postmortem brains for each sample. These samples were obtained with informed consent for research use and were approved by the review board of Washington University in St. Louis. AD neuropathological changes were assessed according to the criteria of the National Institute on Aging-Alzheimer's Association (NIA-AA). Their demographic, clinical severity, and neuropathological information are presented in Supplementary Table 3.

Ethics oversight

The brain samples used in the single-nucleus RNA-seq experiments were obtained with informed consent for research use and were approved by the review board of Washington University in St. Louis.

Flow Cytometry

Plots

Confirm that:

- The axis labels state the marker and fluorochrome used (e.g. CD4-FITC).
- The axis scales are clearly visible. Include numbers along axes only for bottom left plot of group (a 'group' is an analysis of identical markers).
- All plots are contour plots with outliers or pseudocolor plots.
- A numerical value for number of cells or percentage (with statistics) is provided.

Methodology

Sample preparation

Mice received a lethal intraperitoneal injection of euthasol (10% v/v in saline, 250 l), and transcardially perfused with PBS containing 10U/ml heparin. Lateral choroid plexuses were removed from half- or whole brains. Brains were then digested for 40 min at 37C with 1.4U/ml of Collagenase-VIII and 35U/ml of DNase I in DMEM. The cell pellets were washed and resuspended in FACS buffer and stained with the following antibodies (1:200 dilution; eBioscience): rat anti-mouse Ly6C (BV510), rat anti-mouse XCR1 (BV421), rat anti-mouse CD24 (Pacific Blue), rat anti-mouse Ly6G (BUV661), rat anti-mouse CD45 (BV750), rat anti-mouse CD19 (BUV615), rat anti-mouse CD11b (BUV563), rat anti-mouse TCRb (BUV805), rat anti-mouse CD4 (BUV395), rat anti-mouse F4/80 (BV605), rat anti-mouse CD64 (PerCP-Cy5.5), rat anti-mouse CD38 (A647 or Pacific Blue), rat anti-mouse MHCII (BV650). Cell viability was determined using DAPI staining. Fluorescence data were acquired using Cytek Aurora spectral flow cytometer (Cytek) then analyzed using FlowJo Software (Tree Star, v5.0). For one experiment, mice received an i.c.m. injection of pHrodo particles (Life Technologies, P35360), that were detected by A647.

Instrument

- Aurora™ Flow Cytometer (Cytek)

Software

- FlowJo software v10.8.1 (Tree Star, Inc.)

Cell population abundance

For each individual experiment, single-cell suspensions were incubated with viability dyes and aliquots from the unstained single-cell suspensions were incubated with ViaStain™ AOPI Staining Solution (CS2-0106, Nexcelom Bioscience)

Gating strategy

Flow cytometry and FACS using brain tissue preparations:
Briefly, singlets were gated using the height, area and the pulse width of the forward and side scatters and then viable cells were selected as being negative for SYTOX or DAPI. Whole brain hemisphere myeloid (microglia/macrophage) cells were identified and sorted as DAPI-CD45+CD11b+Ly6G-. Blood endothelial and mural cells were identified and sorted as DAPI-CD45-CD11b-CD31+ and DAPI-CD45-CD11b-CD13+CD31-, respectively. Brain cortical myeloid cells were identified and sorted as SYTOX-Ly6G-CD45+CD11b+.

- Tick this box to confirm that a figure exemplifying the gating strategy is provided in the Supplementary Information.

Magnetic resonance imaging

Experimental design

Design type

Evaluation of CSF flow using i.c.m. Dotarem injection and tracing over time

Design specifications

The total acquisition time was of about 1 h per mouse (4m54sec x 12 sequences per mouse).

Behavioral performance measures

None

Acquisition

Imaging type(s)

Contrast-enhanced MRI

Field strength

9.4 Tesla

Sequence & imaging parameters

Series of post-contrast T1 FLASH-3D weighted images were taken through the head with the following parameters: repetition time = 30 ms; echo time = 8 ms; number of echo images = 1; number of averages = 1; number of repetitions = 12; scan time = 272640 ms per sequence (4m54sec); flip angle = 20, FOV = 160 x 160 x 80 μm with a 128 x 128 x 64 matrix; spatial resolution = 125 x 125 x 125 μm (8 pixels per mm; voxel size = 0.125 mm³), number of slices = 64; receiving coil 4 elements RF ARR 400 1H M.

Area of acquisition

Mouse head

Diffusion MRI

Used

Not used

Preprocessing

Preprocessing software	Paravision 360.2.0.pl.1
Normalization	Each mouse was its own control
Normalization template	Each mouse was its own control (diffusion of tracer over time)
Noise and artifact removal	No noise or artifact removal
Volume censoring	No volume censoring

Statistical modeling & inference

Model type and settings	Tracer diffusion overtime per mouse (univariate)
Effect(s) tested	Repeated measure ANOVA
Specify type of analysis:	<input type="checkbox"/> Whole brain <input type="checkbox"/> ROI-based <input checked="" type="checkbox"/> Both
Anatomical location(s)	Whole brain, middle cerebral artery territory
Statistic type for inference (See Eklund et al. 2016)	Specify voxel-wise or cluster-wise and report all relevant parameters for cluster-wise methods.
Correction	Geisser-Greenhouse correction

Models & analysis

n/a	Involvement in the study
<input checked="" type="checkbox"/>	<input type="checkbox"/> Functional and/or effective connectivity
<input checked="" type="checkbox"/>	<input type="checkbox"/> Graph analysis
<input checked="" type="checkbox"/>	<input type="checkbox"/> Multivariate modeling or predictive analysis